



TECHNISCHE  
UNIVERSITÄT  
WIEN

Vienna University of Technology

DISSERTATION

# Surface Chemistry of $\text{Fe}_3\text{O}_4$ (001)

Ausgeführt zum Zwecke der Erlangung des akademischen Grades  
eines Doktors der Naturwissenschaften unter der Leitung von

Univ.-Prof. Dipl.-Ing. Dr.techn. Ulrike Diebold

Institut für Angewandte Physik (E134)

Zweitbetreuung:

Univ.-Ass. Gareth S. Parkinson, PhD

eingereicht an der Fakultät für Physik

der technischen Universität Wien

von

Oscar Alberto Gamba Vasquez

1228638

Josef-Baumann-Gasse 8a/402, 1220 Wien

Wien, Oktober 2016



# Acknowledgements

I would like to express my sincere gratitude to my supervisor, Ulrike Diebold, for giving me the opportunity to work in her group, for her constant supervision and interest for my work, and for showing me a really nice way to make science. I would like to thank Gareth Parkinson for being an important person during my PhD studies, thanks for opening the door of his house, for all the teachings that I received from him and for always being willing to offer his advice. I am grateful to Michael Schmid, who always has been willing to offer his inexhaustible knowledge to answer any kind of question. I would like to say thank you to all members of the surface science group for the nice work team. I am grateful to Roland Bliem for helping me with the german version of the abstract and for all his help during my time here. I acknowledge support from the Austrian Science Fund (FWF) doctoral school Solids4fun (Project W1243), the Austrian Science Fund START prize Y 847-N20 and Project No. P24925-N20.

Quiero agradecer a las personas más importantes en mi vida que en la distancia siempre fueron el soporte y la motivación de continuar con este sueño; mis padres, Eduardo y Ana, mis hermanos Olga, Nestor y Hugo y mi sobrinito Sebas. A mi gran amigo Manuel por las charlas, su amistad y por mandarme la convocatoria, jeje. Por último, y no menos importante quiero agradecer el amor e incondicionalidad de mi novia, gracias por ser.



# Abstract

Metal oxides offer a diversity of structures and compositions that make them excellent candidates as catalysts for reactions involving organic compounds. In this context, magnetite,  $\text{Fe}_3\text{O}_4$ , appears as an attractive material due to its naturally abundance and its electronic properties that make it a material widely used in several catalytic process. Its catalytic activity is related to the presence of both,  $\text{Fe}^{2+}$  and  $\text{Fe}^{3+}$  cations, in its inverse spinel structure. Moreover, the presence of these cations together with oxygen anions represent an important aspect in its acid-base chemistry.

The present thesis presents a surface science study with the aim to understand the reactivity of the  $\text{Fe}_3\text{O}_4(001)$  surface toward small organic molecules such as methanol ( $\text{CH}_3\text{OH}$ ) and formic acid ( $\text{HCOOH}$ ), as well as its role in the water gas shift reaction. The surface chemistry was investigated using an array of surface science techniques including scanning tunneling microscopy (STM), X-ray photoelectron spectroscopy (XPS), low-energy electron diffraction (LEED), temperature programmed desorption (TPD), and infrared reflection absorption spectroscopy (IRRAS) (in collaboration with another group).

The  $\text{Fe}_3\text{O}_4(001)$  surface undergoes a  $(\sqrt{2}\times\sqrt{2})R45^\circ$  reconstruction associated with a cation rearrangement in the subsurface layers, involving two subsurface Fe vacancies and one interstitial Fe atom per unit cell. A major part of the work presented here was devoted to the identification of the most common surface defects, and determining their effect on adsorption. It was discovered that surface defects can be classified in two groups. The first group, line defects include step edges and anti-phase domain boundaries (APDBs). The latter arise because the  $(\sqrt{2}\times\sqrt{2})R45^\circ$  reconstruction is lifted during annealing cycles, and then renucleates on cooling through 723 K with one of two distinct registries with respect to the underlying bulk. The second group, point defects, include surface hydroxyl groups and a defect related with Fe atoms incorporated in the subsurface. In this thesis

this defect is identified, and purposely created by the deposition of Fe onto the clean surface at room temperature. This process also leads to Fe adatoms, and, at high coverage, the so called Fe-dimer surface. Here the Fe atoms of the "dimer" are fourfold coordinated to surface oxygen atoms, filling two of the four octahedral interstitial sites per unit cell. XPS indicates that the Fe-dimer surface contains  $\text{Fe}^{2+}$ .

The  $\text{Fe}_3\text{O}_4(001)$  surface adsorbs  $\text{HCOOH}$  and  $\text{CH}_3\text{OH}$  at room temperature, yielding adsorbed formate ( $\text{HCOO}^-$ ) and methoxy ( $\text{CH}_3\text{O}^-$ ) species, respectively. Formate adsorbs in a bridging bidentate configuration at regular iron surface lattice sites locally producing two different periodicities, one with  $(1\times 1)$  symmetry and a second one with  $(2\times 1)$  symmetry. The adsorbed formate decomposes to produce  $\text{CO}$ ,  $\text{H}_2\text{O}$ ,  $\text{CO}_2$ , and  $\text{H}_2\text{CO}$ , and the reactivity is linked with the presence of surface defects. Methanol adsorbs dissociatively on the  $\text{Fe}_3\text{O}_4(001)$  surface at defect sites that were identified as step edges, antiphase domain boundaries (APDB), iron adatoms and incorporated-Fe defects. The adsorption at the steps and Fe adatoms can be explained in terms of coordinative unsaturation, while the reactivity at the APDBs and incorporated Fe defects is linked to the local electronic structure; specifically to the presence of  $\text{Fe}^{2+}$  cations in the surface layers. The adsorption of multiple methoxy species at the latter two defects promotes a disproportionation reaction to form methanol and formaldehyde.

The implications of  $\text{Fe}_3\text{O}_4(001)$  surface chemistry on catalytic processes was studied using the water gas shift reaction as an example. The co-adsorption of  $\text{CO}$  and  $\text{H}_2\text{O}$  generates the presence of four carbon surface species that are stable at room temperature. Three of them were identified as formate, iron carbide, and carbon in the form of graphite or  $\text{CH}_x$  hydrocarbon fragment respectively. The other species was postulated to be  $\text{HOCO}$  or  $\text{HCO}$  groups, but test experiments on formaldehyde adsorption did not confirm this hypothesis. Theoretical studies would be necessary for complete identification.

# Kurzfassung

Metalloxide kommen in einer Vielzahl von Strukturen und chemischen Zusammensetzungen vor und in vielen Anwendungen eingesetzt unter anderem für die Katalyse organischer Verbindungen. Magnetit,  $\text{Fe}_3\text{O}_4$ , gilt hier als besonders attraktives Material, da es in der Natur weit verbreitet ist und aufgrund seiner elektronischen Eigenschaften bereits in verschiedenen katalytischen Prozessen Anwendung findet. Die katalytische Aktivität dieses Materials steht in engem Zusammenhang mit der Koexistenz von  $\text{Fe}^{2+}$  und  $\text{Fe}^{3+}$  Kationen im Kristallgitter, welches auf der inversen Spinellstruktur basiert. Diese Eisenkationen stellen gemeinsam mit den Sauerstoffanionen einen wichtigen Aspekt der Säure-Basen-Chemie von Magnetit dar.

Die vorliegende Dissertation ist eine oberflächenwissenschaftliche Studie mit dem Ziel, die Reaktivität der  $\text{Fe}_3\text{O}_4(001)$  Oberfläche für kleine organische Moleküle, wie Methanol ( $\text{CH}_3\text{OH}$ ) und Ameisensäure ( $\text{HCOOH}$ ) zu verstehen, und die Rolle dieser Oberfläche in der Wassergas-Shift-Reaktion zu untersuchen. Die Eigenschaften dieser Oberfläche wurden mittels oberflächenphysikalischer Methoden, insbesondere mit Rastertunnelmikroskopie (STM), Röntgen-photoelektronenspektroskopie (XPS), Niedrigenergie-Elektronenbeugung (LEED), Temperatur-programmierter Desorption (TPD) und Infrarot-Reflexions-Absorptions-Spektroskopie (IRRAS), untersucht.

Die  $\text{Fe}_3\text{O}_4(001)$  Oberfläche bildet eine  $(\sqrt{2} \times \sqrt{2})R45^\circ$  Rekonstruktion, die auf einer Umschichtung der Struktur mit zwei Eisenfehlstellen und einem Zwischengitteratom pro Einheitszelle in den ersten beiden Lagen unter der Oberfläche beruht. Ein Großteil der hier vorgestellten Arbeit befasst sich auf der Identifizierung der häufigsten Oberflächendefekte und der Beschreibung ihrer Wirkung auf die Adsorptionseigenschaften. Es wurde gezeigt, dass Oberflächendefekte in zwei Gruppen eingeteilt werden können: Zur Gruppe der Liniendefekte zählen Stufenkanten und Anti-Phasen-Domänengrenzen (APDBs). Letztere entstehen, wenn sich die Rekonstruktion nach Heizen der Oberfläche bei

etwa 723 K wieder ausbildet. Diese Keimbildung beginnt an unterschiedlichen Orten auf der Oberfläche aus, welche um eine nicht rekonstruierte Einheitszelle versetzt sein können, was zur Bildung von Domänengrenzen führt. Die zweite beobachtete Gruppe von Defekten sind Punktdefekte, diese schließen neben Hydroxylgruppen an der Oberfläche auch Eisenatome, die die Fehlstellen in der Rekonstruktion füllen ein. In der vorliegenden Dissertation wird dieser Defekt als Inkorporation von Eisen identifiziert und durch Aufbringen von Eisen auf die reine Oberfläche bei Raumtemperatur reproduziert. Dieses Verfahren führt auch zur Bildung von Eisenadatomen und bei hohen Bedeckungen zur sogenannten Fe-Dimer Oberfläche. Dabei sind die Eisenatome des sogenannten Dimers vierfach zu Sauerstoffatomen in der Oberfläche koordiniert und füllen zwei der vier oktaedrischen Zwischengitterplätze pro Einheitszelle. XPS Experimente zeigen eine Anreicherung der Fe-Dimer-Oberfläche mit  $\text{Fe}^{2+}$ .

$\text{HCOOH}$  und  $\text{CH}_3\text{OH}$  adsorbieren auf der  $\text{Fe}_3\text{O}_4(001)$  Oberfläche bei Raumtemperatur als Formiat- ( $\text{HCOO}^-$ ) und Methoxy- ( $\text{CH}_3\text{O}^-$ ) Spezies. Adsorbiertes Formiat bildet zwei Bindungen zu den benachbarten Eisenatomen aus. Es entstehen unterschiedliche Periodizitäten auftreten, entweder mit  $(1 \times 1)$  oder  $(2 \times 1)$  Symmetrie. Beim Aufheizen der Probe wird das adsorbierte Formiat zu  $\text{CO}$ ,  $\text{H}_2\text{O}$ ,  $\text{CO}_2$  und  $\text{H}_2\text{CO}$  zersetzt, wobei die Reaktivität mit der Anwesenheit von Oberflächendefekten korreliert. Methanol adsorbiert dissoziativ auf Defekten der  $\text{Fe}_3\text{O}_4(001)$  Oberfläche, welche als Stufenkanten, Antiphasen-Domänengrenzen (APDB), Eisenadatom und inkorporierte Eisenatome identifiziert wurden. Die Adsorption an Stufen und auf Eisenadatomaten kann mittels ungesättigter Bindungen aufgrund niedriger Koordination erklärt werden, während die Reaktivität der APDBs und inkorporierten Eisenatomdefekte mit der lokalen elektronischen Struktur zusammenhängt; insbesondere mit der Anwesenheit von  $\text{Fe}^{2+}$ -Kationen in der Oberfläche. Die Adsorption von mehreren Methoxy-Spezies auf den beiden letztgenannten Defekten begünstigt die Disproportionierung zu Methanol und Formaldehyd.



Die Auswirkungen der Eigenschaften der  $\text{Fe}_3\text{O}_4(001)$  Oberfläche auf katalytische Prozesse wurden in Bezug auf die Wassergas-Shift-Reaktion untersucht. Die Koadsorption von CO und  $\text{H}_2\text{O}$  bei Raumtemperatur führt zur Bildung von vier stabilen Kohlenstoffspezies auf der Oberfläche. Drei dieser Spezies konnten als Formiat, Eisencarbid und Kohlenstoff in Form von Graphit oder Kohlenwasserstoff-Fragmenten  $\text{CH}_x$  identifiziert werden. Die aufgestellte Hypothese, dass es sich bei der vierte Spezies um Formaldehyd handeln könnte, konnte durch getrennt durchgeführte Adsorptionsexperimente nicht verifiziert werden. Die verbleibende Spezies könnte HOCO oder HCO Gruppen zugeschrieben werden, wobei für eine vollständige Identifizierung noch zusätzliche theoretische Studien benötigt werden.



# Contents

<b>1. Introduction .....</b>	<b>1</b>
<b>2. Experimental.....</b>	<b>8</b>
2.1 X-ray Photoelectron Spectroscopy (XPS) .....	9
2.2 Temperature Programmed Desorption (TPD) .....	11
2.3 Scanning Tunneling Microscopy (STM) .....	15
2.4 Low Energy Electron Diffraction (LEED) .....	17
2.5 Infrared Reflection Absorption Spectroscopy (IRRAS) .....	19
2.6 Experimental Setups.....	21
2.6.1 OMEGA System.....	21
2.6.2 The Machine for Reactivity Studies "The Mrs." .....	22
2.6.3 IRRAS Measurements.....	23
2.7 Sample Preparation .....	24
2.8 Evaporation Materials .....	24
2.9 Liquids and Gases .....	24
<b>3. Iron Oxides.....</b>	<b>25</b>
3.1 Magnetite, Fe <sub>3</sub> O <sub>4</sub> .....	25
3.2 The Fe <sub>3</sub> O <sub>4</sub> (001) Surface .....	27

3.3.1 Line Defects on the Fe <sub>3</sub> O <sub>4</sub> (001) Surface .....	32
3.3.2 Point Defects on the Fe <sub>3</sub> O <sub>4</sub> (001) Surface.....	33
<b>4. Fe-Dimer Surface.....</b>	<b>36</b>
4.1 Fe Deposition at Room Temperature: Effect of Oxygen .....	38
4.2 Fe Deposition: From Fe Adatom to the Fe-Dimer Surface.....	40
4.3 XPS.....	42
4.4 Thermal Stability of the Fe-Dimer Surface .....	43
4.5 Fe-rich (001) Surface: Reactivity to Oxygen .....	45
4.6 Discussion .....	48
4.7 Conclusions .....	51
<b>5. Surface Defects on Fe<sub>3</sub>O<sub>4</sub>:The Methanol Adsorption Case.....</b>	<b>52</b>
5.1 Adsorption of Methanol on Metal Oxide Surfaces.....	53
5.2 Adsorption of CH <sub>3</sub> OH on the Clean Fe <sub>3</sub> O <sub>4</sub> (001) Surface .....	55
5.3 Fe-rich Fe <sub>3</sub> O <sub>4</sub> (001) Surface .....	56
5.4 Adsorption of CH <sub>3</sub> OH on the Fe-rich Fe <sub>3</sub> O <sub>4</sub> (001) Surface.....	58
5.5. Spectroscopic Study of the Adsorption and Reaction of Methanol on Clean and Fe-rich Fe <sub>3</sub> O <sub>4</sub> (001)-( $\sqrt{2}\times\sqrt{2}$ )R45° Surface.....	61
5.5.1 XPS .....	61
5.5.2. Temperature Programmed Desorption Spectroscopy .....	65

5.6 Adsorption of CH <sub>3</sub> OH on the Fe-Dimer Surface.....	69
5.8. Discussion .....	72
5.9 Conclusions .....	75
<b>6. Adsorption of Formic Acid on the Fe<sub>3</sub>O<sub>4</sub> (001) Surface. ....</b>	<b>76</b>
6.1 Adsorption of Formic Acid on Metal Oxide Surfaces.....	77
6.2 Adsorption of Formic Acid on Iron Oxide Surfaces .....	80
6.3 Adsorption of Formic Acid on the Clean Fe <sub>3</sub> O <sub>4</sub> (001) Surface .....	81
6.3.1 XPS .....	81
6.3.2 Infrared Reflection Absorption Spectroscopy .....	85
6.3.3 Low Energy Electron Diffraction .....	87
6.3.4 Scanning Tunneling Microscopy .....	89
6.3.5 Temperature Programmed Desorption Spectroscopy .....	93
6.4. Discussion: Formic Acid on Fe <sub>3</sub> O <sub>4</sub> (001)-( $\sqrt{2}\times\sqrt{2}$ )R45° Surface .....	98
6.4.1. Adsorption Behavior .....	98
6.4.2. Desorption Behavior.....	101
6.5 Adsorption of HCOOH on the Fe-Dimer Surface .....	103
6.6 Conclusions .....	108
<b>7. The Water Gas Shift Reaction on the Fe<sub>3</sub>O<sub>4</sub>(001) Surface: Related Adsorption Experiments.....</b>	<b>109</b>

7.1 Introduction .....	109
7.2 The WGS on $\text{Fe}_3\text{O}_4(001)$ Surface .....	112
7.3. Discussion: The WGS on $\text{Fe}_3\text{O}_4(001)$ Surface.....	119
<b>Conclusion.....</b>	<b>125</b>
<b>Bibliography .....</b>	<b>127</b>







# 1. Introduction

In the most general concept catalysis can be defined as a process where a catalyst accelerates a chemical reaction. During the process the catalyst typically forms bonds with the reactant molecules such that these can react to form a product. The product then leaves the surface, making the catalyst available for the next reaction. The catalytic reaction is thus as a cyclic event in which the catalyst takes part and is recovered in the last step of the cycle (1).

The importance of catalysis lies in the fact that the rate of chemical reactions can be accelerated by orders of magnitude, and allow reactions to be carried out under favorable conditions of temperature and pressure. This has had a big impact in the chemical industry, in which almost 90% of all processes require at least one catalytic process in its implementation (2).

Catalysis can be divided in two main subclasses: homogeneous and heterogeneous catalysis. In homogeneous catalysis, the catalyst and the reactants are of the same phase, while in the heterogeneous catalysis the phase of the reactants and catalysts is different. In heterogeneous catalysis the catalyst is usually a solid, which catalyzes reactions of molecules in gas or liquid phase (3).

Most industrial catalyzed reactions are of the heterogeneous type. The first crucial step in heterogeneous catalysis is adsorption of the reactants, which leads to the formation of reaction intermediates. This adsorption is normally divided into physisorption and chemisorption. In the case of physisorption the interaction between the adsorbate and the surface is due to van der Waals forces. Chemisorption, on the other hand, is characterized by strong chemical bonds, which can be either covalent or ionic, between the adsorbate and the surface (4).

Once the reactants are adsorbed, they may migrate over the surface of the catalyst. When the reactants meet, they could react forming new surface

intermediates compounds which remain bound to the surface. Finally the products of the reaction are desorbed from the surface (3).

A crucial unknown in the catalytic process is often the nature and stability of surface intermediates, which play an important role in the pathway between reactants and products. The chemistry behind these intermediates is difficult to determine, and often depends strongly on the structure and composition of the surfaces used as catalyst (3).

The development of ultra-high vacuum technology led to the development of many modern techniques for the study of the adsorption and reaction of molecules on surfaces. The use of well-defined single crystals of different materials as model catalysts, prepared and studied under controlled conditions, allows researchers to describe the basic processes involved in heterogeneous catalysis (5, 6). In this context, surface science appears as a crucial field, which offers powerful tools to understand the principles behind heterogeneous catalysis and determine the active sites for adsorption and reactions on surfaces.

A particularly important development was the emergence of scanning probe techniques in the 1980s. Previously, studies of adsorption and reactions on surfaces were limited by a lack of knowledge of the local atomic structure of the surface (5). With the emergence of scanning tunneling microscopy and atomic force microscopy, these methods have been used extensively to characterize the structure of the surfaces and have provided atomic resolution images of many adsorption process on different kind of surfaces (5-7).

Metal oxides are important components of a wide range of solid catalysts. The variety of the structure and composition of metal oxide surfaces leads to a wide range of roles in catalytic processes, for example as the inexpensive support of active phases, as precursors of active phases components, or as active phase itself. Even when just used as a support of metal nanoparticles the properties of the oxide are important as they can facilitate the transport of reactants over the catalyst surface, and facilitate surface phenomena such as hydrogen spillover (8)

and the spillover of organic intermediates (6, 9-11). Furthermore, the metal oxide support is crucial in processes such as SMSI (12) and can even become involved in oxidation reactions via the so-called Mars van-Krevelen mechanism (13).

In many cases metal oxides function as the active phase, interacting with adsorbates to make reactions such as oxidation and selective dehydrogenation of organic compounds. Here the activation of the organic compounds on the metal oxide surfaces involves the scission of different chemical bonds such as the C-H or O-H bonds (10, 14).

The presence of accessible coordinatively unsaturated centers appears as one of the most important factors. The metal oxides have to exhibit to act as an active phase in adsorption and reaction processes, In this sense, metal oxides present two of these active centers, the cations and anions (7, 10).

The reaction of metal oxide surfaces with different organic compounds such as alcohols, aldehydes, and carboxylic acids, is an important issue because these organic compounds and their derivatives are often important intermediates in reactions such as cracking and isomerization of hydrocarbons, oxidations, dehydrogenation, dehydration, and esterification, among others (5, 6, 10).

These type of reactions have been described in terms of acid-base interactions. Acidity and basicity depend on the nature of the oxide, the charge and radius of the metal ions, the character of the metal-oxygen bond, and the coordination numbers of the anions and cations (15). Metal oxides expose cation-anion pairs which can be active sites for dissociative adsorption of alcohols and carboxylic acids (5, 16).

The adsorption occurs due the abstraction of the acidic proton of the organics by a surface  $O^{2-}$  anion to form a hydroxyl group, while the conjugate base anion of the molecule bonds to an exposed metal cation. This process is often described using a Brønsted acid-base formalism (5, 7).

Another important concept to describe the reactivity of metal oxides is the Lewis acid-base definition. The bonding of the conjugate base of an organic molecule to a surface metal cation can be described as a Lewis adduct, where the conjugate

base anion (Lewis base) donates a pair of electrons to the metal cation which acts as electron-accepting (Lewis acid).

Acid-base chemistry on metal oxide surfaces are often characterized in terms of probe reactions. One example of this is the dehydration/ dehydrogenation selectivity for conversion of alcohols. It has been shown by adsorption on ZnO (17), MgO (14, 18) and TiO<sub>2</sub>(19, 20) that both dehydration and dehydrogenation of alcohols proceeds through a common surface alkoxide intermediate. Here, the initial dissociative adsorption on acid or base sites is not what controls the product distribution, it is the selectivity between competing alkoxide decomposition channels. The dehydration that leads to the production of alkenes or ethers is generally considered to be an acid-catalyzed pathway, while dehydrogenation is categorized as base catalyzed. Nevertheless, this categorization must be taken with care due that the reducibility of the oxide plays a role in the selectivity (5, 7).

As will be described throughout this document, the local coordination of the cations and anions, and their electronic configurations are crucial aspects to explain their reactivity, as well as the presence of surface defects.

Step edges are common defects on metal oxide surfaces, and have been cataloged as active sites for the adsorption of weak acids, as in the case of MgO (100) surface (14, 18, 21). In general, steps are reactive because the atoms at the step edge are missing more bonds than the atoms on the regular terrace. A particularly interesting case in point is ZnO, where two inequivalent polar surfaces exist; the (0001) surface that is terminated with Zn cations and the  $(000\bar{1})$  surface that is terminated with O anions. Neither surface is expected to be reactive because of the lack of undercoordinated cation-anion pairs, but in reality both surfaces show some activity linked to the step edges. The ZnO (0001) surface, in particular, exhibits many small terraces with steps that expose undercoordinated cation-anion pairs in close proximity (22-24).

In addition to steps, the leading role of point defects such as oxygen vacancies has been highlighted. This defect has been identified as an active site for dissociative adsorption of oxygenates on  $\text{CeO}_2$  (111) (25-27) and  $\text{TiO}_2$  (110) surfaces (28, 29). The oxygen vacancies act as a direct adsorption sites or as electron donor sites thus modifying the local electronic structure (30). Here two ways in which the oxygen vacancies can modify the adsorption on metal oxide surfaces appear: decreasing the coordination of the surface atoms and changing the electron count.

In this regard the reducibility of the oxides also plays an important role in the mechanism of adsorption on defects as the case of oxygen vacancies.  $\text{MgO}$  has been categorized as an irreducible oxide, wherein the oxygen vacancies leave electrons trapped in the vacancy (31-33). These oxygen vacancies have a great importance for the properties and reactivity of  $\text{MgO}$  (30, 34).

On the other hand,  $\text{TiO}_2$  is a reducible oxide. The removal of a neutral O atom has been shown to result in two unpaired electrons on the fivefold coordinate Ti neighboring to the vacancy. Here the adsorption is associated with an electron transfer, where the reduction of a Ti atom is expected (35). Deoxygenation reaction of  $\text{D}_2\text{O}$ ,  $\text{CH}_2\text{O}$  and  $\text{NO}$  have been related with the presence of  $\text{Ti}^{3+}$  sites on  $\text{TiO}_2$  (110) surface (36).

Different to these materials, where the oxygen vacancies play an important role, another class of metal oxides exists where stoichiometric variation and their reactivity is related to the presence and absence of cations, the iron oxides(37).

The iron oxides appears as an important material in heterogeneous catalysis. They have been used in numerous processes such as the synthesis of  $\text{NH}_3$ , the water gas shift reaction, the Fischer-Tropsch synthesis, and the oxidation and dehydrogenation of different organic compounds (38).

In the case of the synthesis of  $\text{NH}_3$ , the main component of the catalysts used for the process is magnetite with others promoters such as  $\text{Al}_2\text{O}_3$ . Here the magnetite is reduced to iron, to give an alpha-Fe matrix, where the  $\text{Al}_2\text{O}_3$  is distributed over

the surface of the Fe particles (38). Here the surface of the catalyst forms a nitrogen complex, which is more easy to hydrogenate to  $\text{NH}_3$  than the  $\text{N}_2$  (39).

In Fischer-Tropsch synthesis, hydrogen reacts with CO at around 200-300 °C to produce a range of reactions products, which includes acids, alcohols, aldehydes, and hydrocarbon fuels. In the industrial process,  $\text{SiO}_2$  promoted with hematite is used as catalyst (40). During the reaction the catalyst changes to a mixture of iron carbide, hematite, and magnetite (41-43). Here the active phase appears to be carbide compounds from the transformation of magnetite and hematite (40, 44).

The water gas shift reaction, in which carbon monoxide and water react to produce carbon dioxide and hydrogen, is one of the most important reactions in the field of catalysis. The current industrial catalyst most used for the reaction is based on magnetite ( $\text{Fe}_3\text{O}_4$ ) (45-47) (Further information about this reaction will be discussed in chapter 7.)

Despite the intensive use of iron oxides in the processes mentioned above, details concerning reaction pathways, the identification of active intermediates and active sites is not completely clear. This synopsis shows clearly the need for further investigation in this field, where the use of surface science approach appears as an attractive alternative.

The goal of this thesis is to investigate the surface chemistry of a prototypical iron oxide surface;  $\text{Fe}_3\text{O}_4$  (001). Magnetite is an important material in different fields such as groundwater remediation (48), corrosion, and is of particular interest in heterogeneous catalysis where it is involved in different reactions as was mentioned above (46, 49). The (001) surface has received increasing interest in surface science, partly because it exhibits an interesting reconstruction that is stable over a wide range of chemical potentials (37). Moreover, the surface can be reproducibly prepared, and functions as a robust adsorption template for metal adatoms (50, 51). In the context of this thesis, this surface is attractive because it offers the possibility to directly probe the influence of the cation concentration and coordination on the surface reactivity, as different terminations can be prepared

## Chapter 1. Introduction

under precise control. The first objective was to study the structure of the different terminations that the surface offers via Fe deposition experiments. This allows to identify the surface defects present in our material and investigate their influence on adsorption. Thereafter, the influence of the defects and termination were probed using two important and representative organic compounds: methanol and formic acid. Finally, a preliminary study about the use of  $\text{Fe}_3\text{O}_4$  (001) surface in the water gas shift reaction is presented.





## 2. Experimental

This chapter introduces the fundamentals and technical aspects of the experimental techniques and instruments used during the development of this work.

### 2.1 X-ray Photoelectron Spectroscopy (XPS)

X-ray Photoelectron Spectroscopy, also known as Electron Spectroscopy for Chemical Analysis (ESCA), has become to one of the most useful and powerful methods in surface science analysis. The technique allows measurement of the chemical composition and electronic structure of a sample with high surface sensitivity (52).

XPS belongs to the family of electron spectroscopies, where electrons are the detected and analyzed particles. The technique is based on the photoelectric effect explained by Einstein (53).

Electrons from occupied states of atomic core levels, which have a binding energy ( $E_B$ ), are liberated into vacuum by absorption of a photon with energy ( $h\nu$ ). When the electron is ejected, it possesses a specific kinetic energy ( $E_{kin}$ ). This is represented in the equation:

$$E_B = h\nu - (E_{kin} + \phi) \quad [1]$$

Where  $\phi$  is the work function of the sample. Figure 2.1 shows a schematic representation of the photoemission process.

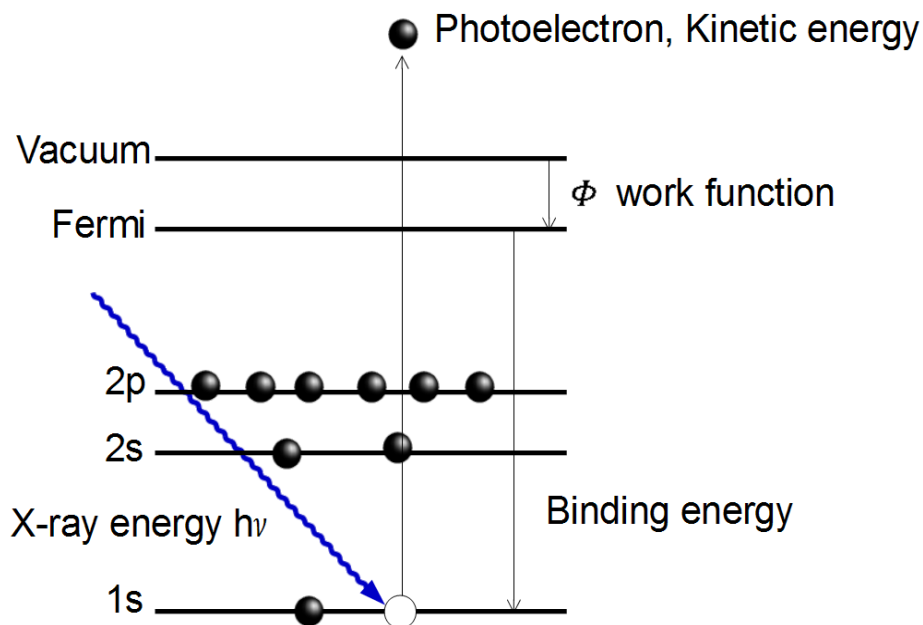


**Figure 2.1.** Schematic of the XPS process.

As every chemical element has a unique set of atomic orbitals, every element yields a characteristic set of peaks in the XPS spectra. The position of the peak provides information about the binding energy. An interesting aspect that makes XPS a powerful tool for investigations of surface phenomena such as adsorption and chemical reactions is the fact that the chemical surrounding affects the electronic structure of the atom, an effect known as chemical shift. Here, the shifts of the peaks offers information about the valence states of the atoms, while its shapes and the presence of satellites offers information related to their bonding environment.

As mentioned before, XPS is a surface sensitive technique. Although the X-rays penetrate deep into the sample, the distance which a photoelectron can travel through the sample without being inelastically scattered is only few Å.

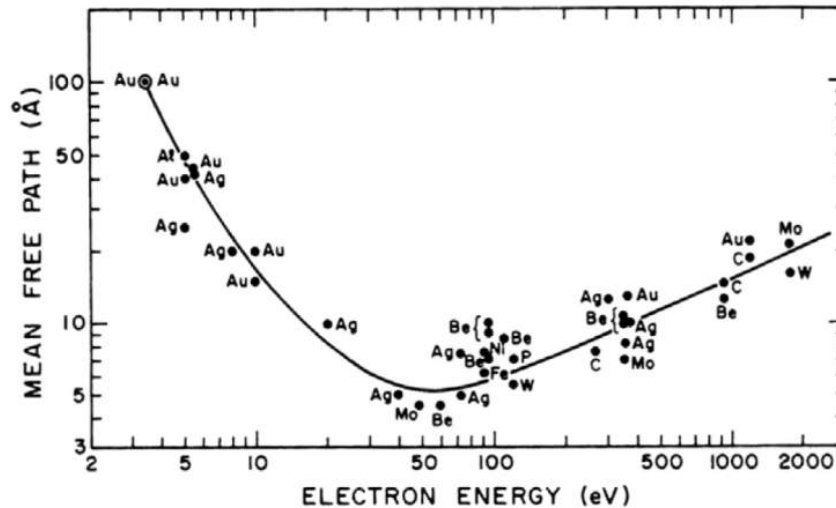


**Figure 2.2.** Empirical data of some inelastic mean free path for photoelectrons of different atoms (54).

The plot in Figure 2.2 shows the dependence in the inelastic mean free path of an electron with the kinetic energy. With kinetic energies in ranges between 10 to 1000 eV (typical energies in XPS), the mean free path is limited to distances below 3 nm.

In order to modify the surface sensitivity of the measurement, the emission angle of the detected electrons, hence the distance travelled in the sample, or the energy of the exciting photons is changed.

## 2.2 Temperature Programmed Desorption (TPD)

When species that have been adsorbed on surfaces gain enough energy from thermal vibrations to leave the surface, we are talking about thermal desorption. Such desorption has been described in terms of a desorption rate,  $r_{des}$ , which represents the number of particles desorbing from unit surface area per unit time. The desorption rate can be written as

$$r_{des} = \sigma^* f^*(\theta) e^{-(E_{des}/k_B T)} \quad [2]$$

Where  $f^*(\theta)$  describes the coverage dependence;  $\sigma^*$  is the desorption coefficient related to steric and mobility factors, and the term  $e^{-(E_{des}/k_B T)}$  is the temperature dependent Boltzmann term.

When it is assumed that the sites occupied by the adsorbed molecules are identical and the adsorbates species do not interact with each other, the desorption rate is given by the Polanyi- Wigner equation (4).

$$r_{des} = -\frac{d\theta}{dt} = k_n^0 \theta^n e^{-(E_{des}/k_B T)} \quad [3]$$

Where  $E_{des}$  is the activation energy of desorption,  $n$  the order of the desorption kinetics, and  $k_n^0$  the desorption rate constant (55). As is observed, the equation presents an Arrhenius equation form, which is typical for thermally activated processes, as the case of the desorption.

The kinetic order falls into three general cases, the zero, first and second order. In the zero order kinetics ( $n=0$ ), the desorption rate is independent of the coverage. Zero order takes place at the desorption of a homogeneous multilayer film.

In the first order ( $n=1$ ), the desorption rate is proportional to the coverage. This case correspond to desorption of single atoms directly from their adsorption sites. Here the rate constant appears in units of frequency,  $s^{-1}$ . This frequency has values on the order of atomic frequency of crystal lattices.

In the second order ( $n=2$ ), where the desorption rate is proportional to  $\theta^2$ . Here the desorbing molecule often originates from two fragments residing at separates sites, which have to join in order to desorb, this is commonly called associative molecular desorption. Where the rate constant  $k_n^1$  is in units of  $ML^{-1} s^{-1}$ .

The term  $E_{des}$  on the Polanyi- Wigner equation refers to the desorption energy, which is related with the activation barrier that the adsorbate species has to overcome in order to leave the surface.

The desorption energy values depend on the process that take place. Two main processes are considered: The activated chemisorption and the non-activated chemisorption. In the case of activated chemisorption, where exist a barrier for adsorption of the precursor state to a chemisorbed state, the desorption energy is the sum of the binding energy in the chemisorbed state and the activation energy for adsorption. While in the non-active chemisorption the desorption energy is just the binding energy in the chemisorbed state.

For the determination of these kinetics parameters, Temperature Programmed Desorption appears as powerful tool. In this technique, the temperature of the adsorbate-covered surfaces is increased, which promotes the desorption of the adsorbate. The desorption process induces increases of pressure, which are monitored as a function of temperature.

In TPD experiments, the sample is heated using a linear temperature ramp, defined as:

$$T(t) = T_0 + \beta t \quad [4]$$

where  $t$  is time and  $\beta$  is the heating rate, typically on the order of 1-10 K/s. The molecules desorbing from the surface are monitored with Quadrupol Mass Spectrometer (QMS).

TPD spectra show the desorption rate of the desorbed molecules with respect to the sample temperature. Analysis of these spectra offers information about the desorption mechanism, the strength of the bond between adsorbate and substrate, and its coverage. Figure 2.3 shows a series of TPD spectra calculated for the kinetic orders described above.

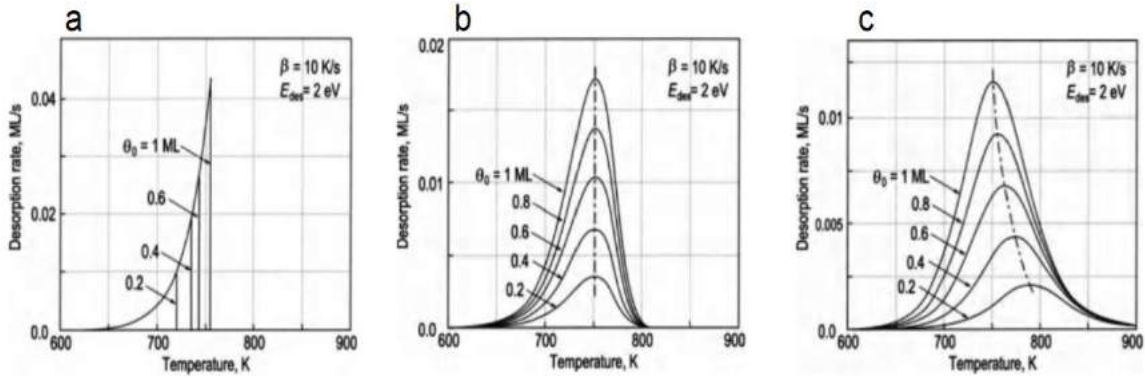


**Figure 2.3.** (Figure taken from ref. 4) TPD spectra calculated for zero order, first order, and second order desorption kinetics and various initial coverages.

For the zero order (Figure 2.3 a), the TPD curves present a common leading edge and rapid drop beyond the peak temperature ( $T_m$ ) for all the initial coverages. The peak temperature shifts to higher temperature with increasing the initial coverage  $\theta_0$ . Figure 2.3 b shows the TPD curves for the first order; here the peak has an asymmetric shape, while the  $T_m$  keeps the same position with increasing initial coverages. Finally for the second order (Figure 2.3 c) the TPD curves present a nearly symmetric shape, where the  $T_m$  moves to lower temperature with increasing the initial coverage. Nevertheless, the cases exposed above represent the ideal cases of desorption. Some complex kinetics would result in other order exponents of desorption (4).

The peak temperature,  $T_m$ , is related to the desorption energy. Different approximations have been postulated. For the case of first-order kinetics, a relationship between  $E_{\text{des}}$  and  $T_m$  has been established as (Redhead equation):

$$E_{\text{des}} = k_B T_m \left( \ln \frac{k_1 T_m}{\beta} - 3.64 \right) \quad [5]$$

Where  $\beta$  is the heating rate. Here it is assuming that  $E_{\text{des}}$  and  $k_1$  are coverage independent (56).

### 2.3 Scanning Tunneling Microscopy (STM)

The Scanning Tunneling Microscope (STM), developed by Binnig and Rohrer in the early 1980's, allows the visualization of a surface at the atomic scale (57, 58) .

The principle of STM is based on the quantum mechanical tunnel effect, which establishes that a particle is able to tunnel through a potential barrier under adequate conditions. In STM experiments, an atomically sharp tip (generally made of tungsten) is brought within a few nanometers of a conducting surface, where the potential barrier is represented by the vacuum between the two objects. Then a small potential difference is applied between the sample and the tip. Depending of the bias which is applied, a tunneling current is generated between the sample and the tip. If the tip is biased positively with respect to the sample an energetic incentive is provided for electrons from the sample to flow to the tip.

The magnitude of this current is exponentially dependent on the tip-surface separation. In this way, measuring the magnitude of the tunneling current as the tip is moved across the surface, can offer a topographic image of the surface.

The basic principle of the tunneling current can be described by a simple model where electrons are described by wave functions  $\psi(z)$  , which satisfy the 1D time-independent Schrödinger equation:

$$\left(\frac{-\hbar^2}{2m} \Delta + U(z)\right) \psi(z) = E\psi(z) \quad [6]$$

With  $m$ ,  $\hbar$ ,  $U$ , and  $E$  being the electrons mass, the reduced Plank constant, the height of the vacuum barrier, and the kinetic energy of the electron, respectively. The solution inside the vacuum barrier is an exponentially decreasing wave function:

$$\psi(z) \propto e^{-z\kappa} , \text{ with } \kappa = \sqrt{\frac{2m\Phi}{\hbar^2}} \quad [7]$$

where  $\Phi$  is the vacuum barrier. The tunneling current ( $I_t$ ), is proportional to the probability (T) for electrons tunneling through the vacuum barrier (width d):

$$I_t \propto T \propto |\psi(d)|^2 \propto e^{-2dk} \quad [8]$$

Here the expression shows that the tunneling current depends exponentially on the distance between the sample and the tip. Small changes in this distance cause big changes in the current.

The local density of states around the Fermi level of the tip and the sample, as well as the applied voltage affects the tunneling current. Figure 2.4 shows an schematics of electron tunneling in STM, for a tip close to a surface with work functions  $\Phi_{\text{tip}}$  and  $\Phi_{\text{sample}}$  respectively. Here, the electrons tunnel from the tip into empty states of the sample (positive sample bias).

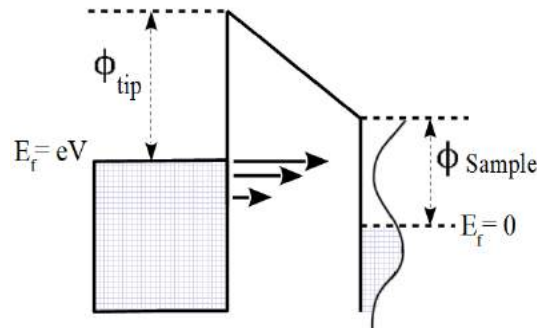


**Figure 2.4.** Schematic view of electron tunneling between tip and sample in STM (positive sample bias).

Figure 2.5 illustrates the typical components of a scanning tunnelling microscope. Commonly the microscope is operated in the constant current mode. Here, an electrochemically etched W tip is mounted on a piezoelectric scanner and is approached to the sample surface. The tunneling current is compared with a reference value, and the difference is amplified to move the z piezo. As the tip scan in the x-y plane of a sample the z piezo changes its height in order to keep constant the tunneling current.



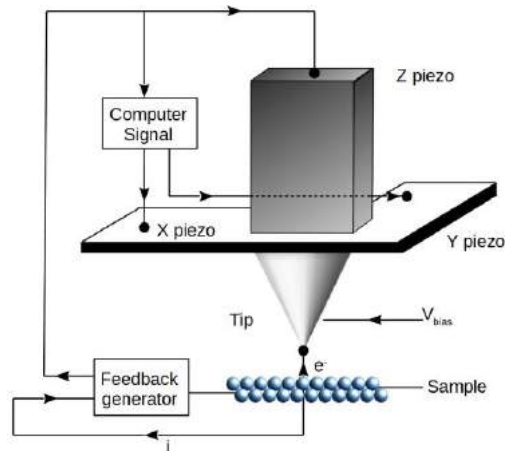


**Figure 2.5.** Schematic view of an scanning tunneling microscope.

## 2.4 Low Energy Electron Diffraction (LEED)

Low Energy Electron Diffraction has been one of the main techniques to study the long range periodicity of a crystal surface. The technique is part of the surface sensitive techniques, due to the mean free path of low energy electrons (Figure 2.2).

The de Broglie wavelength ( $\lambda$ ) of an electron is given by the equation:

$$\lambda = \frac{h}{\sqrt{2mE}} \quad [9]$$

Here, in the range of energies ( $E$ ), used in LEED (50-500 eV) the electrons have a wavelength in the range of 0.5 - 1.7 Å. These wavelength are on the order of the inter-atomic distances, which allows investigating the structure on the atomic scale.

When a crystal surface is bombarded with electrons, the wave fronts of the elastically scattered electrons can interfere with each other. In the case of constructive interference the following relation is satisfied.

$$n\lambda = a \sin \theta \quad [10]$$

where  $n$  is the order of the maximum,  $a$  the lattice constant and  $\theta$  the angle between the diffracted electrons and the sample normal.

An alternative way of representing the conditions for diffraction is in terms of reciprocal lattice vectors. In the reciprocal space, the conditions for constructive interference are given by:

$$\kappa - \kappa_0 = G_{hkl} \quad [11]$$

here,  $\kappa_0$  is the incidence wave vector,  $\kappa$  is the scattered wave vector, and  $G_{hkl}$  is the reciprocal lattice vector. Where  $|\kappa| = |\kappa_0|$  in elastic scattering.

For the case of diffraction on 2D surface, due to the lacking of crystal periodicity in the direction normal to the surface, the condition for constructive interference in the reciprocal space will be:

$$\kappa^{\parallel} - \kappa_0^{\parallel} = G_{hk} \quad [12]$$

The equation previously described refers to the Laue condition, which can be visualized using the Ewald's sphere construction. LEED spots are observed at any energy when the sphere intersects the diffraction rods.

In the experimental method, an electron source irradiates the surface with a beam of electrons with an energy in the range of 50 to 300 eV. The electrons are diffracted from the surface and are accelerated through grids, which also filter the inelastically scattered electrons, until they reach a fluorescent screen.

LEED pattern provides information about the periodicity of the surface unit cell from the position of the diffracted beams. From the variation of intensities with the beam energy it is possible to determine surface geometries. The diffraction pattern exhibits the presence of different domains and provides information about the homogeneity of the surface.

## 2.5 Infrared Reflection Absorption Spectroscopy (IRRAS)

Vibrational spectroscopy is a powerful tool for probing the bonding of atoms and molecules adsorbed on a surface. Infrared spectroscopy is probably the most suitable method to study the adsorption of different systems on surfaces.

The principle of infrared spectroscopy is based on the vibrational excitation of molecules by absorption of infrared light. The information of these vibrations is related to the chemical nature of the adsorbed molecules and its interaction with the substrate. Two groups of vibrations are commonly considered, the stretching vibrations and the bending vibrations. In the first case the vibration produces changes in bond length and in the second case correspond to changes in bond angles. Only vibrations that result in a change of the molecular dipole moment can be observed. Figure 2.6 shows a scheme of some molecular vibrations modes.

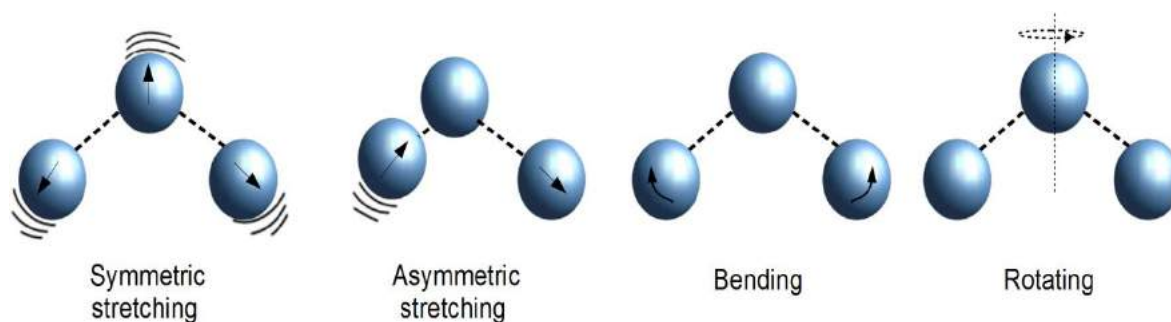


**Figure 2.6.** Molecular vibration modes in a molecule with three atoms.

The vibration modes will depend on the geometry of the molecule, for instance if the molecule is linear or nonlinear, and the number of atoms present in the molecule. In general the factor  $3n$  degrees of freedom (where  $n$  represent the number of atoms presents in the molecule) describes the motion of a molecule in relation to the coordinates  $(x,y,z)$ . This factor also describe the translational, rotational, and vibrational motions of the molecule.

In IRRAS the vibration of molecules adsorbed on surfaces are obtained in reflection mode. The process of reflection at a surface is analyzed by evaluating

the behavior of two polarization components, the s component, with its electric field polarized parallel to the surface and perpendicular to the direction of the propagation, and the p component, which is perpendicular to the s component and to the line of propagation as is shown in figure 2.7. When the reflection process occurs the magnitude and the direction of the electric field related with both components change. An adsorbed molecule on the surface will be affected for the fields due to the incident and reflected beams (59).

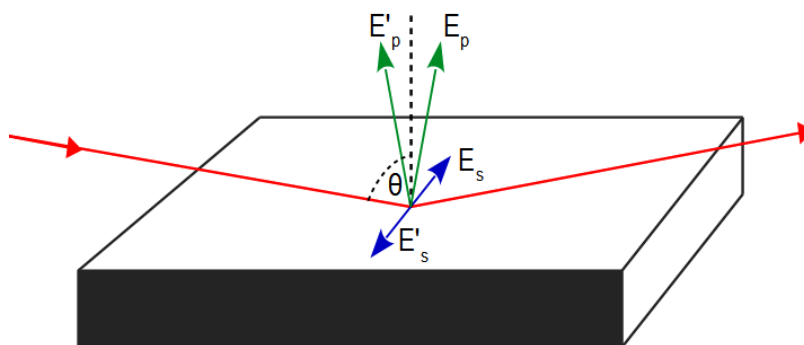


**Figure 2.7.** Scheme of the electric vector of s and p-polarized radiation incident on a surface at an angle  $\theta$  to the normal.

As is observed in figure 2.7 the electric vectors  $E_s$  and  $E'_s$  are canceled as they are equals and opposites. This come from the fact that the direction of the s component is reversed on reflection. In the case of the p component its behavior will depend on the angle of incidence  $\theta$ . Here, the sensitivity is maximized by employing high angles of incidence.

As was described, the absorption of IR light by a molecule adsorbed on a surface is influenced by the dielectric behavior of the surface. On metallic surfaces the electric field of the incident light and the dipole moment of the adsorbed molecule interact with the metal electrons. These interactions have been explained following a set of rules known as metal surface selective rule, which can be enunciated as follows (60):

- (1) Only vibrations with a dynamic dipole moment component perpendicular to the surface will be excited.
- (2) The incident light should be reflected at the metal surface at grazing incidence.

The vibrational spectrum of adsorbed molecules can give relevant information about the system under study. The spectrum allows the identification of the adsorbate state (atomic, molecular, intermediates), and determination of the molecular symmetry and the surface-adsorbate bond.

### 2.6 Experimental Setups

The experiments presented in this thesis were performed mainly in two different ultrahigh vacuum (UHV) systems. A short description is given in this section.

#### 2.6.1 OMEGA System.

The OMEGA system is a UHV setup that consists of two chambers, the load lock and the main chamber, with a base pressure below  $5 \times 10^{-8}$  mbar and  $1 \times 10^{-11}$  mbar, respectively. The load lock employs two different pumps, a scroll pump and a turbo molecular pump. The main chamber employs four pumps: a scroll pump, a turbo molecular pump, an ion pump and a titanium sublimation pump (TSP).

Figure 2.8 shows a schematic model of the main facilities that the system offers, including an Omicron UHV-STM-1, Omicron LEED, sample heating stage (resistive heating up to 700 °C) Omicron ISE-10 rasterable ion gun, SPECS PHOIBOS 100 analyser and an SRS RGA-100 residual gas analyzer. Temperatures were measured with a K-type thermocouple attached to the sample manipulator.

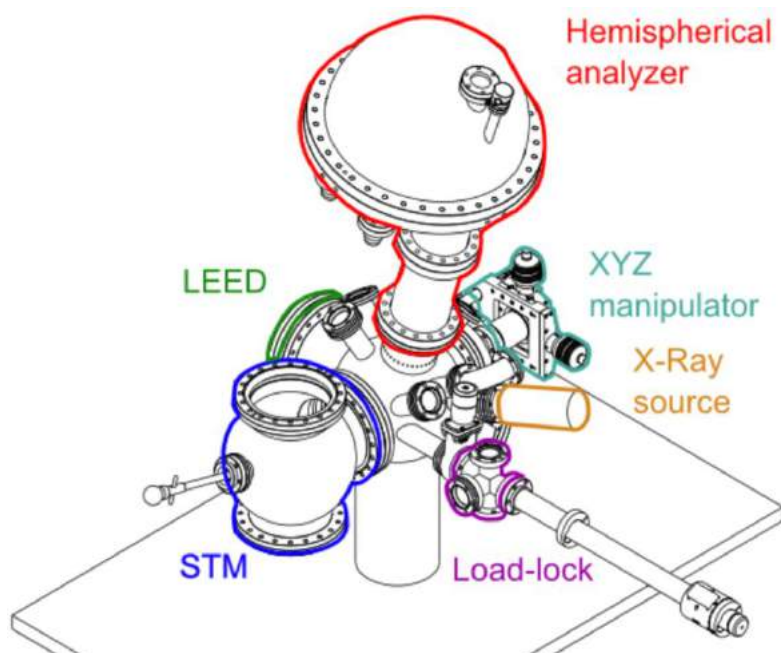


**Figure 2.8.** Schematic view of OMEGA system.

### 2.6.2 The Machine for Reactivity Studies "The Mrs."

The Machine for Reactivity Studies, is a home-built UHV setup designed to investigate surface chemistry of metal oxide samples. It has a base pressure of  $\approx 10^{-10}$  mbar. The machine is equipped in order to carry out different surface analyses such as, TPD, UPS (Ultra Violet Photoemission Spectroscopy), XPS, and Low-Energy Ion Scattering Spectroscopy.

Figure 2.9 shows a schematic of the Machine for Reactivity Studies. To carry out XPS measurements the system includes an SPECS Phoibos 150 MCD hemispherical analyzer. The X-ray source is a SPECS XR50M with an Al anode. To obtain X-ray radiation with an energy of 1486.74 eV and a line width of 0.4 eV, a Focus 500 monochromator was used.

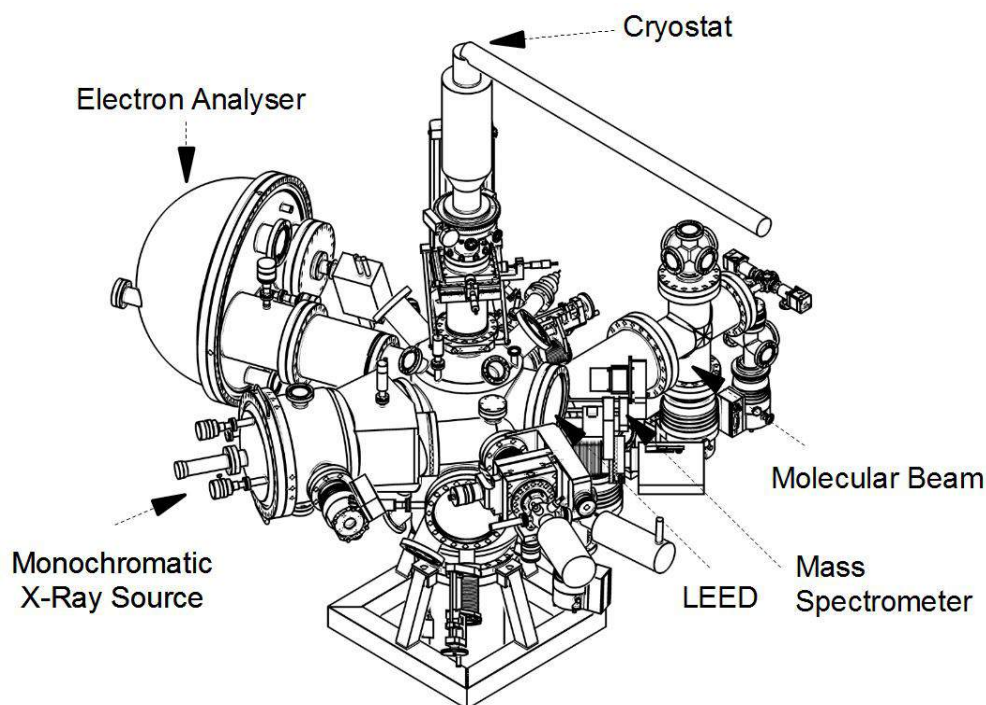


**Figure 2.9.** Schematic view of The Machine for Reactivity Studies.

TPD experiments were performed using a HIDEN HAL/3F RC 301 PIC quadrupole mass spectrometer (QMS). The sample was cooled by a Janis ST-400 UHV liquid-He flow cryostat, and heated by direct current at a rate of 1 K/s through a Ta back plate, on which the sample was mounted. The temperature was measured by a K-type thermocouple, and the sample was biased at -100 V during TPD measurements to prevent electrons from the QMS filament from reaching the sample. To dose molecules onto the surfaces of the sample, the chamber has a molecular beam doser, which enables precise and reproducible exposures to a defined area on the sample surface (61).

### 2.6.3 IRRAS Measurements

IRRAS measurements shown in this thesis were performed by our collaborators Dr. Heshmat Noei and Prof. Andreas Stierle in a third UHV-system at DESY, Germany that is equipped with an IR spectrometer Bruker Vertex 80v (Bruker Optics, Ettlingen, Germany) coupled to the UHV chamber via differentially pumped

KBr-windows. Each IR spectrum was accumulated in 1024 scans with a resolution of  $2\text{ cm}^{-1}$  and was taken with the unpolarized beam at an incidence angle of  $80^\circ$  at a base pressure of  $5 \times 10^{-10}$  mbar.

### 2.7 Sample Preparation

The samples used in the present work were  $\text{Fe}_3\text{O}_4$  (001) natural single crystals from SurfaceNet GmbH. The crystals were mounted onto Ta Omicron-type sample plates using two stripes of flat Ta wire that are shaped into clips, which uniformly press the sample and are fixed by spotwelding the ends to the Ta plate. When the sample is in ultrahigh vacuum is prepared *in-situ* by 1 keV  $\text{Ar}^+$  sputtering at room temperature for 20 minutes followed by annealing in UHV at 873 K for 15 minutes. Once no contamination could be detected by XPS in the C1s region, the sample was annealed in  $\text{O}_2$  ( $5 \times 10^{-7}$  mbar) at 873 K for 15 minutes.

### 2.8 Evaporation Materials

Iron was evaporated from a 2-mm-thick rod (99.99 + %, MaTeck GmbH) with the  $\text{Fe}_3\text{O}_4$  sample at room temperature using an Omicron electron-beam evaporator; the deposition rate was calibrated by a quartz crystal microbalance.

### 2.9 Liquids and Gases

Formic acid and methanol were obtained from Sigma Aldrich at a purity of 99.9 and 99.8% respectively. Both were purified with several freeze-pump-thaw cycles. On the OMEGA system the molecules were dosed into the chamber through a high-precision leak valve. For the machine for reactivity studies the dosing was performed with an effusive molecular beam source. Formaldehyde was prepared by thermal decomposition of paraformaldehyde (Aldrich, 95%) at  $80\text{ }^\circ\text{C}$  after extensive outgassing.



## 3. Iron Oxides

As one of the transition metals, iron (Fe) has the ability to form different oxidized compounds, some of them used by humanity since a long time ago. These compounds exist as oxides, hydroxides or oxy-hydroxides with or without hydration water.

These compounds show different properties. Iron oxides can be semiconductors, conductors or insulators; paramagnetic, ferromagnetic, or antiferromagnetic. These properties depend on the crystal structure, which varies from the amorphism of limonite, the hexagonal structure of ferrosilite, and the orthorhombic structure of goethite, to the spinel structure of magnetite.

Within the oxides, three are the most common forms: Hematite ( $\alpha\text{-Fe}_2\text{O}_3$ ), the stable oxide phase under oxidizing conditions, where the iron has an oxidation state of 3+. In reducing conditions wustite (FeO) is formed with rocksalt structure and all the iron atoms with oxidation state of 2+, and magnetite ( $\text{Fe}_3\text{O}_4$ ), a mixed valence metal oxide (38).

### 3.1 Magnetite, $\text{Fe}_3\text{O}_4$

Magnetite, described by the general formula  $\text{AB}_2\text{O}_4$ , belongs to the inverse spinel family. Figure 3.1 shows the bulk unit cell of magnetite. The structure shows a mixed valence oxide, with both  $\text{Fe}^{2+}$  and  $\text{Fe}^{3+}$  present in the fcc oxygen lattice, with a lattice unit cell of 8.397 Å. The  $\text{Fe}^{3+}$  cations occupy tetrahedral interstitial sites (FeA), while the octahedral interstitial sites (FeB) are occupied by a mixture of  $\text{Fe}^{2+}$  and  $\text{Fe}^{3+}$  cations (1:1) at room temperature.

The magnetite bulk unit cell can be understood as a stack of two different atomic layers which are alternatively repeated in the (001) direction. The A layer consist of two iron atoms with tetrahedral coordination per unit cell, and the B layer consist

of four iron atoms with octahedral coordination and eight oxygen anions per unit cell.

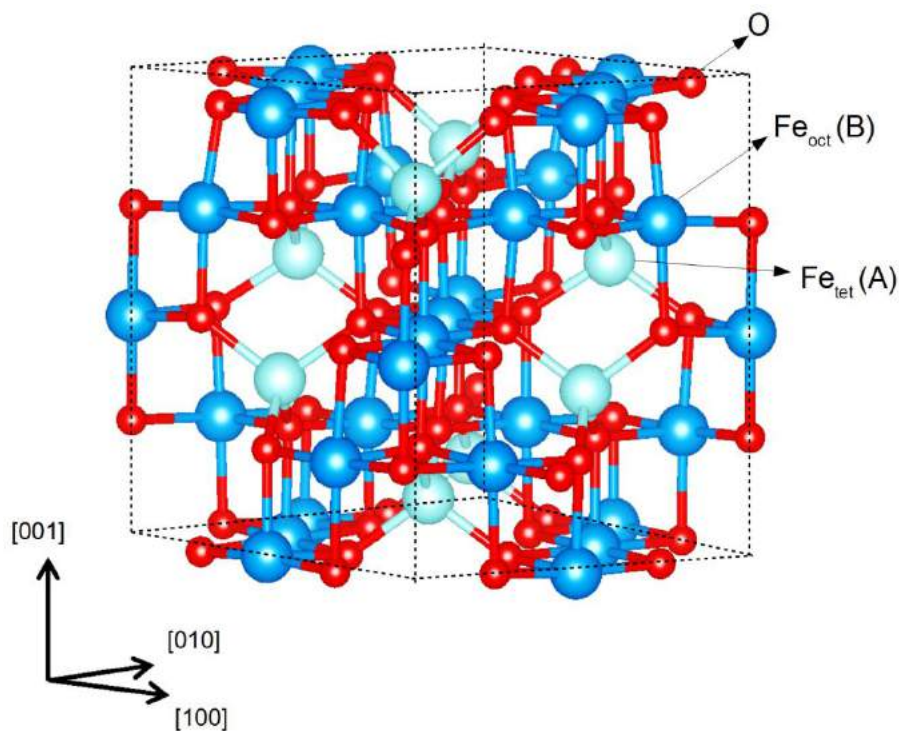


**Figure 3.1.** Inverse spinel bulk unit cell of Fe<sub>3</sub>O<sub>4</sub>, consisting of an oxygen fcc lattice with iron in interstitial positions.

At 125 K, the material undergoes a metal-insulator transition, the Verwey transition. The transition represents a drop in conductivity and changes in the magnetic and structural properties (62-64). Above this temperature, the material is predicted to be a half-metal (64).

Magnetite represents the iron oxide most used as catalyst. It is an industrially important material, used as catalyst in the Fischer-Tropsch synthesis (49), in the decomposition of hydrogen peroxide (65), and is the active phase in catalytic systems used in the water gas shift reaction (46, 66).

### 3.2 The Fe<sub>3</sub>O<sub>4</sub> (001) Surface

As mentioned above, magnetite consists of alternating planes (A layer and B layer) in the (001) direction. This corresponds to a Tasker type 3 polar surface, where a non-zero net dipole moment perpendicular to the surface is present. In line with this, a surface reconstruction is expected (67, 68). A  $(\sqrt{2}\times\sqrt{2})R45^\circ$  reconstruction has been observed experimentally (69-71).

Previously the surface structure for the Fe<sub>3</sub>O<sub>4</sub> (001) surface was explained in terms of distorted bulk truncation (DBT) (71, 72). Here the symmetry was explained by subtle lateral relaxations of the surface octahedral irons and O atoms. The alternating, lateral relaxation of pairs of Fe atoms in a direction that is perpendicular to the octahedral iron rows leads to a wave-like undulation of the rows (Figure 3.2). This reconstruction creates two non-equivalent sites for Fe<sub>tet</sub> (A) bulk continuation sites of the reconstructed surface. The model predicts that Fe<sub>oct</sub> (B) atoms in the surface and the Fe<sub>tet</sub> (A) atoms in the subsurface layer are Fe<sup>3+</sup>, while the subsurface Fe<sub>oct</sub> (B) atoms contains alternating pairs of Fe<sup>2+</sup> and Fe<sup>3+</sup> cations, ordered with the  $(\sqrt{2}\times\sqrt{2})R45^\circ$  symmetry.

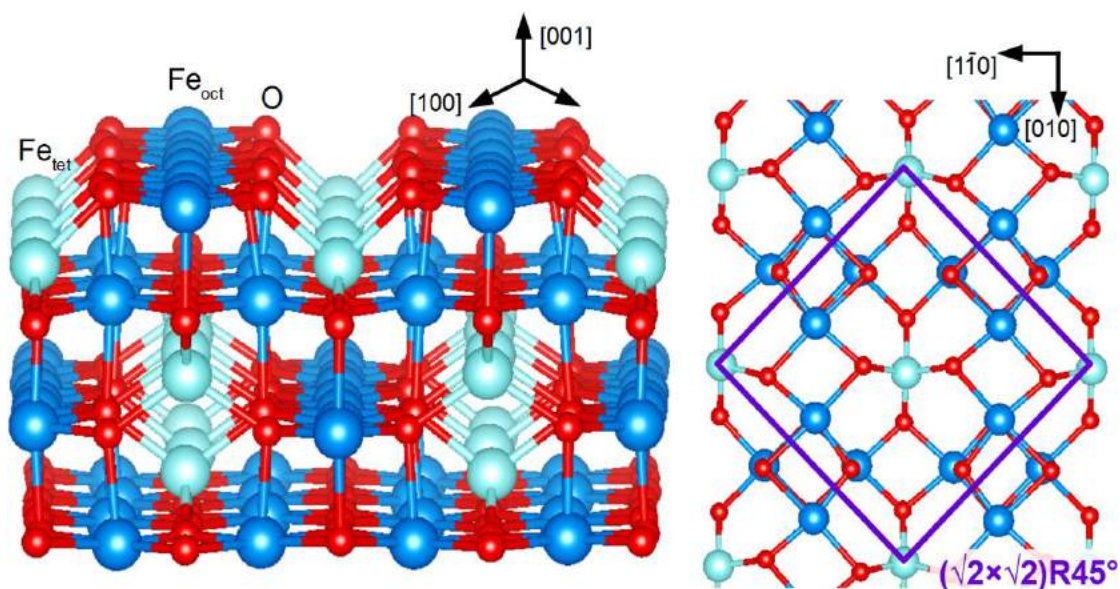


**Figure 3.2.** Perspective and top views of the distorted bulk truncation model of the Fe<sub>3</sub>O<sub>4</sub>(001)- $(\sqrt{2}\times\sqrt{2})R45^\circ$  surface.

Recently our group used a combination of quantitative low-energy electron diffraction, scanning tunneling microscopy, and density functional theory calculations, to propose a new surface structure of the  $\text{Fe}_3\text{O}_4(001)-(\sqrt{2}\times\sqrt{2})R45^\circ$  reconstruction (37). Quantitative measurements of the agreement between experimental and theoretical LEED IV curves, the Pendry R-factor ( $R_p$ ), shows best-fit structure achieved ( $R_p = 0.125$ ) for the new model over the value obtained for the distorted bulk truncation model ( $R_p = 0.34$ ) (37).

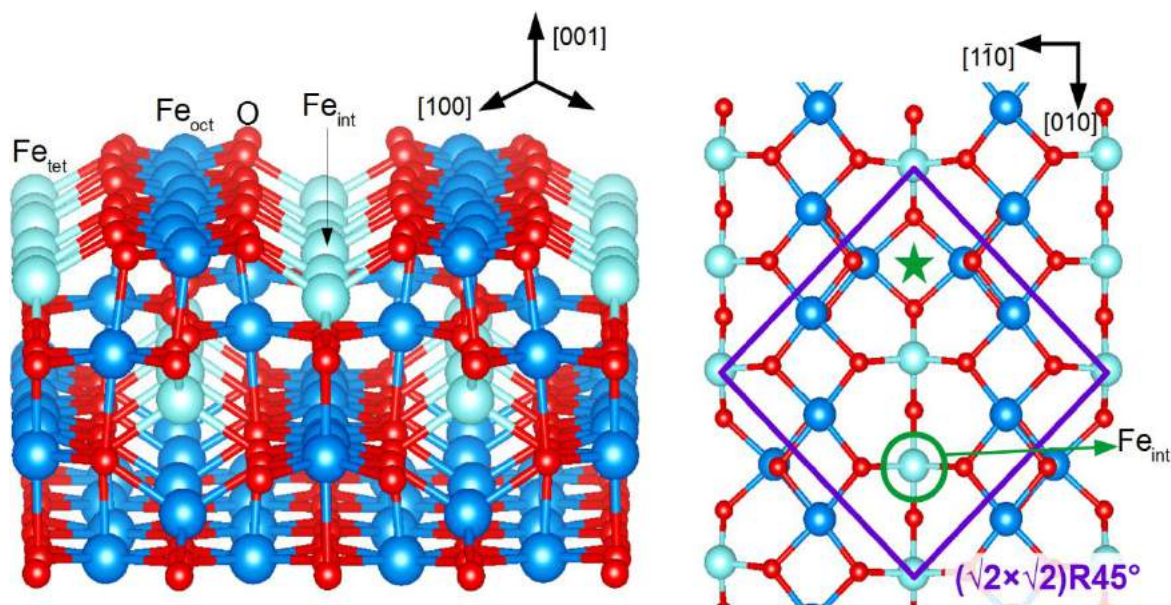


**Figure 3.3.** Perspective and top views of the subsurface cation vacancy structure of the  $\text{Fe}_3\text{O}_4(001)-(\sqrt{2}\times\sqrt{2})R45^\circ$  surface.

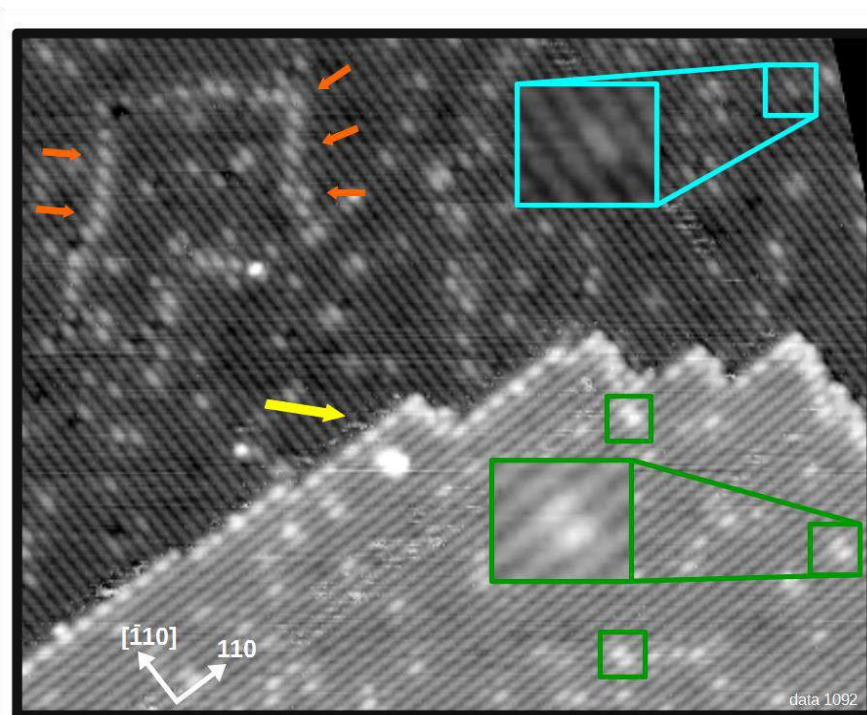
Figure 3.3 shows the perspective and top views of the  $\text{Fe}_3\text{O}_4(001)-(\sqrt{2}\times\sqrt{2})R45^\circ$  structure. Here, the  $(\sqrt{2}\times\sqrt{2})R45^\circ$  periodicity emerges from replacing two octahedral iron ( $\text{Fe}_{\text{oct}}$ ) from the third layer by an interstitial tetrahedral coordinated iron in the second layer (labelled  $\text{Fe}_{\text{int}}$  in figure 3.3). This new structure has received the name subsurface cation vacancy (SCV) structure.

The reorganization that occurs in the subsurface results in a wave-like undulation in the  $\text{Fe}_{\text{oct}}$  rows on the surface. The new model predicts that all Fe atoms in the four outermost layers are  $\text{Fe}^{3+}$ . This reconstruction creates two non-equivalent bulk

continuation sites per  $(\sqrt{2}\times\sqrt{2})R45^\circ$  until cell. One of them with an  $\text{Fe}_{\text{tet}}$  (interstitial iron atom) underneath, and the other site without this interstitial iron atom (green star figure 3.3).

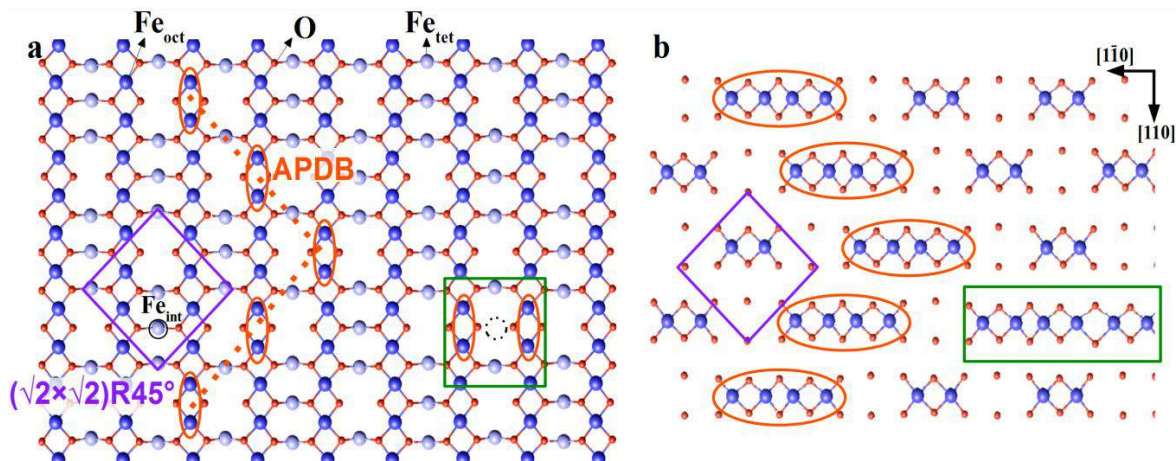
### 3.3 Typical Defects on the $\text{Fe}_3\text{O}_4$ (001) Surface

Figure 3.4 shows an STM image of the clean  $\text{Fe}_3\text{O}_4(001)$  surface. The surface exhibits rows of protrusions separated by 5.9 Å, related to octahedral iron atoms within the subsurface cation vacancy (SCV) reconstruction (37). Surface oxygen atoms are not imaged as there are no O-derived states in the vicinity of the Fermi level (37). A step edge runs across the centre of the image from left to right, separating two adjacent terraces (yellow arrow). The apparent step height of 2.1 Å corresponds to the spacing between equivalent planes in the bulk structure (73). The direction of the iron rows is perpendicular when going from one terrace to the next (73), consistent with the inverse spinel structure of magnetite. As reported previously (73), steps that run parallel to the Fe rows on the upper terrace are generally straight, whereas perpendicular steps are often jagged.



**Figure 3.4.** STM images of the as-prepared  $\text{Fe}_3\text{O}_4$  (001)- $(\sqrt{2}\times\sqrt{2})\text{R}45^\circ$  surface ( $39 \times 31 \text{ nm}^2$ ;  $V_{\text{sample}} = +1.7 \text{ V}$ ;  $I_{\text{tunnel}} = 0.3 \text{ nA}$ ). The surface exhibit typical defects labeled as follows: An antiphase domain boundary (APDB) is visible as a row of protrusions in the lower terrace (indicated by the orange arrows). The bright protrusion on the Fe rows highlighted by the cyan box is due to a surface hydroxyl. The green boxes highlight pairs of bright features located on neighboring Fe rows, attributed to additional subsurface Fe. The yellow arrow indicates a step edge.

A schematic model of the outermost three layers of the the  $\text{Fe}_3\text{O}_4(001)-(\sqrt{2}\times\sqrt{2})\text{R}45^\circ$  surface with the most common defects on the surface is shown in Figure 3.5. The two outermost layers are shown in panel (a) and the third layer in panel (b).



**Figure 3.5.** Schematic model of defects at the  $\text{Fe}_3\text{O}_4(001)$ - $(\sqrt{2} \times \sqrt{2})R45^\circ$  surface. The outermost two layers are shown in panel (a) and the third layer in panel (b). The  $(\sqrt{2} \times \sqrt{2})R45^\circ$  unit cell, indicated by the purple square, contains four  $\text{Fe}_{\text{oct}}$  atoms (big balls, dark blue) and eight O atoms (small balls, red) in the surface layer, and three  $\text{Fe}_{\text{tet}}$  atoms in the second layer (big balls, light blue). The  $\text{Fe}_{\text{tet}}$  indicated by the black circle is an interstitial ( $\text{Fe}_{\text{int}}$ ) linked to the subsurface cation vacancy (SCV) reconstruction. The interstitial replaces two  $\text{Fe}_{\text{oct}}$  atoms in the third layer, such that there are only two  $\text{Fe}_{\text{oct}}$  per unit cell instead of four. The dotted orange line indicates an antiphase domain boundary in the SCV reconstruction. The pairs of surface  $\text{Fe}_{\text{oct}}$  atoms indicated by orange ovals at the boundary appear bright in STM images. Note that four  $\text{Fe}_{\text{oct}}$  are present in a row in the third layer beneath the APDB (see panel b). The green boxes highlight a defect in which an additional  $\text{Fe}_{\text{oct}}$  atom is incorporated in the third layer, which causes  $\text{Fe}_{\text{int}}$  to relocate to the other  $\text{Fe}_{\text{oct}}$  vacancy position, as will be described below. Note that because six  $\text{Fe}_{\text{oct}}$  are present in a row in the third layer beneath this defect, it appears as a double protrusion in STM images (orange ovals). The black dashed circle represents the position for a missing  $\text{Fe}_{\text{int}}$  in the second layer.

### 3.3.1 Line Defects on the Fe<sub>3</sub>O<sub>4</sub> (001) Surface

The step edge structures for the Fe<sub>3</sub>O<sub>4</sub> (001) surface are not definitively known. Following the procedure of Henrich (73), we have reevaluated the step stability in terms of covalent stability (coordinative unsaturation) for the SCV reconstructed surface. As mentioned above, two different groups of step edges for the Fe<sub>3</sub>O<sub>4</sub> (001) surface are considered, with edges parallel or perpendicular to the octahedral iron atoms rows of the upper terrace, the  $\alpha$  and  $\beta$  type respectively.

The most stable step parallel to the Fe<sub>oct</sub> rows (denoted B- $\alpha^*$  by Henrich) is terminated with the O atoms (Figure 3.6a). All other configurations expose Fe<sub>oct</sub> atoms with three dangling bonds at each atom, which are likely more reactive. Perpendicular to the rows several different configurations are similarly stable, and all expose both, Fe<sub>oct</sub> atoms with three dangling bonds per atom, and Fe<sub>tet</sub> atoms, which have two dangling bonds (one example is shown in Figure 3.6b).

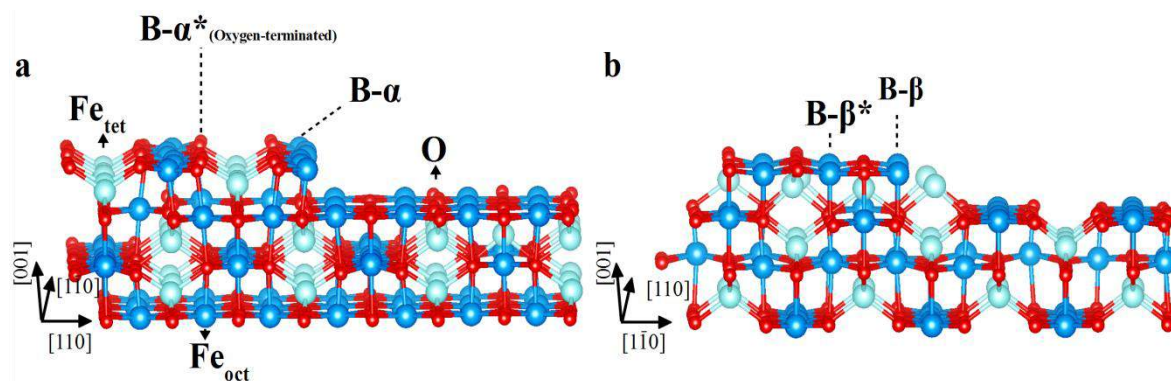


**Figure 3.6.** Structural models of step edges for the Fe<sub>3</sub>O<sub>4</sub>(001) surface. (a) Steps parallel to the iron ion rows along [1 $\bar{1}$ 0] (B- $\alpha$  type). (b) Steps perpendicular to the iron ion rows along [110] (B- $\beta$  type). Labels after ref. (73)

A second, extended defect that is frequently observed on the freshly prepared surface is the antiphase domain boundary (APDB) (74), indicated by orange arrows in Figure 3.4 and dotted orange line in Figure 3.5. This feature appears as a chain of bright protrusions located on the Fe<sub>oct</sub> rows, and is typically aligned at 45° with respect to the row direction (74). The APDBs probably arise because the



$(\sqrt{2}\times\sqrt{2})R45^\circ$  reconstruction is lifted during each annealing cycle (75), and then renucleates on cooling through 723 K with one of two distinct registries with respect to the underlying bulk. The structure of the antiphase domain boundaries has been previously interpreted in terms of the distorted B-layer model for the  $(\sqrt{2} \times \sqrt{2}) R 45^\circ$  reconstruction in which a lattice distortion couples to charge order in the subsurface layers (74).

The SCV reconstruction creates two different bulk continuation sites per  $(\sqrt{2} \times \sqrt{2}) R 45^\circ$  unit cell. One of them blocked by interstitial  $Fe_{tet}$  atom, and the other site which remain non blocked, the four  $Fe_{oct}$  atoms in a row in the third layer are related with the junction of non blocked sites (Figure 3.5).

Interestingly, with no  $Fe_{int}$  in the second layer and four  $Fe_{oct}$  atoms in a row in the third layer, the local structure at the APDB is similar to a bulk truncated surface (Figure 3.2).

### 3.3.2 Point Defects on the $Fe_3O_4$ (001) Surface

In addition to the line defects, two types of point defects are observed. Surface hydroxyl groups appear in STM as bright protrusions located on the Fe rows (cyan box in Figure 3.4). These species were identified through the adsorption of atomic H on this surface (76), and have also been observed following dissociative adsorption of water (77). They are easily distinguished from other defects as they exhibit a characteristic hopping between opposite Fe rows in STM movies collected at room temperature. It is important to note that the OH group is a H atom adsorbed on a surface O atom, although it appears as increased brightness of a pair on adjacent Fe atoms. This is an electronic effect, as the OH donates charge to the neighboring Fe atoms, which makes them brighter in STM (77).

The green boxes (Figure 3.4) highlight pairs of bright features located on neighboring Fe rows. At first glance these features appear similar to hydroxyl groups, but they have a different apparent height (50 pm, compared to 20 pm for

the OH) and they do not exhibit the characteristic hopping behavior described above.

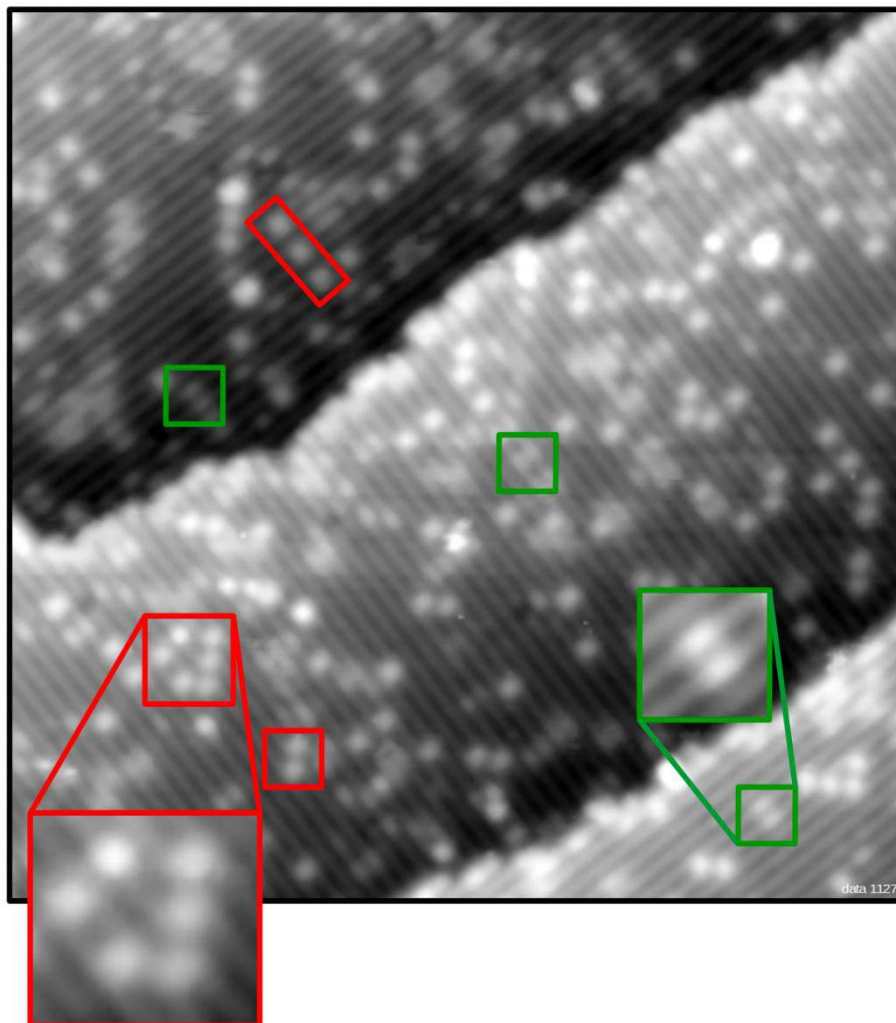


**Figure 3.7.** STM image ( $30 \times 30 \text{ nm}^2$ ,  $V_{\text{sample}} = 1.9 \text{ V}$ ,  $I = 0.2$ ) after deposition of 0.2 ML Fe at RT. Fe adsorbs as adatoms (red boxes) and incorporates in the subsurface (green boxes)

Figure 3.7 shows the surface after deposition of 0,2 ML of Fe (1 ML is defined as one atom per  $(\sqrt{2}\times\sqrt{2})R45^\circ$  unit cell, i.e.,  $1.42 \times 10^{14}$  atoms/cm<sup>2</sup>). The surface exhibits the characteristic rows of protrusions separated by 5.9 Å, related to octahedral iron atoms of the SCV reconstructed surface. Fe adatoms are observed, as reported previously (78), which appear as bright protrusions between the Fe rows (red boxes). The appearance of the Fe protrusions is similar to those observed for adatoms of Ag, Pd and Au (50, 51, 79).

A second group of features, which are highlighted with green boxes, appear as a pair of protrusions located on neighboring iron rows. It is known that Ni, Co, Ti and Zr enter the subsurface, filling one Fe<sub>oct</sub> vacancy in the third layer of the SCV reconstruction, which induces the Fe<sub>int</sub> to move and occupy the other vacancy. At 1 ML coverage this results in a (1×1) symmetry (80). Based on this, it is natural to propose that deposited Fe atoms can also enter the surface, and locally lift the SCV reconstruction.



## 4. Fe-Dimer Surface

Understanding the factors that control the surface terminations of metal oxides is important considering its implications on surface reactivity. It is documented that the  $\text{Fe}_3\text{O}_4$  (001) surface presents more than one termination, depending on the preparation conditions (81). In addition to the SCV termination described previously,  $\text{Fe}_{\text{tet}}$  terminated surfaces were initially proposed by STM analysis, because an array of bright protrusions with  $(\sqrt{2} \times \sqrt{2})R45^\circ$  periodicity was observed on sputtered and UHV-annealed samples. Such a surface would in principle compensate polarity by providing a surface layer with a charge of +3 electrons (81). However, XPS measurements on this surface revealed an enhanced  $\text{Fe}^{2+}$  contribution, rather than  $\text{Fe}^{3+}$  as expected for this  $\text{Fe}_{\text{tet}}$  (81). Moreover, this  $\text{Fe}_{\text{tet}}$  surface appears to be unstable; using molecular dynamics simulations it was demonstrated that subsurface  $\text{Fe}_{\text{tet}}$  atoms migrate to the surface to form an Fe dimer (70).

This Fe-dimer configuration has been validated by STM analysis, where the protrusions have been resolved into pairs of protrusions located between the  $\text{Fe}_{\text{oct}}$  rows (82-84). Different models have been proposed to assign the position of the Fe atoms in the dimer configuration, which are shown in Figure 4.1. One of these models suggest that the dimer is located above a subsurface  $\text{Fe}_{\text{tet}}$  vacancy (Figure 4.1a) (70), whereas studies of  $\text{Fe}_3\text{O}_4$  (001) epitaxial films on Fe(001) buffer layer on MgO (001) suggested that the Fe-dimer is located on a bulk terminated surface, but with the dimer straddling one of the subsurface  $\text{Fe}_{\text{tet}}$  atoms (Figure 4.1b) (85, 86).

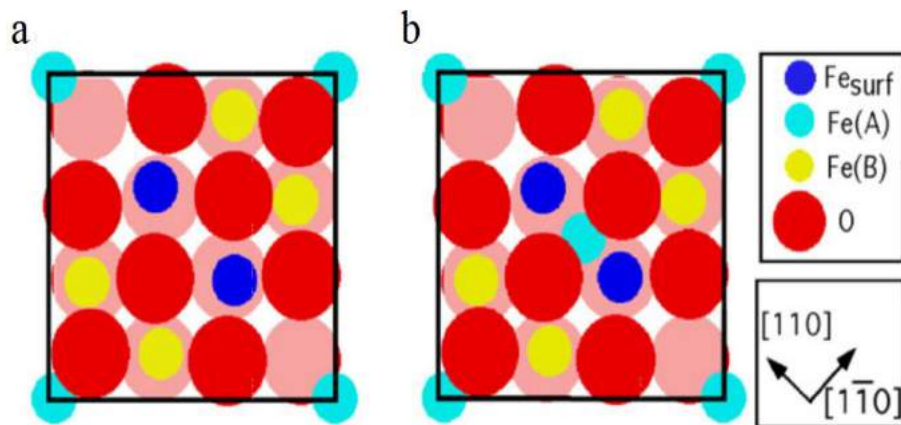


**Figure 4.1.** Models for the Fe-Dimer configuration. a) Model proposed in reference (70). b) Model proposed in reference (85, 86)

Deposition of Fe on the  $\text{Fe}_3\text{O}_4$  (001) surface has been proposed in order to study directly the structure of the Fe-rich terminations (78). Previously, work from our group suggested that the dimer atoms are located in fourfold hollow sites between subsurface  $\text{Fe}_{\text{tet}}$  atoms. Nevertheless, in the light of new experimental evidence and the subsurface cation vacancy model for the  $\text{Fe}_3\text{O}_4(001)-(\sqrt{2}\times\sqrt{2})R45^\circ$  surface (37), a new interpretation is proposed.

#### 4.1 Fe Deposition at Room Temperature: Effect of Oxygen

Figure 4.2a shows an STM image acquired after deposition of Fe on the clean surface. The image shows the presence of a high density of Fe clusters. These clusters were reported by Novotny et al. (78) during the Fe deposition experiments and were attributed to excess of Fe on the surface (78). In the new experiments the formation of Fe clusters was observed at very low coverages, so control experiments were carried out to determine the cause. Here it will be demonstrated that the clusters result from a reaction of Fe atoms with  $\text{O}_2$  present in the residual gas following preparation of the clean  $\text{Fe}_3\text{O}_4(001)$  surface. Figure 4.2a shows the result of the Fe deposition with oxygen intentionally leaked into the background during Fe deposition at a pressure of  $1\times 10^{-9}$  mbar.

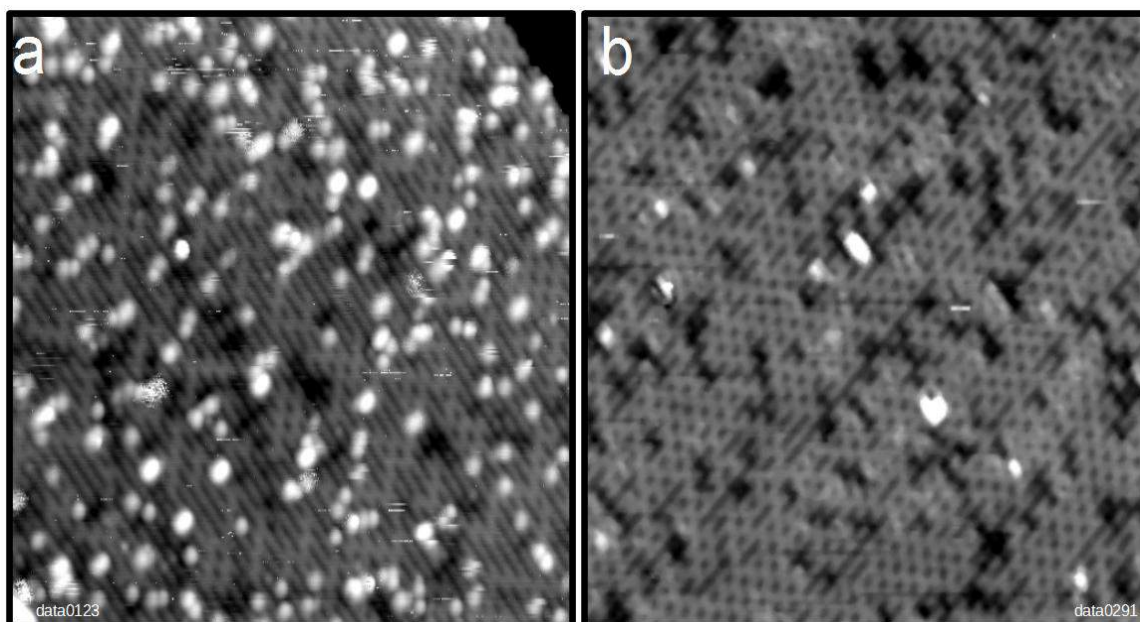


**Figure 4.2.** (a) STM image ( $30 \times 30 \text{ nm}^2$ ,  $V_{\text{sample}} = 1.5 \text{ V}$ ,  $I = 0.3$ ) after deposition of 2 ML Fe with oxygen in the background ( $1 \times 10^{-9}$  mbar  $\text{O}_2$  during deposition). (b) STM image ( $30 \times 30 \text{ nm}^2$ ,  $V_{\text{sample}} = 1.5 \text{ V}$ ,  $I = 0.3$ ) after deposition of 2 ML Fe (deposition of Fe in good vacuum, after TSP cycles)

In order to avoid this situation for the Fe deposition experiments described hereafter, several TSP cycles were made before Fe deposition to decrease the pressure of  $\text{O}_2$ . During the titanium sublimation, reactive components of the residual gas, as is the case for oxygen, react with a titanium thin layer on the walls, forming stable compounds.

Figure 4.2b shows an STM image acquired after deposition of Fe after TSP cycles. Clearly the cluster density is dramatically reduced, so we propose the clusters to be Fe oxide in nature, formed through the reaction with molecular  $\text{O}_2$  at the surface.

## 4.2 Fe Deposition: From Fe Adatom to the Fe-Dimer Surface

Figure 4.3 shows STM images of the  $\text{Fe}_3\text{O}_4$  (001) surface acquired after deposition of different coverages of Fe onto a clean surface at room temperature. Here, 1 ML is defined as one atom per  $(\sqrt{2}\times\sqrt{2})R45^\circ$  unit cell, i.e.,  $1.42 \times 10^{14}$  atoms/cm<sup>2</sup>. (The following experiments were carried out after TSP cycles).

Figure 4.3a shows the surface after deposition of 0.2 ML of Fe, which was described in the previous chapter.

After deposition of 0.6 ML Fe (Figure 4.3b), the number of adatom features (around 0.1 ML) is less than the deposited amount and the density of the features located directly at the Fe rows increases. In addition, a new configuration is observed in the STM images (yellow square), where new protrusions located between the Fe rows appear. The protrusions are spaced by 12 Å along the  $\text{Fe}_{\text{oct}}$  row and due their appearance were assigned to Fe-dimers. Previously, similar features were atomically resolved with STM showing two atoms per each dimer configuration (78). According to DFT+U calculations for the bulk truncation model, the Fe atoms of the "dimer" are fourfold coordinated to surface oxygen atoms, filling two of the four octahedral interstitial sites per unit cell, and no Fe-Fe bond is formed (78).

After deposition of 1 ML, the  $\text{Fe}_{\text{oct}}$  rows of the underlying substrate remain visible in some areas. The density of regions with Fe-dimers increases, and the dimers are distributed with  $(\sqrt{2}\times\sqrt{2})R45^\circ$  symmetry. In some areas single Fe adatoms coexist with Fe dimers. Figure 4.3d shows an STM image acquired following deposition of 2 ML Fe onto the clean  $\text{Fe}_3\text{O}_4(001)$  surface. The image shows a high density of Fe dimers with  $(\sqrt{2}\times\sqrt{2})R45^\circ$  symmetry as is highlighted in the inset with a yellow grid overlay.

The inset in figure 4.3e shows an atomically resolved STM image, where the protrusion of the dimer appear directly between the  $\text{Fe}_{\text{oct}}$  atoms of the neighboring rows (Image adapted from Ref. (78)). This atomically resolved image resembles the configurations shown in Figure 4.3c and Figure 4.3d (red square).



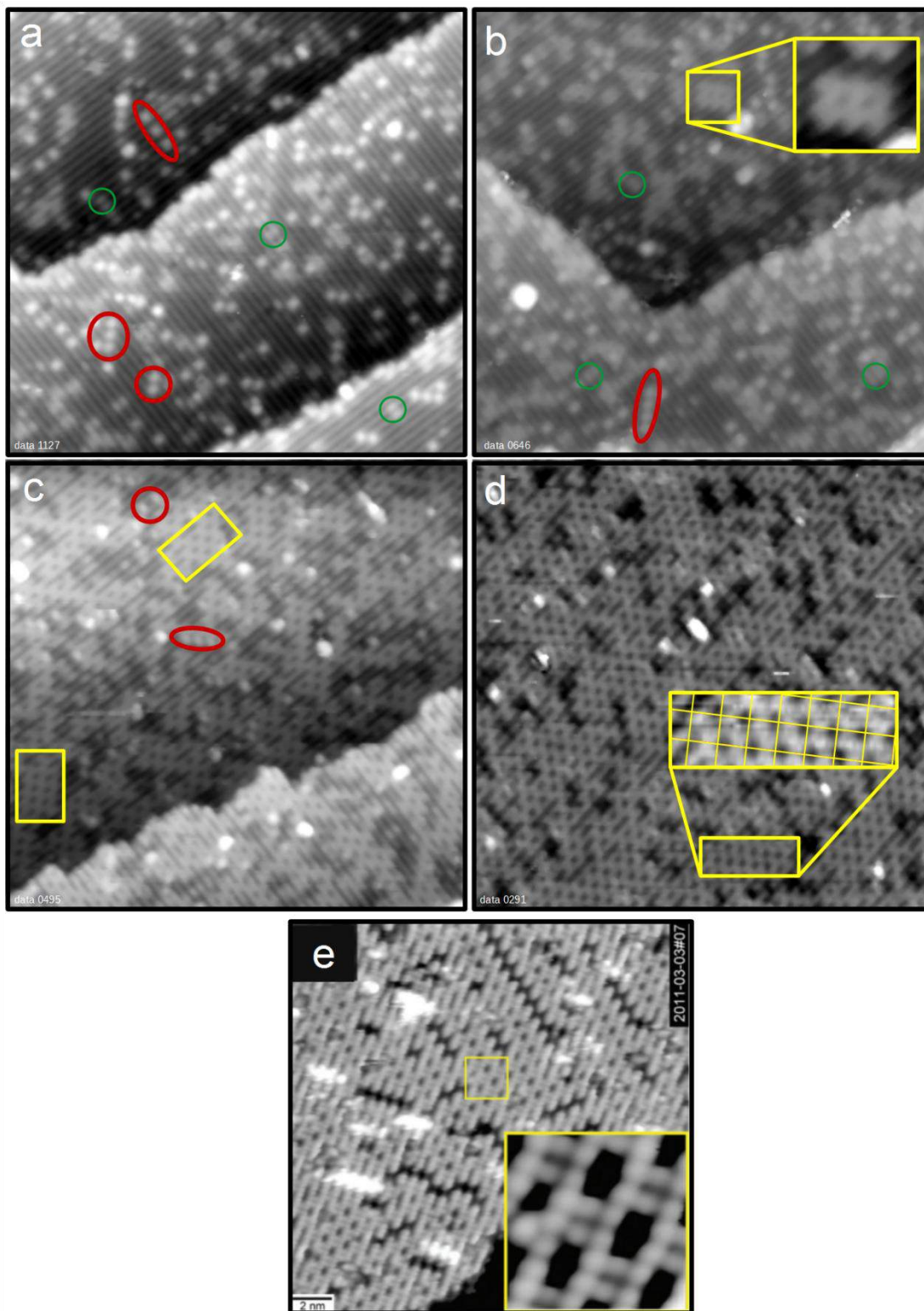


**Figure 4.3.** STM images of different coverage of Fe on the  $\text{Fe}_3\text{O}_4$  (001) surface at room temperature. (a) STM image ( $30 \times 30 \text{ nm}^2$ ,  $V_{\text{sample}} = 1.9 \text{ V}$ ,  $I = 0.2$ ) after deposition of 0.2 ML Fe at RT. Fe adsorbs as adatoms (red ovals) and incorporates in the subsurface (green circles). (b) STM image ( $30 \times 30 \text{ nm}^2$ ,  $V_{\text{sample}} = 1.7 \text{ V}$ ,  $I = 0.3$ ) after deposition of 0.6 ML Fe. Fe is present in a new configuration, the Fe-Dimer (yellow square). (c) STM image ( $30 \times 30 \text{ nm}^2$ ,  $V_{\text{sample}} = 1.9 \text{ V}$ ,  $I = 0.3$ ) after deposition of 1 ML Fe. The density of Fe-Dimer patches increases with some Fe adatoms. (d) STM image ( $30 \times 30 \text{ nm}^2$ ,  $V_{\text{sample}} = 1.5 \text{ V}$ ,  $I = 0.3$ ) after deposition of 2 ML Fe (Fe-Dimer surface). (e) STM image ( $20 \times 20 \text{ nm}^2$ ,  $V_{\text{sample}} = 1.0 \text{ V}$ ,  $I = 0.3$ ) after deposition of 0.7 ML Fe. (inset) High resolution STM image of the area obtained within the yellow rectangle (Adapted from Ref (78)).

### 4.3 XPS

The reduction of the surface due to Fe deposition is visible in the XPS. Figure 4.4 shows Fe 2p and O 1s core level spectra for the clean and the Fe-dimer surface. The high-resolution data were acquired using a SPECS FOCUS 500 monochromatic source and a SPECS PHOIBOS 150 electron analyzer at normal emission with a pass energy of 18 eV in the Mrs chamber. Similar XPS data were acquired in the OMEGA system (not shown)

For the clean surface the dominant contribution to the spectrum comes from the  $\text{Fe}^{3+}$  cations, since this is the only oxidation state present in the four outermost layers (37). The Fe-Dimer surface exhibits an enhanced  $\text{Fe}^{2+}$  component at 708.7 eV in the  $\text{Fe}2p_{3/2}$  peak, and an  $\text{Fe}^{2+}$  related satellite peak at 714 eV.

The clean  $\text{Fe}_3\text{O}_4(001)$  surface exhibits a slightly asymmetric O 1s peak at 530.1 eV due to the lattice oxygen in magnetite as reported previously (87). For the Fe-

Dimer surface the peak has the same shape, but shifts 0.2 eV to higher binding energy.

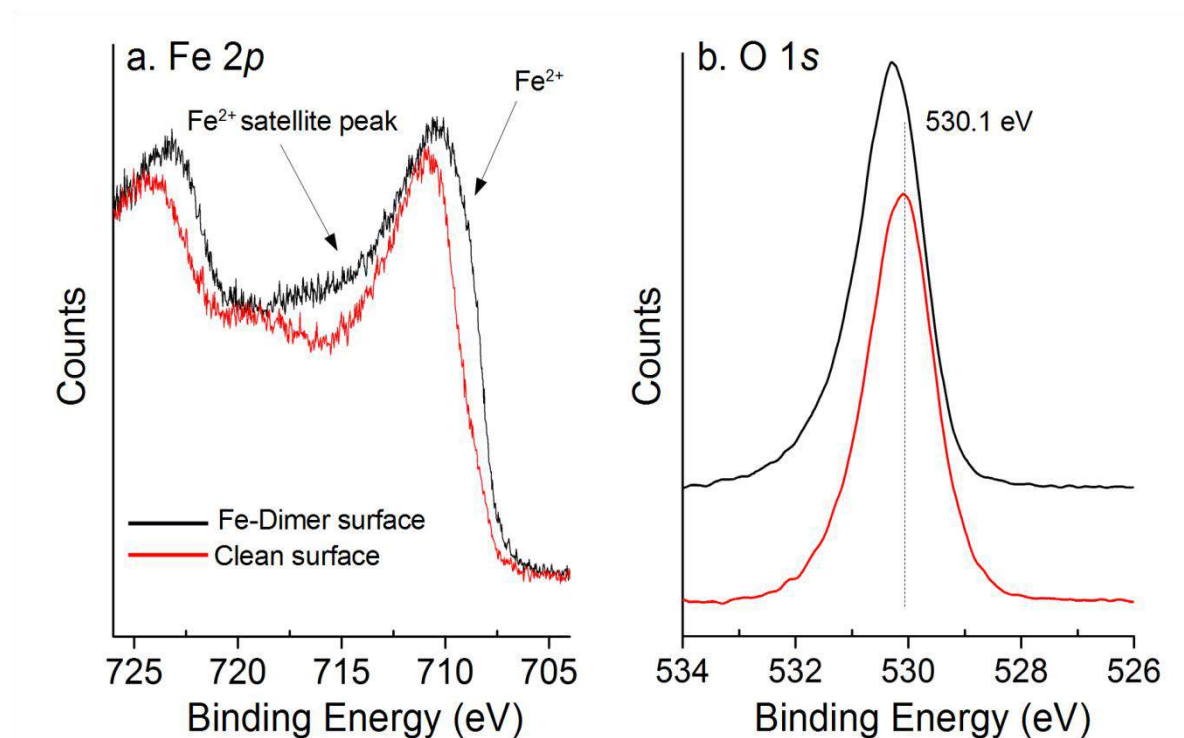


**Figure 4.4.** Fe 2*p* (a) and O 1*s* (b) XPS spectra before (red) and after (black) the deposition of 2.0 ML Fe on the clean Fe<sub>3</sub>O<sub>4</sub>(001)-( $\sqrt{2} \times \sqrt{2}$ )R45° surface at room temperature.

#### 4.4 Thermal Stability of the Fe-Dimer Surface

In order to evaluate the thermal stability of the Fe-Dimer surface, temperature dependent XPS experiments were carried out. Figure 4.5 shows O 1*s* and Fe 2*p* photoemission spectra that were recorded after 2 ML of Fe was deposited on the clean Fe<sub>3</sub>O<sub>4</sub>(001) surface and subsequently annealed to progressively higher temperatures.

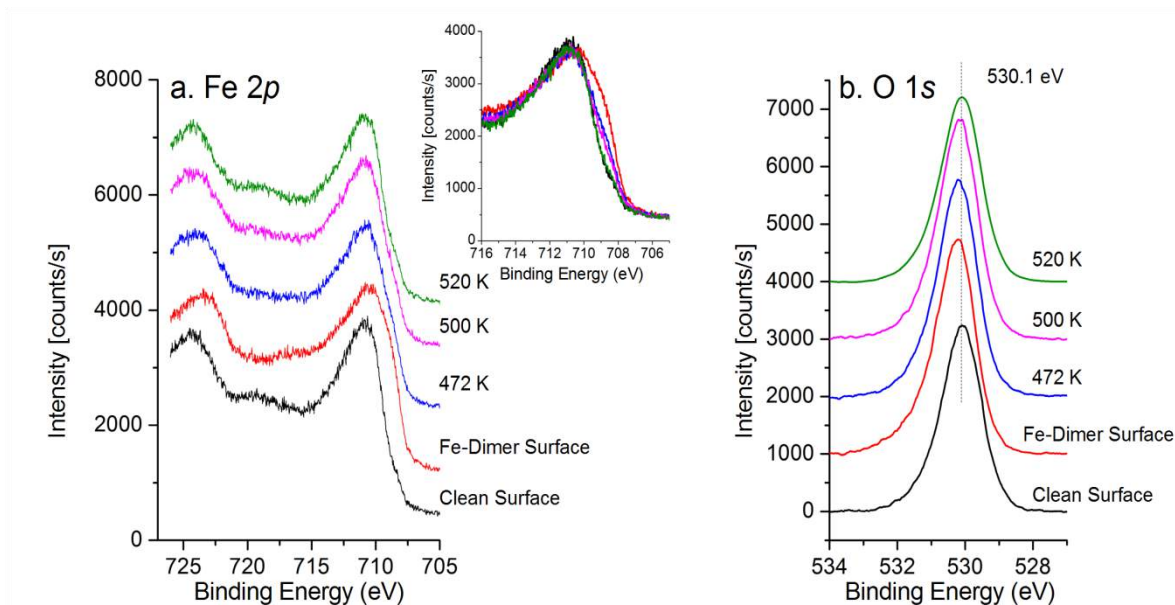


**Figure 4.5.** Fe2*p* and O1*s* XPS spectra from 2 ML Fe deposited on the Fe<sub>3</sub>O<sub>4</sub>(001)-( $\sqrt{2} \times \sqrt{2}$ )R45° surface at room temperature and annealed as indicated. The data are offset in the y-direction while the spectra in the inset were superimposed for clarity.

The Fe2*p* spectra are shown in Figure 4.5a. The Fe-Dimer surface exhibits an enhanced Fe<sup>2+</sup> shoulder as mentioned above (red), as well as shifting of the lattice oxygen peak to high binding energy in comparison with the clean sample (Figure 4.5b).

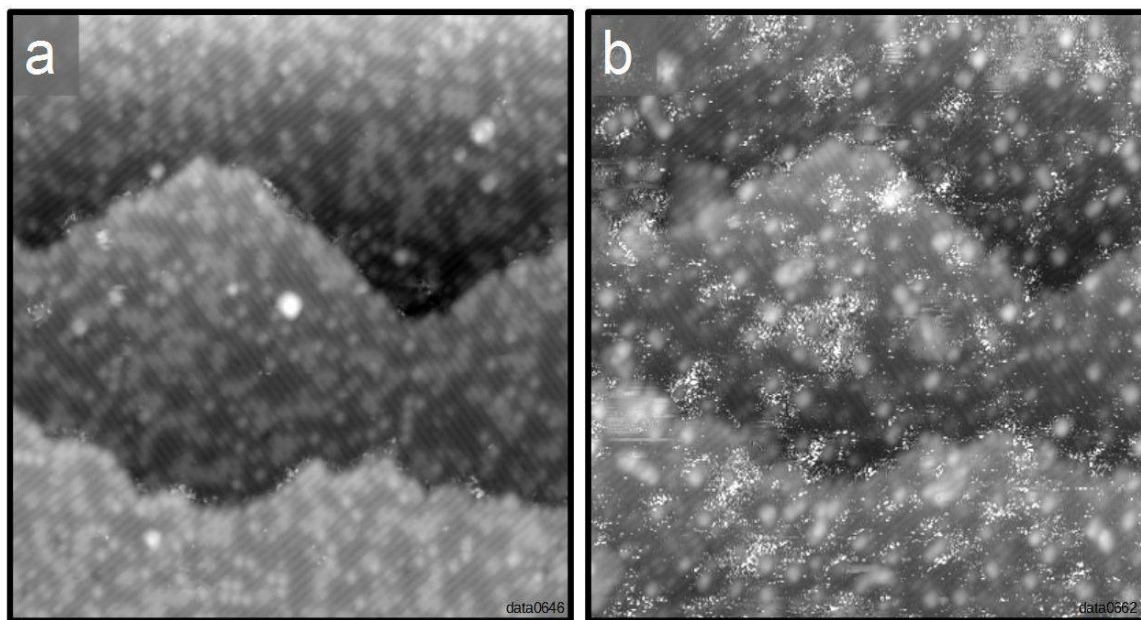
As the sample is heated to progressively higher temperatures the intensity of the Fe<sup>2+</sup> contributions i.e., signals around 708.7 eV and 714 eV decreased. By 520 K, the obtained spectra resemble the spectra for the clean surface (compare inset in Fig. 7.4a, black and green spectra). At the same temperature, the lattice oxygen peak recovers its original position at 530.1 eV. These changes are related with the diffusion of Fe into the bulk (88).

Similar results were observed in STM. The surface keeps the Fe-Dimer configuration until 523 K, annealing at higher temperature showed a clean Fe<sub>3</sub>O<sub>4</sub>(001)-( $\sqrt{2} \times \sqrt{2}$ )R45° surface.

#### 4.5 Fe-rich (001) Surface: Reactivity to Oxygen

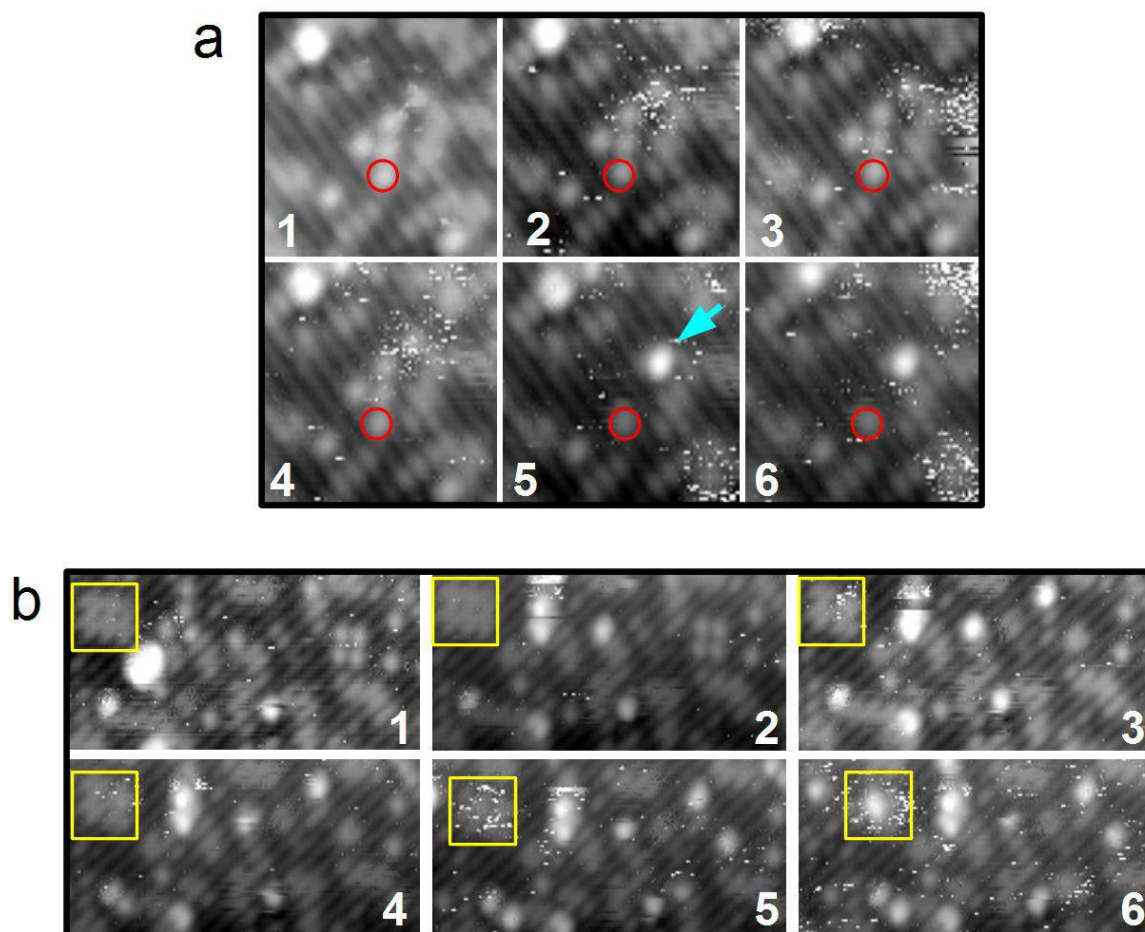
As discussed previously the presence of oxygen during the iron deposition induces the formation of Fe clusters. Here the reactivity of the as-prepared Fe-rich  $\text{Fe}_3\text{O}_4$  (001)- $(\sqrt{2}\times\sqrt{2})\text{R}45^\circ$  surface to oxygen will be discussed in more detail.

Figure 4.6a shows the surface after deposition of 0.6 ML of Fe, the surface exhibits the features described above: iron adatoms, Fe incorporated in the subsurface, and Fe dimers. Exposing the surface to oxygen ( $3 \times 10^{-9}$  mbar  $\text{O}_2$ ) for a time period of 1 hour and 20 minutes (10.8 Langmuir) (Figure 4.6b), leads to an increase of white features associated with clusters, while the species obtained after iron desposition decreases. Fuzzy areas are present on the image, which typically is the result of molecules moving on the surface.



**Figure 4.6.** The effect of  $\text{O}_2$  exposure on Fe-rich surface. (a) STM image after deposition of 0.6 ML Fe at RT. (b) After exposure to  $\text{O}_2$ . Clusters have formed. Scanning details (both images):  $(40 \times 40) \text{ nm}^2$ ,  $V_{\text{sample}} = +1.7 \text{ V}$ ,  $I = 0.3 \text{ nA}$ .

Figure 4.7 shows two panels from different areas of the surface during the same experiment. Each panel has six selected frames from sequential STM images. The panel a focuses on the behavior of the Fe adatoms during the exposition of oxygen ( $3 \times 10^{-9}$  mbar  $O_2$ ). Between frame 1 and 4 (corresponding to a time span of 22 minutes), the surface did not show any changes. Then, in the frame 5 the three adatoms nearby to the Fe adatom labeled with the red circle disappear while an iron cluster emerges, which is indicated with the cyan arrow.



**Figure 4.7.** The effect of  $O_2$  exposure on Fe-rich surface. STM images selected from sequential STM images (a) ( $7.6 \times 7.6$  nm<sup>2</sup>,  $V_{\text{sample}} = +1.7$  V,  $I = 0.3$  nA). (b) ( $16 \times 8$  nm<sup>2</sup>,  $V_{\text{sample}} = +1.7$  V,  $I = 0.3$  nA. Image details: Omega-STM: from data 0647 until data 0652.

In panel b, the yellow box highlights a small patch of Fe-Dimers. As in the case of Fe adatoms, the formation of clusters is observed from the dimer configuration due to the presence of oxygen. This phenomenon appears to be related with the induced mobility of Fe adatoms by oxygen, a similar process as was observed during the adsorption of CO on a Pd adatoms on  $\text{Fe}_3\text{O}_4(001)$  (51).

The oxidation of the Fe-rich surface due to oxygen exposure is visible in XPS. Figure 4.8 shows Fe  $2p$  and O  $1s$  core level spectra for the Fe-Dimer surface, the surface after exposure to 10 L of  $\text{O}_2$ , and subsequent annealing to 472 K.

The Fe  $2p$  spectra are shown in Figure 4.8a. After that Fe-Dimer surface is exposed to oxygen the spectra loses its  $\text{Fe}^{2+}$  component at 708.7 eV in the  $\text{Fe}2p_{3/2}$  peak and the satellite peak at 714 eV. For the O  $1s$  region (Figure 4.8b), the lattice oxygen peak recovers the position for the clean  $\text{Fe}_3\text{O}_4(001)-(\sqrt{2}\times\sqrt{2})\text{R}45^\circ$  surface at 530.1 eV. Subsequent annealing to 472 K not does induce any changes with respect to the oxidized surface.

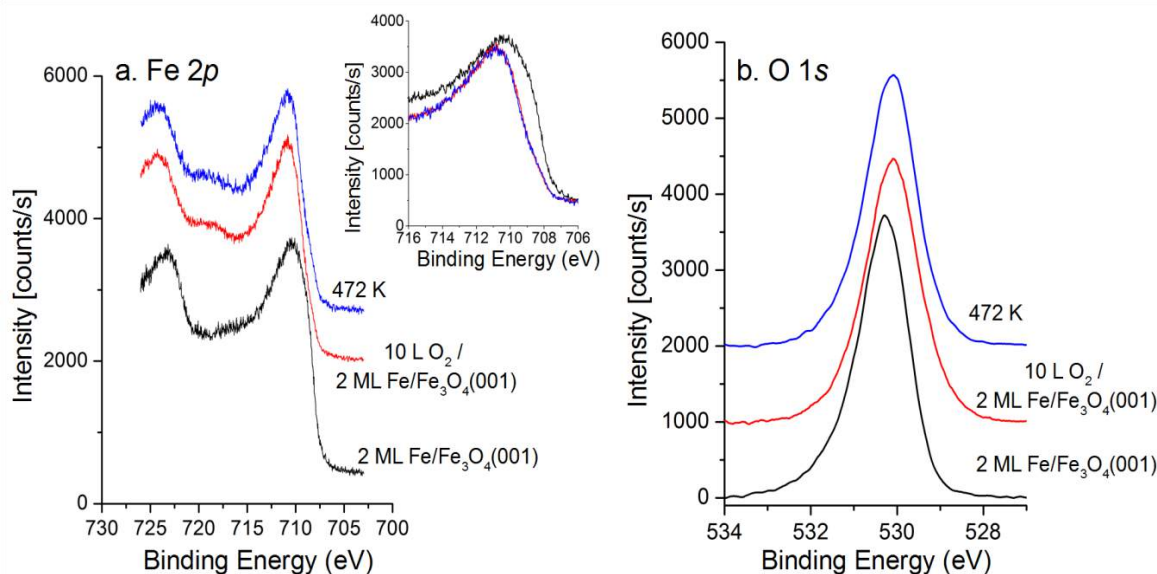


**Figure 4.8.** Fe $2p$  (a) and O $1s$  (b) XPS spectra from 2 ML Fe deposited on the  $\text{Fe}_3\text{O}_4(001)-(\sqrt{2}\times\sqrt{2})\text{R}45^\circ$  surface at room temperature (black line). After exposure of 10 L of oxygen (red line), and annealed at 472 K (blue line) The data are offset in the y-direction for clarity.

## 4.6 Discussion

Our results suggest that for low coverage of Fe ( $\leq 0.3$  ML) deposited at room temperature, Fe is present on two configurations; as a single  $\text{Fe}_{\text{tet}}$  adatoms and as Fe atoms incorporated in the subsurface, which locally lifts the  $(\sqrt{2} \times \sqrt{2})R45^\circ$  reconstruction. When the coverage is increased the density of patches due to unreconstructed unit cells increases while the density of adatoms decreases. At this point, the Fe dimers start to nucleate on the unreconstructed patches until the Fe-Dimer surface is achieved after the deposition of 2 ML of Fe with few SCV reconstructed areas.

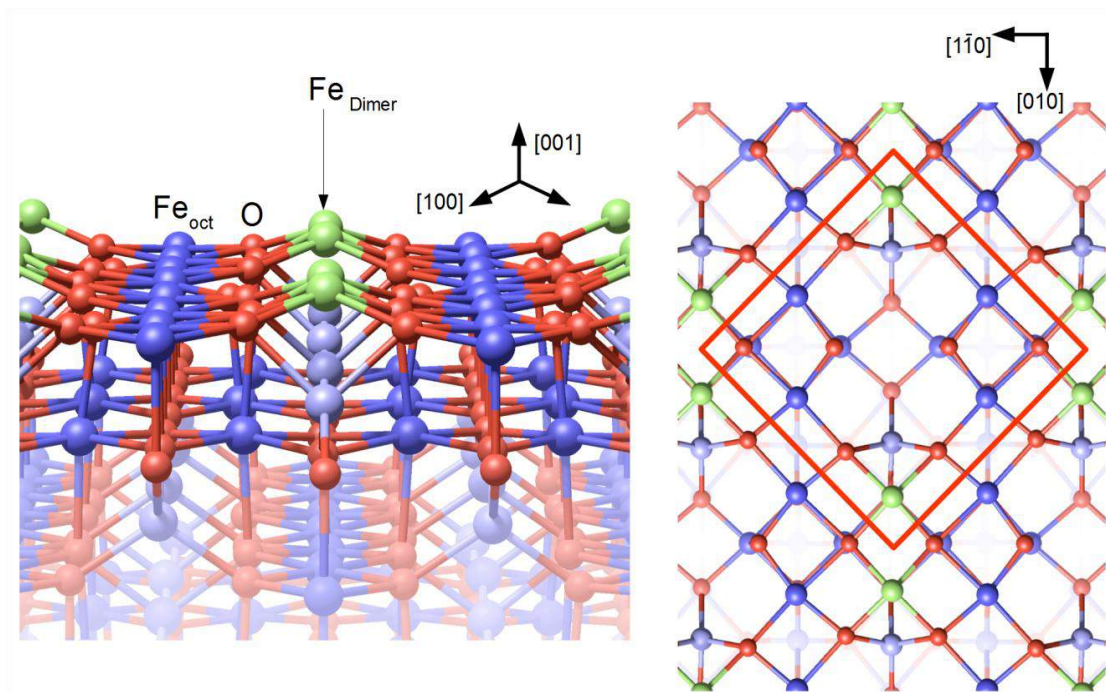
These results allow us to propose a mechanism for the formation of the Fe-Dimer surface by deposition of Fe on the  $\text{Fe}_3\text{O}_4(001)-(\sqrt{2} \times \sqrt{2})R45^\circ$  surface. It is known that some elements such as Ni, Co, Ti, (80) enter the subsurface, filling one  $\text{Fe}_{\text{oct}}$  vacancy in the third layer of the SCV reconstruction, which induces the  $\text{Fe}_{\text{int}}$  to move and occupy the other vacancy. Our observations suggest that the formation of the Fe-Dimer surface requires a similar process as the first step, i.e. deposited Fe atoms should enter the surface, and locally lift the SCV reconstruction as our low coverage STM experiments suggest. This Fe incorporation would explain the two bright protrusions on opposite  $\text{Fe}_{\text{oct}}$  rows observed in STM (see also Figure 3.5 and 3.7).

Once the reconstruction is lifted, a new configuration is obtained (which is most likely the DBT structure as reported previously (71, 78) and described in the previous chapter, Figure 3.2). In this structure there are two vacant tetrahedral site per unit cell. According to STM results, the Fe-dimer configuration is only formed on regions where the reconstruction is lifted. One might expect that extra Fe atoms should occupy these sites within the distorted bulk truncation (Fe adatom on DBT). Nevertheless, adsorption of a second Fe atom in the other tetrahedral site per unit cell on DBT structure appears to be unfavorable by DFT + U calculations (78) and were never observed experimentally. Rather, a high coverage of Fe atoms at room



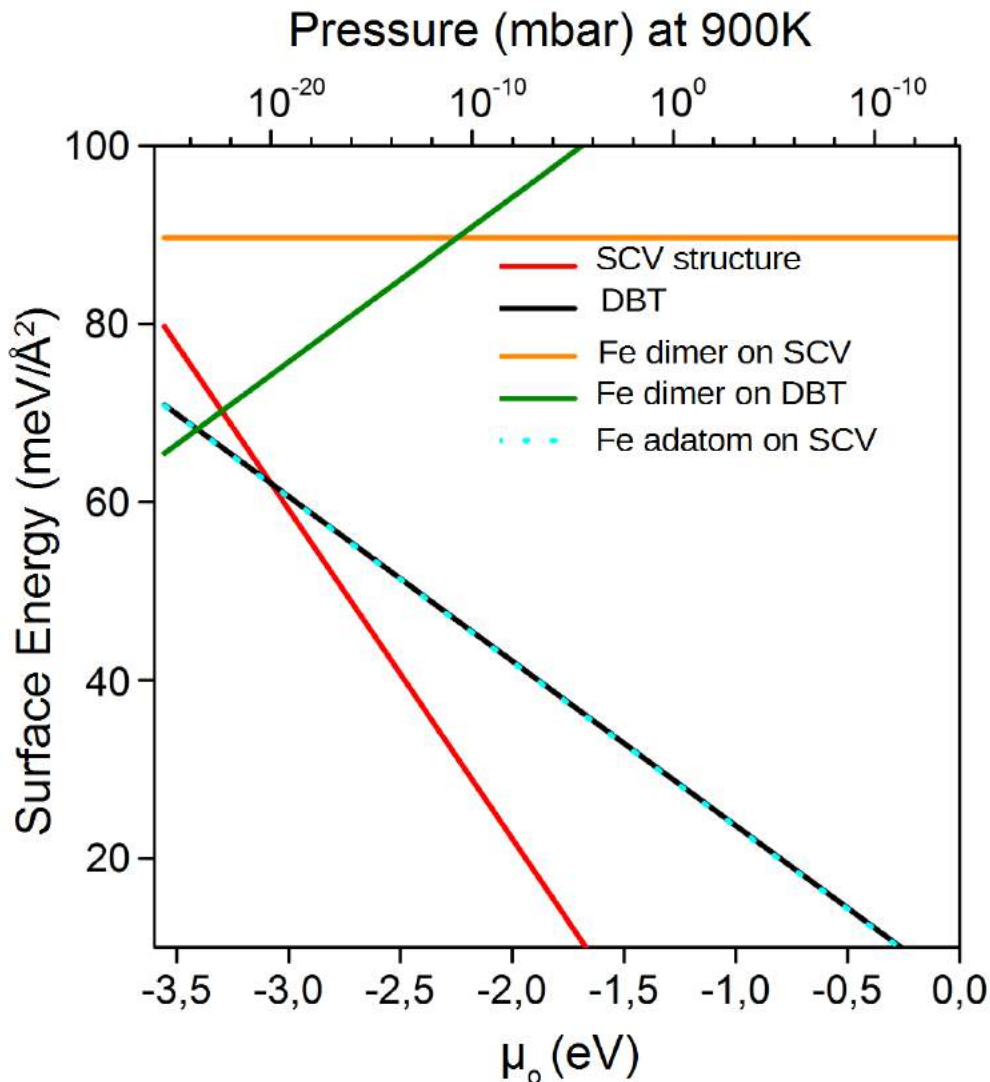
temperature seems to facilitate a conversion from tetrahedral to octahedral Fe coordination, forming the Fe-dimer configuration.

Figure 4.9 shows the perspective and top views of the Fe-dimer on the  $\text{Fe}_3\text{O}_4(001)$  surface. The Fe atoms of the dimer (green atoms) are fourfold coordinated to surface oxygen atoms, filling two of the four octahedral sites per unit cell. The orange square on the top view show the  $(\sqrt{2}\times\sqrt{2})R45^\circ$  periodicity, which is generated by the Fe-dimers.



**Figure 4.9.** Perspective and top views of the Fe-dimer on the  $\text{Fe}_3\text{O}_4(001)$  surface.

The mechanism described for the formation of Fe-dimers on the  $\text{Fe}_3\text{O}_4(001)$  surface appears to be consistent with first principles thermodynamics calculations. Figure 4.10 shows the surface phase diagram for different configurations related with the  $\text{Fe}_3\text{O}_4(001)$  surface.



**Figure 4.10.** Surface energy as a function of oxygen chemical potential,  $\mu_o$ , for different  $\text{Fe}_3\text{O}_4$  (001) surface configurations (Adapted from(88)).

The subsurface cation vacancy (SCV) appear in red and is energetic favored with respect to the distorted bulk truncation (DBT) (black line), which is favored below an oxygen chemical potential of - 3 eV.

The diagram shows a similar surface energy between the DBT structure and the Fe adatom on the SCV (cyan dot line), which is consistent with the observation that both Fe adatoms and incorporated Fe atoms are observed after deposition at low coverage (one additional Fe adatom per unit cell).

To validate our mechanism, two configurations for the Fe-Dimer surface were calculated (88): the dimer on the SCV structure and the dimer on the BDT structure, the diagram shows how the formation of Fe-Dimer on the SCV structure is very unfavourable while the formation of the Fe-Dimer on the BDT structure under reducing conditions occurs.

### 4.7 Conclusions

The Fe-Dimer termination was prepared by evaporating Fe onto the  $\text{Fe}_3\text{O}_4(001)$ - $(\sqrt{2}\times\sqrt{2})R45^\circ$  surface at room temperature. At low coverage, the Fe coexist as Fe adatoms and as Fe atoms incorporated in the subsurface. The Fe-Dimer surface is formed onto the distorted bulk truncation surface suggesting that the  $(\sqrt{2}\times\sqrt{2})R45^\circ$  reconstruction should be lifted before the formation of the dimer. The Fe-Dimer surface is formed at two Fe atoms per unit cell, exhibiting  $(\sqrt{2}\times\sqrt{2})R45^\circ$  symmetry. The Fe-Dimer surface is unstable in oxygen rich conditions, and Fe-oxide clusters are formed. Formation of clusters also were observed when Fe atoms, and patches of Fe-Dimers on Fe rich surfaces reacted with oxygen.



## 5. Surface Defects on Fe<sub>3</sub>O<sub>4</sub>: The Methanol Adsorption Case

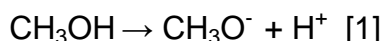
*This chapter is based on a manuscript published in Topics in Catalysis Special Issue 2016, doi:10.1007/s11244-016-0713-9, where most parts of this chapter can also be found. However, this chapter contains more information about TPD analysis, and adsorption on the Fe-Dimer surface, which is not discussed in the published paper.*

### 5.1 Adsorption of Methanol on Metal Oxide Surfaces

Methanol can be involved in several processes to produce hydrogen, as in the case of oxidative reforming, decomposition, steam reforming (89) and has received renewed interest for its importance in fuel-cell technology (90). Its importance is based in its characteristics; methanol has a high H/C ratio (4:1), equal to methane, which is crucial in its application as hydrogen carrier. Unlike methane, methanol is a liquid at atmospheric pressure and environmental temperature. It has a low boiling point, which allows a facile vaporization. Furthermore, its conversion to hydrogen requires lower temperature than other fuels (89).

Moreover, the adsorption of methanol (CH<sub>3</sub>OH) has been used to study and quantify the density of active sites on metal oxide catalysts, and the product distribution observed upon desorption is thought to reflect the nature of the active sites (91). In this sense, Wachs and Badlani have proposed a novel chemisorption method to quantitatively determine the number of surface active sites on metal oxide catalysts, using the dissociative adsorption of methanol as a reference (91).

Such dissociation is typically described as follows :



## Chapter 5. Surface Defects on Fe<sub>3</sub>O<sub>4</sub>: The Methanol Adsorption Case

Here, the authors claim that methanol oxidation product distribution at low conversion reflects the nature and number of the surface active sites, calling the methanol molecule a "smart" chemical probe (91).

Whether CH<sub>3</sub>OH dissociates upon adsorption on a metal-oxide surface depends on the atomic-scale structure, the adsorption temperature, and the degree of coordinative unsaturation of the surface sites, i.e., the number of bonds missing in comparison to the bulk environment (14, 92).

The adsorption of methanol on MgO (100) surface is a good example of this. The dissociative adsorption appears to be dependent of the preparation conditions of the sample and the adsorption temperature. When the samples were exposed to methanol at low temperature (180 K), the sputtered surface shows a higher adsorption of methanol than the surface which was not sputtered. Different results were found when the adsorption of methanol was made at room temperature. Here, the sputtered surface shows high intensity of methoxy species due to the dissociation reaction, while on the not sputtered surface was not observed adsorption (14).

Another important aspect to consider is related to the basicity and acidity present on the oxides. While MgO (001) shows dissociative adsorption of methanol, as was described above, the NiO (100) surface, with a similar structure as the MgO (001) surface, does not present dissociative adsorption of methanol. This suggests a lower basicity on the NiO (001) surface to induce dissociation of weak acids (93).

Several studies have focused on the interaction of methanol with metal oxide surfaces, and show a strong correlation between the atomic-scale structure with the chemical reactivity (5, 14, 27, 91, 92, 94-99). The presence of defects has been shown to have a high importance.

On ZnO (0001) surface the step edges would expected to be the sites for dissociative adsorption of methanol. Step edges which have under-coordinative cations-anions pairs in its structure (100).

## Chapter 5. Surface Defects on Fe<sub>3</sub>O<sub>4</sub>: The Methanol Adsorption Case

Oxygen vacancies ( $V_{\text{O}}$ s) have been shown to be the major active sites on TiO<sub>2</sub> (96, 97) and CeO<sub>2</sub> (27, 98) surfaces, with adsorbed methoxy species ( $\text{CH}_3\text{O}^-$ ) and hydroxyl groups formed at room temperature. Reaction products such as formaldehyde and methane are reported to emerge from this chemistry. Here the use of scanning probe microscopies has been relevant. On the TiO<sub>2</sub> (110) surface, atomic resolution STM images show that methanol adsorbs dissociatively on the oxygen vacancy sites (96). The use of NC-AFM has helped to identify the oxygen vacancies as the dissociative adsorption site for methanol on CeO<sub>2</sub> (111) surface (98).

On the Fe<sub>3</sub>O<sub>4</sub>(111) surface (100) methanol undergoes dissociative adsorption on Fe-terminated regions of the surface, while O-terminated regions do not show any reaction at room temperature. This observation led to the conclusion that the dissociation occurs via a Brønsted acid-base mechanism requiring under-coordinated cation–anion pairs.

Recombination to produce methanol was observed at 330-360 K in TPD, along with a disproportionation reaction between two adsorbed methoxy species to produce methanol and formaldehyde as follows (101)



### 5.2 Adsorption of CH<sub>3</sub>OH on the Clean Fe<sub>3</sub>O<sub>4</sub>(001) Surface

When the clean Fe<sub>3</sub>O<sub>4</sub> (001)-( $\sqrt{2} \times \sqrt{2}$ )R45° surface is exposed to 20 L of CH<sub>3</sub>OH at room temperature new features appear at some of the defects described in chapter 3; compare Figure 3.4 with the one shown on Figure 5.1. The defects do not change their positions, but their apparent height in STM increases significantly. For example, the bright features located on the incorporated Fe defect are now 150 pm high, as compared to the 50 pm previously reported (green square).

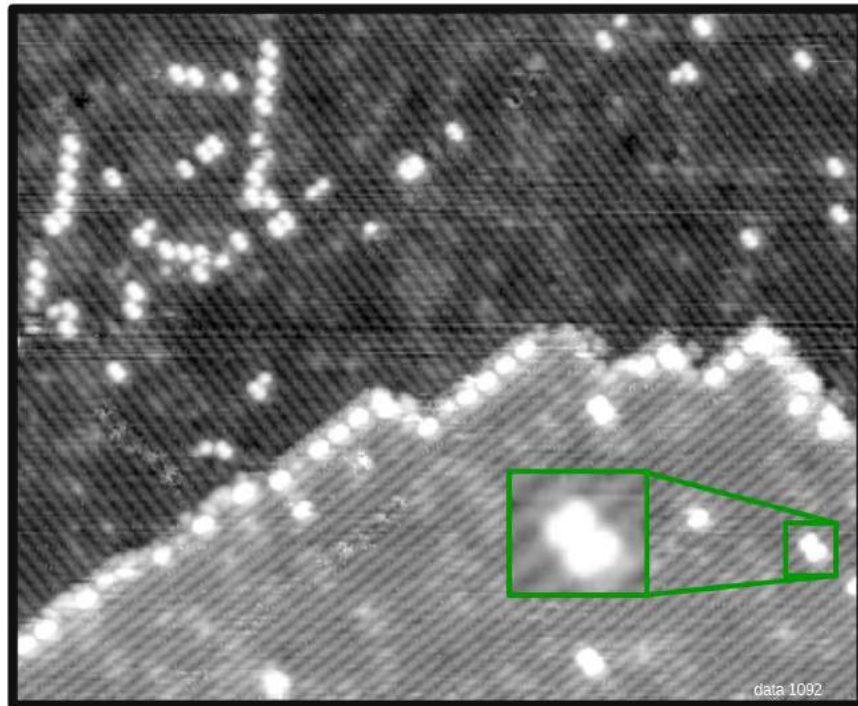


**Figure 5.1.** STM images of the as-prepared Fe<sub>3</sub>O<sub>4</sub> (001)-( $\sqrt{2}\times\sqrt{2}$ )R45° surface (39 × 31 nm<sup>2</sup>; V<sub>sample</sub> = +1.7 V; I<sub>tunnel</sub> = 0.3 nA) after exposure to 20 L CH<sub>3</sub>OH at room temperature.

Interestingly, the methanol-induced, bright features were sometimes observed to disappear as the surface was scanned with the STM tip at room temperature, and the defects assumed their original appearance. However, because methanol was still present in the residual gas following the initial exposure, re-adsorption at defects was also observed (See also Figure 5.4, below).

### 5.3 Fe-rich Fe<sub>3</sub>O<sub>4</sub> (001) Surface

To create an increased coverage of defects, 0.1 monolayer (ML) of Fe was deposited on the Fe<sub>3</sub>O<sub>4</sub> (001) surface at room temperature. As described in the previous chapter, 1 ML Fe is defined as one atom per ( $\sqrt{2}\times\sqrt{2}$ )R45° unit cell, i.e.,  $1.42 \times 10^{14}$  atoms/cm<sup>2</sup>.

After deposition (Figure 5.2) , Fe adatoms and Fe incorporated in the subsurface are observed.



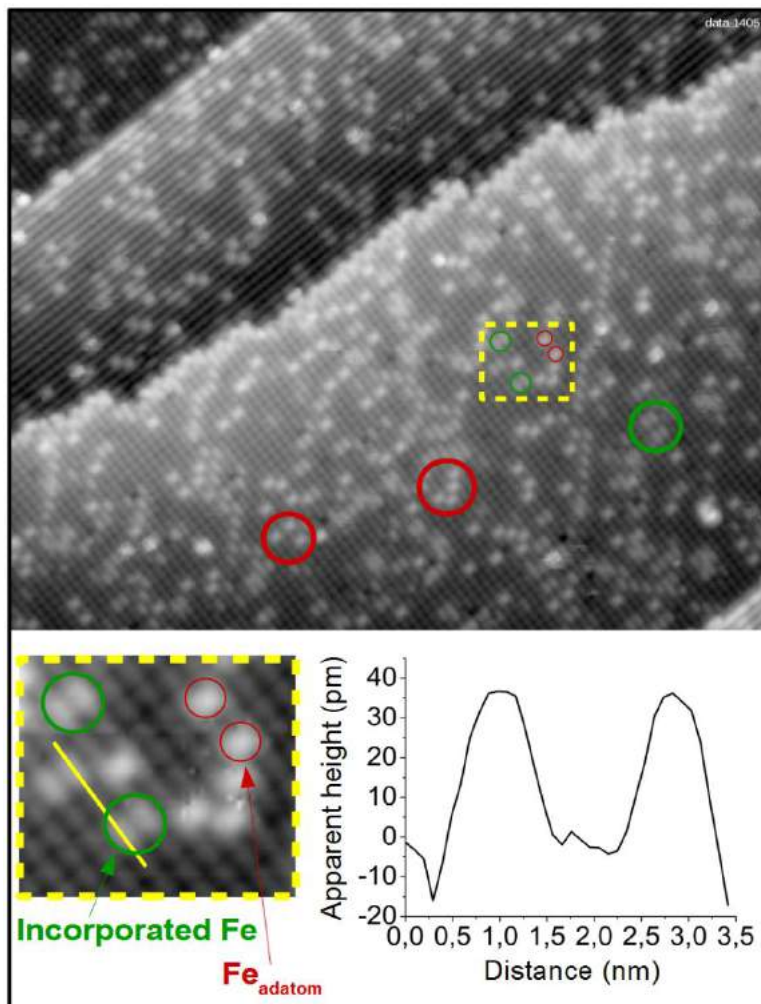


**Figure 5.2.** STM images of as-prepared Fe<sub>3</sub>O<sub>4</sub>(001)-( $\sqrt{2}\times\sqrt{2}$ )R45° surface modified by deposition of 0.1 ML Fe (48 × 45 nm<sup>2</sup>; V<sub>sample</sub> = +1.7 V; I<sub>tunnel</sub> = 0.3 nA). Fe adsorbs as adatoms (red circles) and incorporates in the subsurface, forming bright double features on the Fe<sub>oct</sub> rows (green circles), see inset.

### 5.4 Adsorption of CH<sub>3</sub>OH on the Fe-rich Fe<sub>3</sub>O<sub>4</sub> (001) Surface

Exposing the Fe-rich Fe<sub>3</sub>O<sub>4</sub> (001) surface shown in Figure 5.2 to 20 L CH<sub>3</sub>OH (Figure 5.3) leads to similar features as already shown for the adsorption of CH<sub>3</sub>OH on the clean Fe<sub>3</sub>O<sub>4</sub>(001) surface. Adsorption occurs at the step edges, APDBs, and the incorporated Fe defects.

On the incorporated Fe defects, after methanol adsorption each of the two protrusions shows two maxima (see zoomed areas and line scans in Fig. 5.3), suggesting the adsorption of two methanol related species in close proximity to this defect.

The figure shows two kinds of step edges on the Fe<sub>3</sub>O<sub>4</sub>(001) surface. The yellow arrow in Figure 5.3 highlights a straight step edge, which runs parallel to the iron rows on the upper terrace. The second type, perpendicular to the octahedral iron rows, is more jagged (red arrow) as was described in Chapter 3.

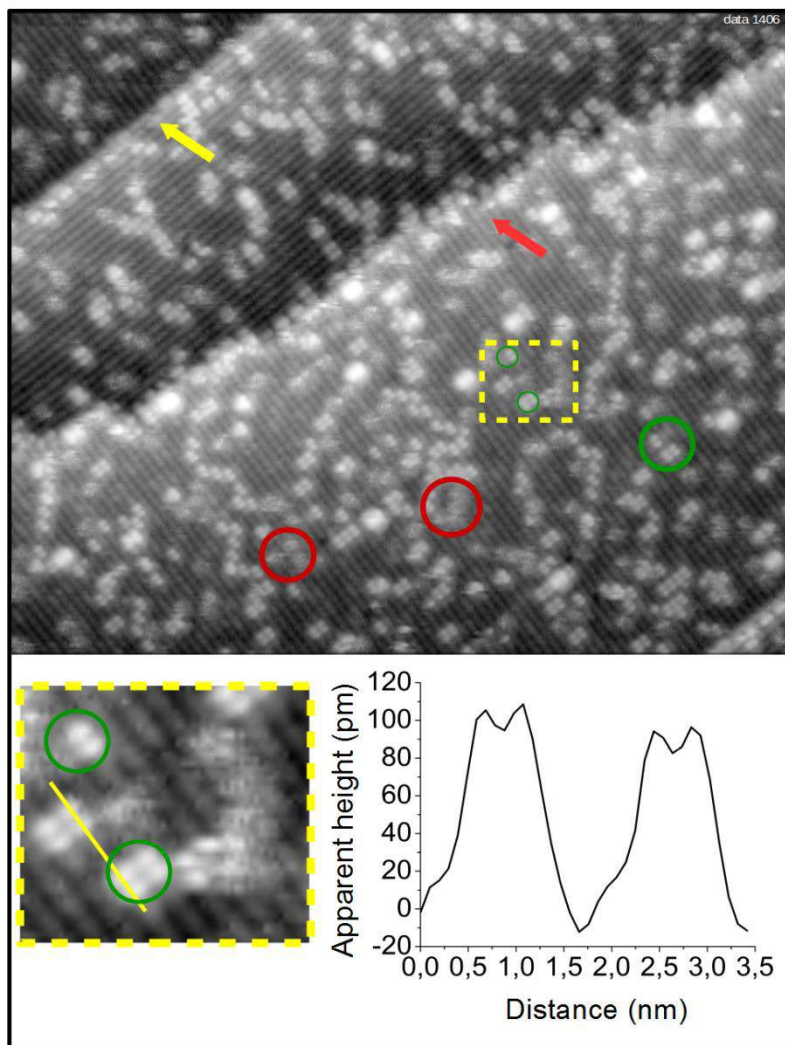


**Figure 5.3.** STM images of as-prepared Fe<sub>3</sub>O<sub>4</sub>(001)-( $\sqrt{2}\times\sqrt{2}$ )R45° surface modified by deposition of 0.1 ML Fe ( $48 \times 45 \text{ nm}^2$ ;  $V_{\text{sample}} = +1.7 \text{ V}$ ;  $I_{\text{tunnel}} = 0.3 \text{ nA}$ ) after exposure to 20 L CH<sub>3</sub>OH at room temperature. Defects have a larger apparent height than those observed on the Figure 5.2 (see line profiles); the fuzzy appearance of the species on top of Fe adatoms indicates weakly adsorbed molecules.

## Chapter 5. Surface Defects on Fe<sub>3</sub>O<sub>4</sub>: The Methanol Adsorption Case

In addition, fuzzy features appear at the position of the Fe adatoms (red circle). Such apparently noisy parts in STM images are typically associated with weakly bound adsorbates that move during the scan.

As in the case of the clean surface, dynamic desorption and readsorption was observed while scanning the surface with the STM at room temperature. The Figure 5.4 shows an STM images sequence acquired, which exemplifies this situation.

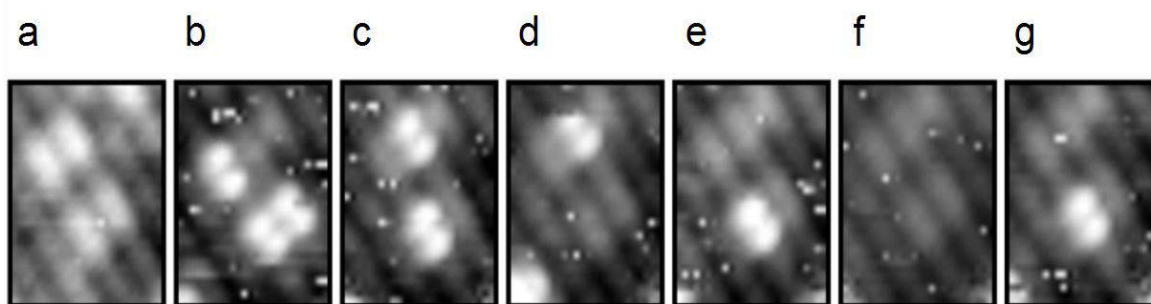


**Figure 5.4.** Dynamic desorption and readsorption of methanol related species on Fe-rich Fe<sub>3</sub>O<sub>4</sub> (001) surface. Consecutive STM images (2.5 × 3.2 nm; V<sub>sample</sub> = +1.6 V; I<sub>tunnel</sub> = 0.3 nA). Panel a shows a couple of incorporated Fe defects before methanol adsorption. Following the adsorption, features related to methanol are observed on the defects. Desorption and readsorption process are observed during STM scanning. Image details: Omega-STM: from data 1405 until data 1411.

### 5.5. Spectroscopic Study of the Adsorption and Reaction of Methanol on Clean and Fe-rich Fe<sub>3</sub>O<sub>4</sub>(001)-( $\sqrt{2}\times\sqrt{2}$ )R45° Surface

To investigate the nature and reactivity of the observed protrusions on STM, the adsorption and reaction of methanol on clean and Fe-rich Fe<sub>3</sub>O<sub>4</sub>(001)-( $\sqrt{2}\times\sqrt{2}$ )R45° surface has been studied with XPS and TPD.

#### 5.5.1 XPS

Figure 5.5 shows O 1s and C 1s photoemission spectra that were recorded after the Fe<sub>3</sub>O<sub>4</sub>(001) surface was exposed to 1.8 L of CH<sub>3</sub>OH at 65 K, and subsequently annealed to progressively higher temperatures.

The O 1s spectra are shown in Figure 5.5a. Adsorption of 1.8 L CH<sub>3</sub>OH at 65 K and annealing to 95 K produces two additional signals in addition to the peak at 530.1 eV that is associated with the lattice oxygen (76, 87). The shoulder on the high-energy side at approximately 531 eV is consistent with both surface OH groups and methoxy species (102), while the peak at 533.1 eV is attributed to molecular CH<sub>3</sub>OH (26). Neither the shape nor position of the lattice oxygen peak is affected by methanol adsorption, only its intensity is reduced.

When the sample is heated to progressively higher temperatures the molecular methanol desorbs first. By 280 K, the intensity of the peak area at 533.1 eV has decreased from 32 % to 4 %. The signal from the lattice oxygen increases again.

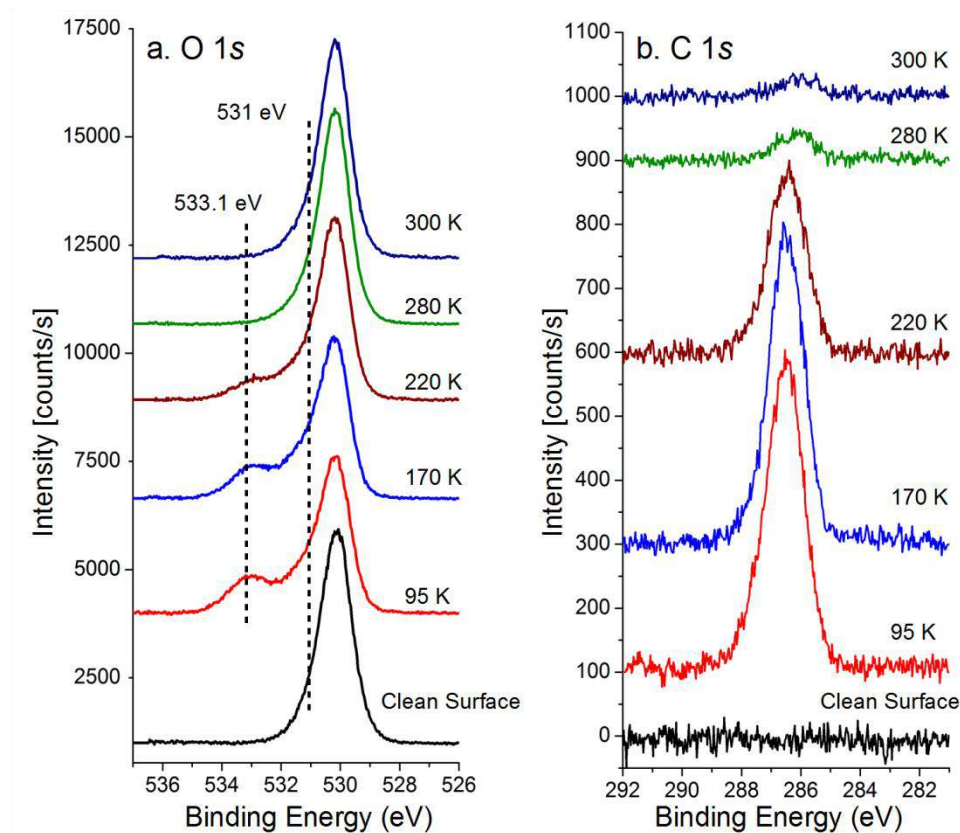


**Figure 5.5.** C 1s and O 1s XPS spectra from methanol adsorbed on the Fe<sub>3</sub>O<sub>4</sub>(001)-( $\sqrt{2} \times \sqrt{2}$ )R45° surface at 65 K and annealed as indicated. The data are offset in the y-direction for clarity.

The C 1s spectra are shown in Figure 5.5b. The C 1s region has no detectable C signal when the surface is freshly prepared. Following the adsorption of methanol at 65 K and annealing to 95 K, a symmetric peak centered at 286.5 eV appears. Upon heating, this peak becomes narrower and decreases in intensity. When the sample is heated to 280 K, its intensity decreases notably and its position shifts to 286 eV. This suggests that molecular methanol desorbs below room temperature, leaving only adsorbed methoxy species at 280 K. Methoxy generally has a lower C 1s binding energy than methanol (e.g. on ZnO (103), TiO<sub>2</sub> (110) (97), TiO<sub>2</sub> (001) (104), MgO (105), and CeO<sub>2</sub> (111) (26)) due to an increase in the electron density around the C atom when the hydroxyl proton is removed (103).

## Chapter 5. Surface Defects on Fe<sub>3</sub>O<sub>4</sub>: The Methanol Adsorption Case

In order to get more details about the effect of the Fe defects on the adsorption of methanol, we performed XPS measurements for a surface on which the defect concentration was enhanced by deposition of 0.3 ML Fe.

Figure 5.6a compares the Fe2*p* spectra obtained before and after the deposition of the Fe (no methanol exposure). The deposition of Fe on the Fe<sub>3</sub>O<sub>4</sub>(001) surface results in an increase in the Fe<sup>2+</sup> component at 708.7 eV in the Fe2*p*<sub>3/2</sub> peak (inset in Fig. 5.6a). Adsorption of 10 L methanol at 280 K has no effect on the Fe2*p* spectrum for the clean or Fe rich surface. In the C 1*s* region (Figure 5.6b) however, a peak appears at 286.1 eV on the clean surface, related to adsorption on defects. Heating to 300 K decreases this peak's intensity, while it remains at the same position. On the Fe deposited surface (blue), a peak appears at 286.3 eV, which is 50 % larger than the one obtained for the clean Fe<sub>3</sub>O<sub>4</sub>(001) surface. Again, heating to 300 K decreases the intensity of the peak, which remains at the same position.

The C 1*s* spectra show a small shift in the binding energies between the 0.3 ML ML Fe-Fe<sub>3</sub>O<sub>4</sub>(001) surface and the clean Fe<sub>3</sub>O<sub>4</sub>(001) surface. This shift may be related to changes in the valence charge on the carbon due to changes in the electronegativity of the vicinity. Such an interpretation was suggested for similar differences between oxidized and reduced cerium oxide thin films (26), where the peak position on the reduced surface is shifted to higher binding energy. Alternatively, there may be a contribution from molecular methanol adsorbed on Fe adatoms. The O 1*s* spectra after adsorption of 10 L methanol at 280 K are shown in Figure 5.6c. On the clean surface a peak at 530.1 eV is observed that is associated with the lattice oxygen (76, 87). The lattice oxygen peak on the Fe deposited surface (blue spectra), shifts to higher binding energy as expected. The shoulder on the high-energy side at approximately 531 eV is higher than the observed on the clean surface (compare inset in Fig. 5.6c). The peak at 533.1 eV (attributed to molecular CH<sub>3</sub>OH), is not observed due presumably to the low concentration to methanol species on the surface.

## Chapter 5. Surface Defects on Fe<sub>3</sub>O<sub>4</sub>: The Methanol Adsorption Case

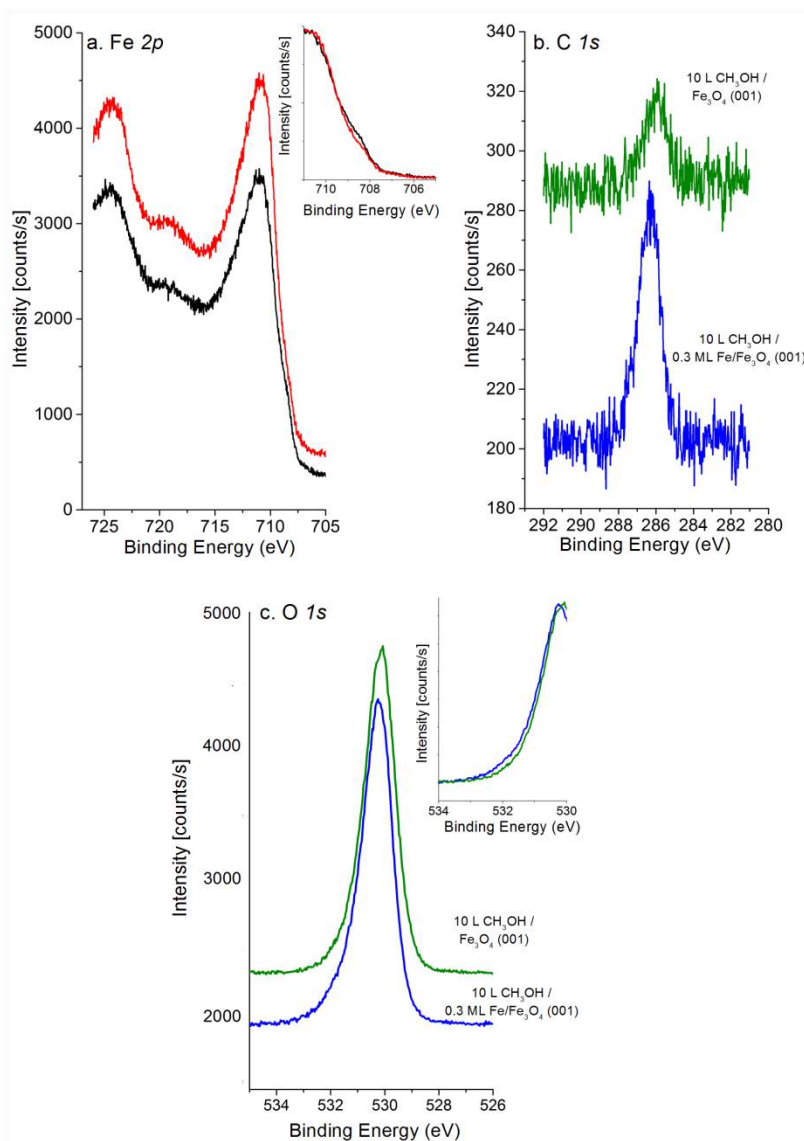


**Figure 5.6.** a. Fe 2p XPS spectra before (red) and after (black) the deposition of 0.3 ML Fe on the clean Fe<sub>3</sub>O<sub>4</sub>(001)-( $\sqrt{2} \times \sqrt{2}$ )R45° surface at room temperature. b. C 1s XPS spectra from methanol adsorbed at 280 K on the Fe<sub>3</sub>O<sub>4</sub>(001)-( $\sqrt{2} \times \sqrt{2}$ )R45° surface (green line) and the 0.3 ML Fe/ Fe<sub>3</sub>O<sub>4</sub>(001)-( $\sqrt{2} \times \sqrt{2}$ )R45° surface (blue line). c. O 1s XPS spectra from methanol adsorbed at 280 K on the Fe<sub>3</sub>O<sub>4</sub>(001)-( $\sqrt{2} \times \sqrt{2}$ )R45° surface (green line) and the 0.3 ML Fe/ Fe<sub>3</sub>O<sub>4</sub>(001)-( $\sqrt{2} \times \sqrt{2}$ )R45° surface (blue line). The data are offset in the y-direction for clarity.



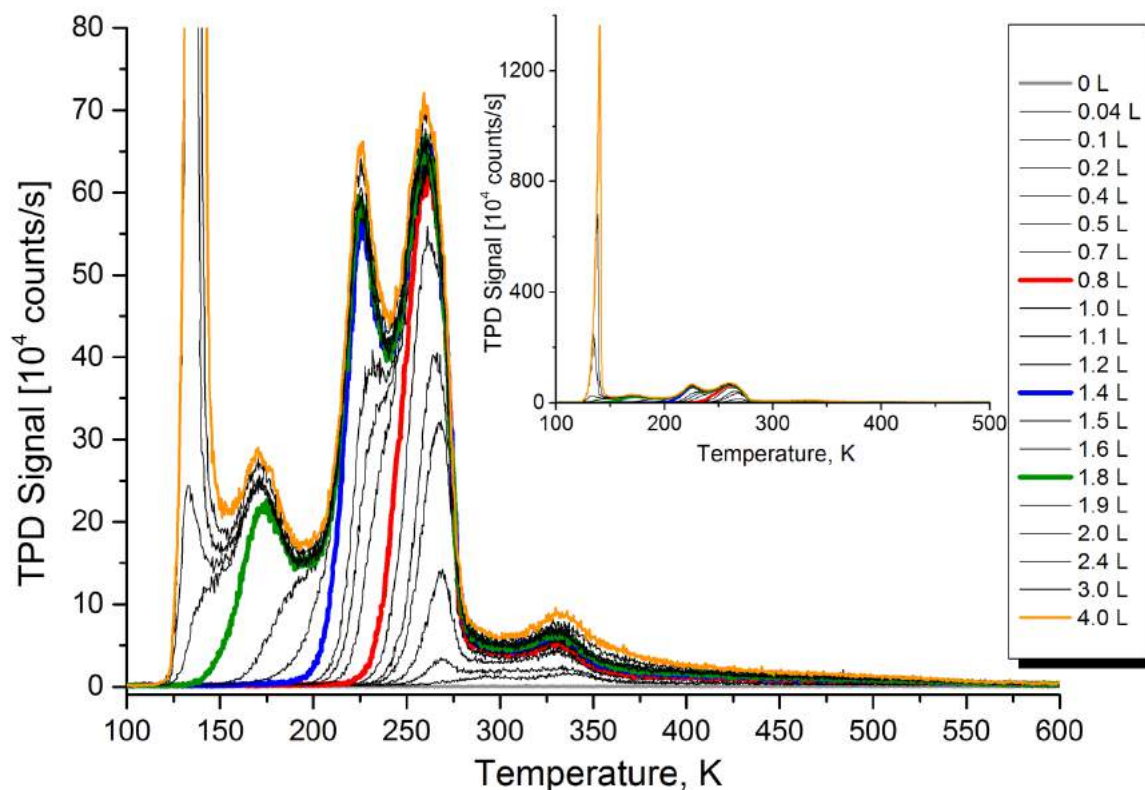
### 5.5.2. Temperature Programmed Desorption Spectroscopy

Figure 5.7 shows a series of TPD spectra for several methanol dosed surfaces. The figure shows the spectra monitored at  $m/z = 31$ , which is the main product of the methanol cracking. Other masses (32, 28, 18, 19) were followed and its spectra showed the same trend that the mass 31, which indicates that these masses were products of mass spectrometer cracking of methanol. The methanol was dosed at temperature of 110K. During the experiment the sample had been flashed to 900 K after each TPD measurement, with no evidence of changes on the surfaces between experiments after flashing.

The lowest temperature desorption peak is measured at 134 K, and appears after doses of 1.9 L of CH<sub>3</sub>OH. Its intensity increases as exposure increases. The peak has been assigned to multilayer desorption according to observations on other metal-oxides surfaces such as, Fe<sub>3</sub>O<sub>4</sub> (111) (101), TiO<sub>2</sub> (110) (19) and ultrathin MgO films on Mo (100) (106).

A small peak is observed at 173 K, similar signals have been observed on TiO<sub>2</sub> (110) and Fe<sub>3</sub>O<sub>4</sub> (111) surfaces and have been attributed to physisorption of methanol molecules on bridging oxygen sites. On the Fe<sub>3</sub>O<sub>4</sub> (111) surface, the adsorption is attributed to O-terminated areas. (19, 101).

Two TPD peaks are observed at 226 and 260 K. The peak at 260 K appears after exposure to approximately 0.1 L of CH<sub>3</sub>OH and saturates at 0.8 L (red curve). After dosing 1.0 L the peak at 226 K starts to grow, and reaches saturation at 1.4 L (blue curve). Both peaks follow a first-order desorption kinetics, where the temperature stays constant with different methanol coverage. Similar observations were observed on the Fe<sub>3</sub>O<sub>4</sub> (111) surface, where these peaks were attributed to two different molecular adsorption states of methanol.



**Figure 5.7.** TPD spectra of methanol on the clean Fe<sub>3</sub>O<sub>4</sub> (001) surface, monitored at  $m/z=31$ , for several dosing values.

As observed in Figure 5.8, the amount of CH<sub>3</sub>OH represented by the integrated area of the TPD curves increases linearly with the dosage. The linear yield implies that the sticking coefficient of methanol on magnetite at 110 K is constant with exposure and is likely unity.

## Chapter 5. Surface Defects on Fe<sub>3</sub>O<sub>4</sub>: The Methanol Adsorption Case

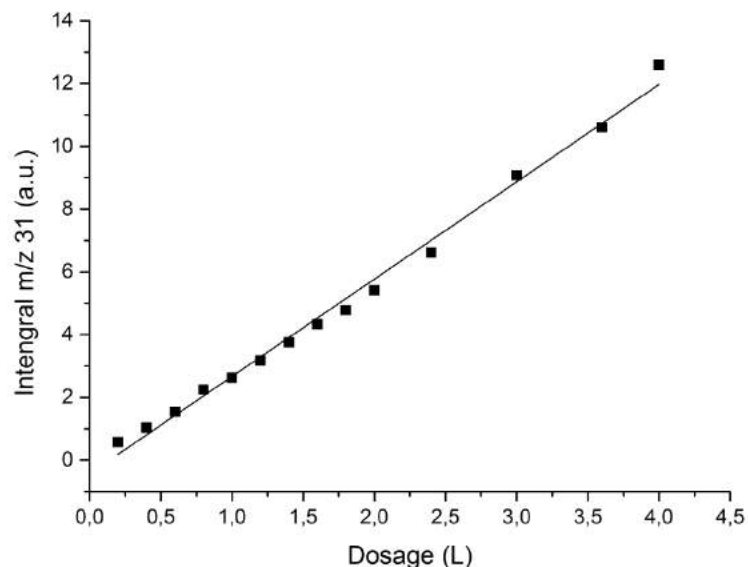


**Figure 5.8.** Total CH<sub>3</sub>OH (m/z=31) TPD peak area vs. methanol exposure at 110 K

Above room temperature additional TPD signals are observed, which has been assigned to adsorption at defects. Temperature programmed desorption was performed following the adsorption of 10 L CH<sub>3</sub>OH at 280 K on the clean Fe<sub>3</sub>O<sub>4</sub>(001) surface (Figure 5.9 a) and on the 0.3 ML Fe-Fe<sub>3</sub>O<sub>4</sub>(001) surface (Figure 5.9 b). Desorption of methanol was monitored by following mass 31 (red dots), which is the most intense cracking fragment of this molecule. By comparing this signal with mass 29 (black dots), possible reaction products can be determined (94). On the clean surface, the TPD spectra exhibit two peaks; a sharp peak at 335 K, and a broad shoulder in the region between 400 and 580 K. While the peak at 335 K has a similar shape and intensity for both masses, indicative of molecular methanol, the signal in the region between 400 and 580 K is higher for mass 29. With the addition of 0.3 ML Fe, the low-temperature peak at 335 K slightly shifts to 320 K, and its intensity increases by 42%. As before, the intensity and line shape is similar for both mass 29 and 31. In the region between 400 and 580 K, the peak for mass 31 has its maximum at 450 K, while the peak for mass 29, which is significantly sharper, has the maximum intensity at 470 K.

## Chapter 5. Surface Defects on Fe<sub>3</sub>O<sub>4</sub>: The Methanol Adsorption Case

The blue curves in the spectra result from subtracting the smoothed signal for mass 31 from the mass 29 spectrum. This procedure removes the contribution of methanol from the mass 29 signal, leaving only that of formaldehyde. A broad peak is observed at 480 K, which is increased in intensity following the deposition of 0.3 ML Fe. This peak is most likely attributable to desorption of formaldehyde, as observed previously on Fe<sub>3</sub>O<sub>4</sub>(111) (101). The mass spectra show no evidence for CH<sub>4</sub> or C<sub>x</sub>H<sub>y</sub>, which would have been related to C–O bond cleavage (107). Evolution of CO and H<sub>2</sub> was also not observed.

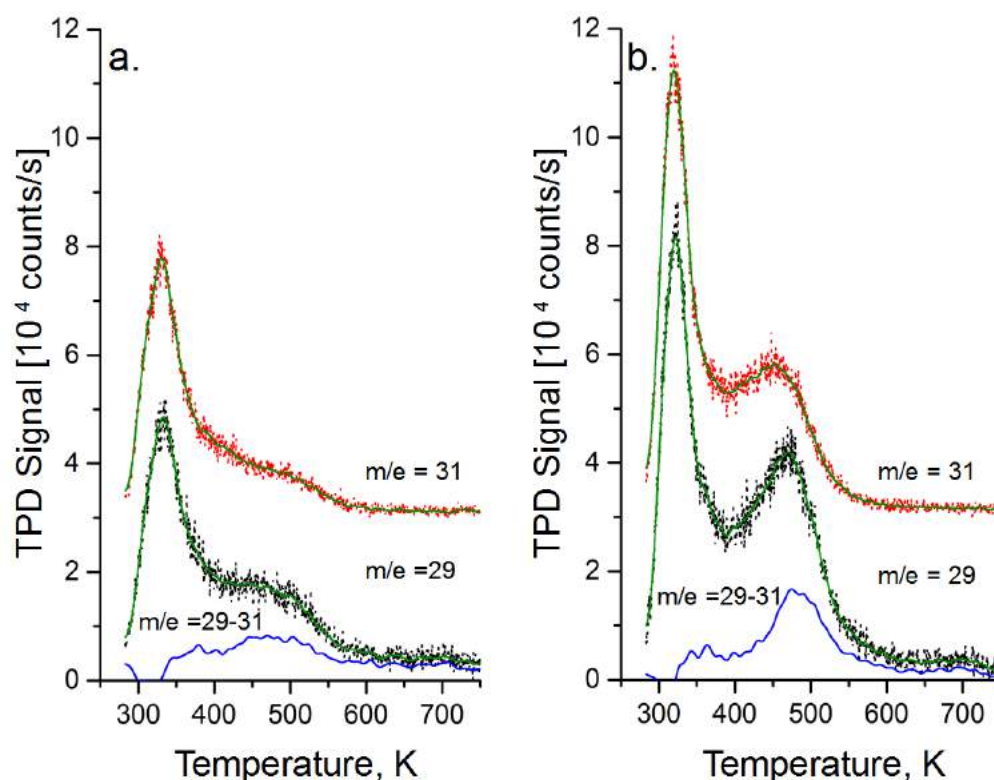


**Figure 5.9.** TPD spectra of 10L of CH<sub>3</sub>OH dosed at 280 K. (a) Fe<sub>3</sub>O<sub>4</sub>(001)-( $\sqrt{2} \times \sqrt{2}$ )R45° surface; (b) 0.3 ML Fe - Fe<sub>3</sub>O<sub>4</sub>(001)-( $\sqrt{2} \times \sqrt{2}$ )R45° surface. The data are offset in the y-direction for clarity. The blue curve, calculated by subtracting the smoothed signal from mass 29 from the smoothed signal of mass 31 represents the desorption of formaldehyde.

### 5.6 Adsorption of CH<sub>3</sub>OH on the Fe-Dimer Surface

As reported in the previous chapter, the Fe-Dimer surface exposes two extra octahedral Fe atoms per reconstructed unit cell. These under-coordinated cations could be active sites for dissociation of molecules. The adsorption of methanol on the Fe-Dimer surface was studied using STM and XPS.

Figure 5.10a shows the Fe-Dimer Fe<sub>3</sub>O<sub>4</sub> (001) surface obtained as reported in the previous chapter. After dosing 20 L of CH<sub>3</sub>OH at room temperature (Figure 5.10b), a high density of bright protusions, located atop of the Dimers appears as a consequence of methanol exposure.

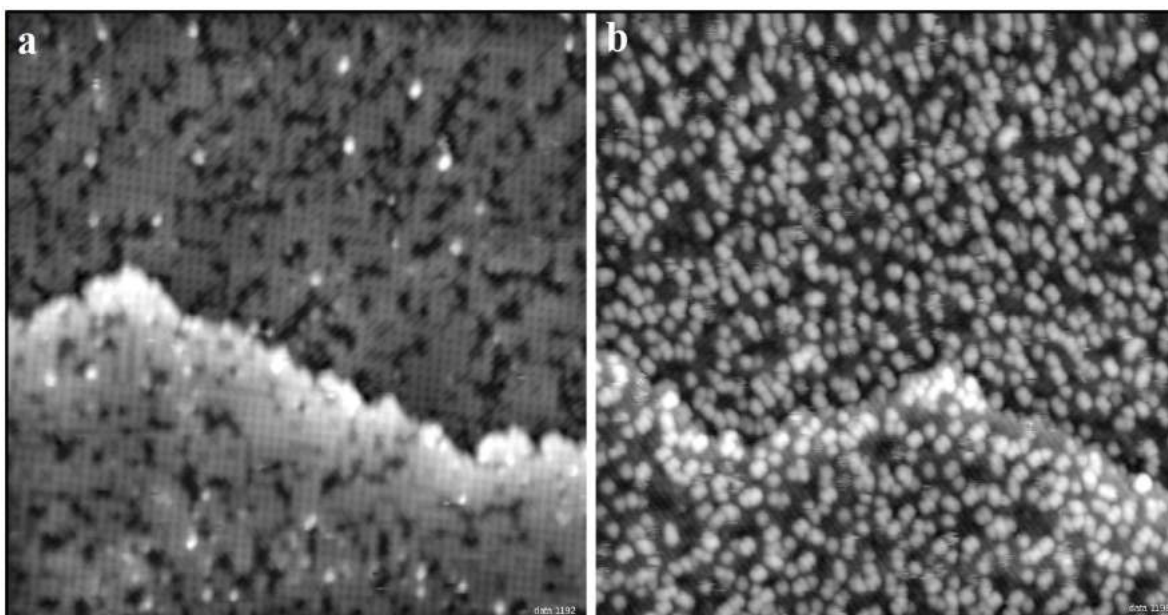


**Figure 5.10.** **a.** STM image of as-prepared Fe-Dimer ( $50 \times 50 \text{ nm}^2$ ;  $V_{\text{sample}} = +1.4 \text{ V}$ ;  $I_{\text{tunnel}} = 0.3 \text{ nA}$ ). Image **b** shows the surface in **a** after dosing 20 L of CH<sub>3</sub>OH at room temperature ( $50 \times 50 \text{ nm}^2$ ;  $V_{\text{sample}} = +1.4 \text{ V}$ ;  $I_{\text{tunnel}} = 0.3 \text{ nA}$ ).

## Chapter 5. Surface Defects on Fe<sub>3</sub>O<sub>4</sub>: The Methanol Adsorption Case

Figure 5.11 shows C 1s, O 1s and Fe 2p photoemission spectra that were recorded after the Fe-Dimer surface was exposed to 10 L of CH<sub>3</sub>OH at room temperature, and subsequently annealed to progressively higher temperatures.

The C 1s spectra are shown in Figure 5.11a. Following the adsorption of methanol a symmetric peak centered at 286.8 eV appears. When the sample is heated to 373 K, its intensity decreases. By 433 K, the intensity decreases notably and its position shifts to 286.1 eV, assigned previously to adsorption of methanol on defects. At 773 K, the C 1s region has no detectable C signal.

The position of the carbon peak at 286.8 eV is higher than the position assigned to methanol and methoxy adsorption on the Fe<sub>3</sub>O<sub>4</sub> (001)-( $\sqrt{2}\times\sqrt{2}$ )R45° surface. Again, the shift may be related to changes in the valence charge on the carbon, where the peak position on the more reduced surface is shifted to higher binding energy (26).

The O 1s spectra are shown in Figure 5.11b. The Fe-Dimer surface exhibits a slightly asymmetric peak at 530.3 eV associated with the lattice oxygen in the Fe-rich surface (78). Adsorption of CH<sub>3</sub>OH produces an additional signal at approximately 531 eV, which is consistent with both, surface OH groups and methoxy species (102).

When the sample is heated to 433 K the signal at 531,3 eV decreases its intensity. The O 1s peak recovers the position for the lattice oxygen in magnetite at 530.1 eV when the sample is annealed at 773 K.

Adsorption of methanol does not involve changes on the Fe 2p spectra for the Fe-Dimer surface (Figure 5.11c). As discussed previously, the Fe-Dimer surface exhibits an enhanced Fe<sup>2+</sup> component (compare inset in Fig. 5.11c, black and red spectra). This feature persists after adsorption of methanol and further annealing until 473 K. By 773 K, the obtained spectra resemble the spectra for the clean Fe<sub>3</sub>O<sub>4</sub> (001)-( $\sqrt{2}\times\sqrt{2}$ )R45° surface due to diffusion of Fe into the bulk (88)

## Chapter 5. Surface Defects on Fe<sub>3</sub>O<sub>4</sub>: The Methanol Adsorption Case

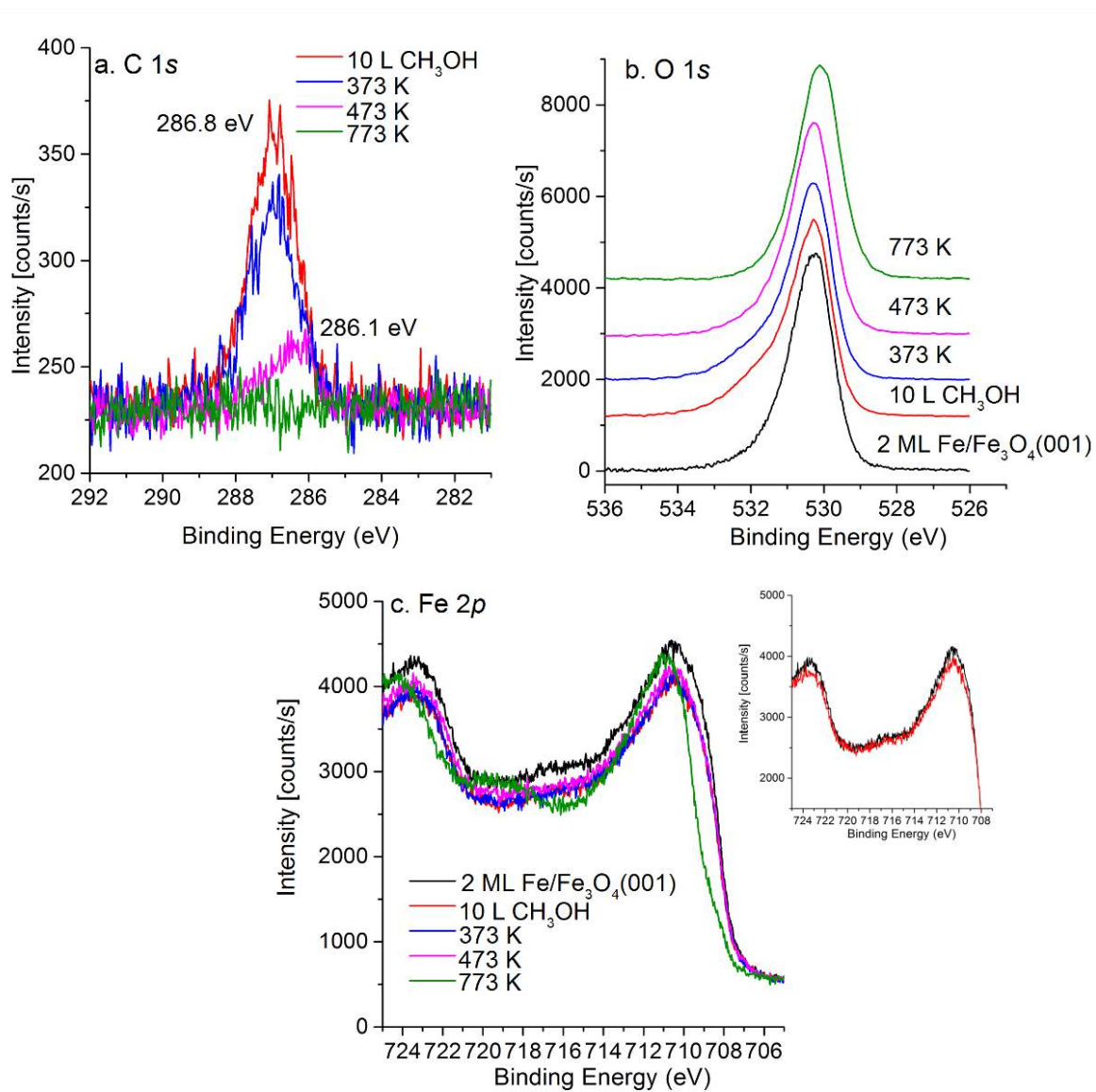


**Figure 5.11.** C 1s, O 1s and Fe 2p XPS spectra from methanol adsorbed on the Fe-Dimer surface at room temperature and annealed as indicated.

### 5.8. Discussion

The results described above show clearly that methanol adsorption on the Fe<sub>3</sub>O<sub>4</sub>(001) surface at room temperature is restricted to defect sites. The active sites for dissociation are identified as step edges, incorporated Fe defects, and APDBs.

The reactivity of step edges on metal oxide surfaces is well documented (5, 108, 109), and is linked to the coordinative unsaturation of the atoms located there.

Iron adatoms are a common defect when the Fe<sub>3</sub>O<sub>4</sub>(001) surface is prepared in reducing conditions (81), when the Fe<sub>3</sub>O<sub>4</sub> bulk is Fe-rich (85, 110), or when Fe is evaporated onto the surface (78). The reactivity of the Fe adatoms is again most likely linked to coordinate unsaturation, because such cations have only two bonds to surface oxygen. The fuzzy appearance of the adsorbed methanol (inset Fig. 3), which indicates mobility underneath the STM tip, could mean that the molecule is adsorbed more weakly as compared to the other defects. This is probably because dissociation of the molecule is precluded by the lack of nearby lattice oxygen that can receive the acid proton. Previous experimental and theoretical studies have found that adsorption of H is energetically unfavorable for an O<sub>surface</sub> with a subsurface Fe<sub>tet</sub> neighbor (111).

Fe atoms incorporated in the surface appears in STM as a pair of bright protrusions on opposite Fe<sub>oct</sub> rows. The density of such defects scales with the amount of deposited Fe. As described in the previous chapter it is proposed that deposited Fe atoms can enter the subsurface and occupy one of the Fe<sub>oct</sub> vacancies present in the third layer. This induces the Fe<sub>int</sub> interstitial to move and occupy the other Fe<sub>oct</sub>, resulting in a structure that locally resembles a bulk-truncated Fe<sub>3</sub>O<sub>4</sub> lattice.

The coordinative unsaturation of the Fe and O atoms are similar for the bulk truncated surface and for the SCV reconstruction. DFT+U calculations predict that both surfaces contain only Fe<sup>3+</sup>-like cations in the surface layer (37). A key



## Chapter 5. Surface Defects on Fe<sub>3</sub>O<sub>4</sub>: The Methanol Adsorption Case

difference affecting reactivity might be the local electronic structure: Density-of-states plots for the bulk truncation exhibit significantly greater density of (empty) states above the Fermi level than the SCV reconstruction due to Fe<sub>oct</sub><sup>2+</sup>-like cations in the third layer (72, 112). The presence of such states can make the region a stronger Lewis acid site, and more receptive to the electrons from the methoxy species.

The APDB appears as an interruption of the vacancy-interstitial pattern in the second and third layers of the SCV reconstruction (Figure 3.5). Due to this, four Fe<sub>oct</sub> cations meet in the third layer at the junction. Locally, such a configuration also resembles again the unreconstructed lattice. Thus the reactivity can be explained in similar terms to the incorporated-Fe point defect.

Analysis of the TPD data for the clean Fe<sub>3</sub>O<sub>4</sub>(001) surface and the Fe-rich Fe<sub>3</sub>O<sub>4</sub>(001) surface shows that, for both surfaces, the signals for masses 29 and 31 match perfectly over the range between 280 and 350 K (Figure 5.9). This is evidence that the peak around 300 K is due to desorption of CH<sub>3</sub>OH only (94). Similar observations have been reported on Fe<sub>3</sub>O<sub>4</sub>(111) (101) and TiO<sub>2</sub>(110) (19), where peaks in the same range of desorption temperatures have been assigned to the recombinative desorption of CH<sub>3</sub>OH. Deposition of Fe results in an increased desorption in this region, which is probably linked to molecular methanol adsorbed at the Fe adatoms.

The presence of Fe-related defects increases the desorption signal in the region between 400 and 580 K. Following the behavior of the spectra for both masses (29 and 31), it is clear that in the high-temperature range, the intensity and the shape of both spectra are different; this observation indicates the presence of another species in addition to methanol. Mass 31 has a contribution from methanol, while mass 29 has contributions from both methanol and formaldehyde (H<sub>2</sub>CO); the latter is often observed as product of methanol reaction. Consequently, we assign the signal at high temperature as due to partial oxidation of methanol to formaldehyde.

## Chapter 5. Surface Defects on Fe<sub>3</sub>O<sub>4</sub>: The Methanol Adsorption Case

Partial oxidation has been identified on other oxide surfaces as one of the main possible reactions. Interestingly, when the Fe<sub>3</sub>O<sub>4</sub>(001) surface was modified to have additional Fe adatoms and incorporated Fe defects, a similar increase was observed in the peak at 320 K and the high-temperature products linked to the disproportionation reaction. Given the relative abundance of Fe adatoms and incorporated Fe defects (approx. 50:50 at 0.3 ML coverage), and the probability that the Fe adatoms cannot dissociate CH<sub>3</sub>OH and thus contributes to the lower temperature peak, it seems likely that the increase in formaldehyde production is due to the subsurface Fe defects. This can be because this defect promotes the disproportionation reaction by adsorbing two methoxy species in close proximity as STM data suggest (Figure 5.3); yielding formaldehyde and methanol as was observed on TPD data.

On the Fe<sub>3</sub>O<sub>4</sub> (111) surface, complexes with iron ions with a CH<sub>3</sub>O-Fe-CH<sub>3</sub>OH configuration have been proposed, where the strong interaction of the organic species with the iron atom prevents steric repulsions between the methanol related species (101). It could be expected that here, where the adsorption of species occurs in neighboring atoms rather than the same Fe atom, the steric repulsion interaction between the species should be lower.

The temperature for the disproportionation reaction appears to depend on various factors such as the oxidation state of the metal oxide. In the case of vanadium oxide supported on CeO<sub>2</sub>, formaldehyde desorption curves have shown signals in temperature ranges from 500 to 610 K, depending on the oxidation state of vanadium (113). At the CeO<sub>2</sub> (111) surface, methanol was oxidized to formaldehyde and water at 680 K after that methanol dissociation had occurred at oxygen vacancies (98). On the other hand, complete dehydrogenation of methanol to CO and H<sub>2</sub> has been reported on highly reduced ceria surfaces (27).

Oxygen vacancies have shown to be active site for dissociative adsorption of methanol. At the surface, the vacancies affect its electronic structure which would explain its high reactivity. The Fe<sub>3</sub>O<sub>4</sub> (001) surface does not present oxygen

## Chapter 5. Surface Defects on Fe<sub>3</sub>O<sub>4</sub>: The Methanol Adsorption Case

vacancies. Here, the reactivity of the surface with methanol has been explained due the presence of defects which changes the electronic structure of the surface via changes on the oxidation states and distribution of the cations among octahedral and tetrahedral interstitial sites.

Given the available evidence it appears that the adsorption of multiple methoxy species in close proximity at the incorporated Fe defect may promote the disproportionation reaction.

### 5.9 Conclusions

The adsorption of methanol on the Fe<sub>3</sub>O<sub>4</sub> (001) surface was studied. Methanol adsorbs dissociatively on Fe<sub>3</sub>O<sub>4</sub> (001) at 280 K at defect sites that were identified as step edges, antiphase domain boundaries (APDB), iron adatoms and incorporated-Fe defects.

The adsorption at the steps and Fe adatoms can be explained in terms of coordinative unsaturation. In contrast the reactivity at the APDBs and incorporated Fe defects is linked to the local electronic structure; specifically to the presence of Fe<sup>2+</sup> cations in the surface layers.

The adsorption of multiple methoxy species at the latter two defects promotes a disproportionation reaction to form methanol and formaldehyde.

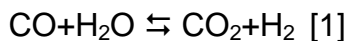


## 6. Adsorption of Formic Acid on the Fe<sub>3</sub>O<sub>4</sub> (001) Surface

*This chapter is based on a manuscript published in The Journal of Physical Chemistry C 119, 2015, 20459. However, this chapter contains additional data and analysis that cannot be found in the published manuscript.*

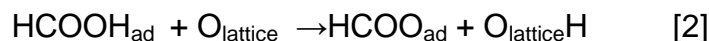
### 6.1 Adsorption of Formic Acid on Metal Oxide Surfaces

Formic acid (HCOOH), the simplest carboxylic acid, has often been used as a model system to investigate the reactivity of metal-oxide surfaces. This is due to its simple molecular structure, and because it is a common intermediate product in the decomposition of harmful organic compounds. Furthermore, the study of the adsorption and reaction of this carboxylic acid is relevant for catalysis, because formate (HCOO<sup>-</sup>) has been proposed as a reaction intermediate in the water-gas shift reaction, (45, 114, 115).



Several experimental and theoretical studies have been undertaken to understand the chemistry behind the adsorption and reaction of formic acid on metal oxides. It is known that adsorption can be molecular, particularly at low temperature, but is often dissociative on surfaces that expose under-coordinated cation/anion pairs (e.g. rutile-TiO<sub>2</sub>(110)(28, 116), MgO(100) (117), NiO(111) (118) CeO<sub>2</sub> (119), anatase-TiO<sub>2</sub> (101) (120) , ZnO (121) ,and SnO<sub>2</sub>(110) (122)).

Such dissociation is typically described in terms of an acid-base reaction; the acidic proton of the HCOOH is abstracted by a basic O<sup>2-</sup> anion, forming an O<sub>lattice</sub>H species, while the remainder of the molecule, a formate (HCOO<sup>-</sup>) species, is bound to acidic metal cation sites (5):



## Chapter 6. Adsorption of Formic Acid on the Fe<sub>3</sub>O<sub>4</sub> (001) Surface

Whether HCOOH dissociates upon adsorption on a metal-oxide surface depends on the atomic-scale structure, the adsorption temperature (123), and whether the cation/anion pair are close enough together to facilitate the H transfer. The degree of coordinative unsaturation (CUS) of the surface sites, i.e. the number of bonds missing in comparison to the bulk environment, affects the strength of the interaction (5, 124).

Three configurations have been considered to explain the bonding of formate on metal oxides surfaces. Figure 6.1 shows schematic models for these configurations: monodentate (Figure. 6.1a), bidentate bridging (Figure. 6.1b) and chelating configuration (Figure. 6.1c) (119, 125, 126). In all cases bonds are formed between the oxygen atoms of the molecule and surface cations.

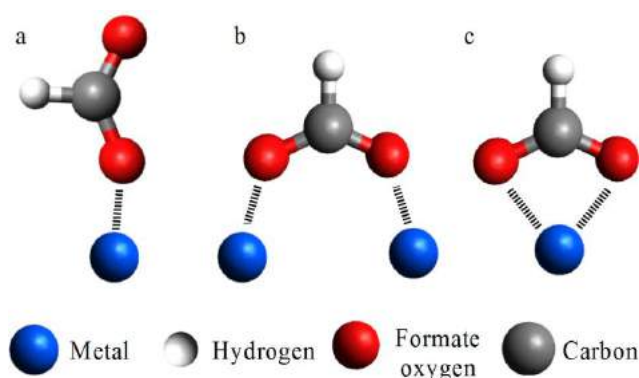


**Figure 6.1** Adsorption geometries for formate on metal oxide surfaces: (a) monodentate configuration, (b) bidentate bridging configuration, and (c) non-bridging bidentate or chelating configuration.

As an example, we briefly consider the prototypical metal oxide surface rutile TiO<sub>2</sub>(110). It is known that the distance between the oxygen atoms of the free formate group is 2.25 Å (127), and the distance between Ti atoms parallel to the [001] direction on rutile TiO<sub>2</sub>(110) surface is 2.968 Å, sufficiently close that formate can adsorb in a bridging bidentate configuration (128). Systems where the distance between metal atoms on surface are larger present a chelating or monodentate configuration, as is the case of ZnO(0001) (129), where the distance

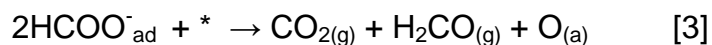
## Chapter 6. Adsorption of Formic Acid on the Fe<sub>3</sub>O<sub>4</sub> (001) Surface

between Zn cations is 3.25 Å. On the Fe<sub>3</sub>O<sub>4</sub>(001) surface the distance between Fe atoms in the surface Fe rows is around 3 Å, here a similar behaviour as the observed on TiO<sub>2</sub> (110) surface would be expected.

After adsorption, formate species can suffer decomposition reactions. Both dehydration, to produce H<sub>2</sub>O and CO, and dehydrogenation to produce H<sub>2</sub> and CO<sub>2</sub> (5), are known to occur. In general, dehydration has been associated with acidic oxides while the dehydrogenation occurs on basic oxides (5). The concept of acidic or basic oxides appears to be related to the metal-oxygen bond strength of the oxide. Here, acidic oxides will present a stronger metal-oxygen bonding than the basic oxides, where the metal-oxygen bonds will be weak (130). According to their selectivity to dehydration or to dehydrogenation reactions, the oxides most widely studied have been classified according to this concept. MgO and ZnO are mainly active in dehydrogenation reactions. Oxides such as Al<sub>2</sub>O<sub>3</sub> and SiO<sub>2</sub> have been associated with dehydration reactions. The oxides of the transition metals have shown reactivity for both reactions. Nevertheless, factors such as the temperature and preparation conditions can change these reactivities (131-133).

When just one channel is present, either dehydration or dehydrogenation, the reaction has been postulated to follow a monomolecular decomposition. On surfaces where both channels are present, the reaction may proceed via a bimolecular mechanism, where two formate species react, or where reactions between formic acid and formate species take place (134).

For bimolecular mechanisms the presence of other decomposition products has been postulated. Decomposition of formic acid on the TiO<sub>2</sub>(110) surface showed evolution of formaldehyde and carbon dioxide as product of decomposition. Here the process was explained by the equation:



Where \* represents the active site necessary for the disproportionation reaction to occur. In the case of the TiO<sub>2</sub>(110) surface this active site was associated with

## Chapter 6. Adsorption of Formic Acid on the Fe<sub>3</sub>O<sub>4</sub> (001) Surface

oxygen vacancies (28), and on the TiO<sub>2</sub>(001) surface with Ti cations of 4-fold oxygen coordination (135).

### 6.2 Adsorption of Formic Acid on Iron Oxide Surfaces

On the Fe<sub>3</sub>O<sub>4</sub>(111) the adsorption of HCOOH varies with the surface termination. On the 1/4 ML Fe<sub>tet</sub> terminated surface, dissociation of HCOOH occurs, and since the distance between under-coordinated Fe<sub>tet</sub> atoms is 5.92 Å, formate groups take a chelating configuration. Molecular adsorption occurs on the oxygen terminated surface (125). The terminations often coexist, and the structure of each remains somewhat controversial (88); therefore it is difficult to draw further conclusions.

The (001) surface, in contrast, undergoes a  $(\sqrt{2}\times\sqrt{2})R45^\circ$  reconstruction that dominates over a wide range of chemical potentials as was described in Chapter 3. The reconstruction is linked to a rearrangement of the cations in the subsurface, but the surface layer is essentially bulk-like save for a subtle distortion of the lattice and the fact that all surface cations are Fe<sup>3+</sup> (37).



### 6.3 Adsorption of Formic Acid on the Clean Fe<sub>3</sub>O<sub>4</sub>(001) Surface

#### 6.3.1 XPS

To investigate the nature of the species obtained after adsorption of HCOOH on the Fe<sub>3</sub>O<sub>4</sub>(001) surface, XPS measurements were conducted at room temperature and low temperature (70 K) in the Mrs. system (Section 2.6.2).

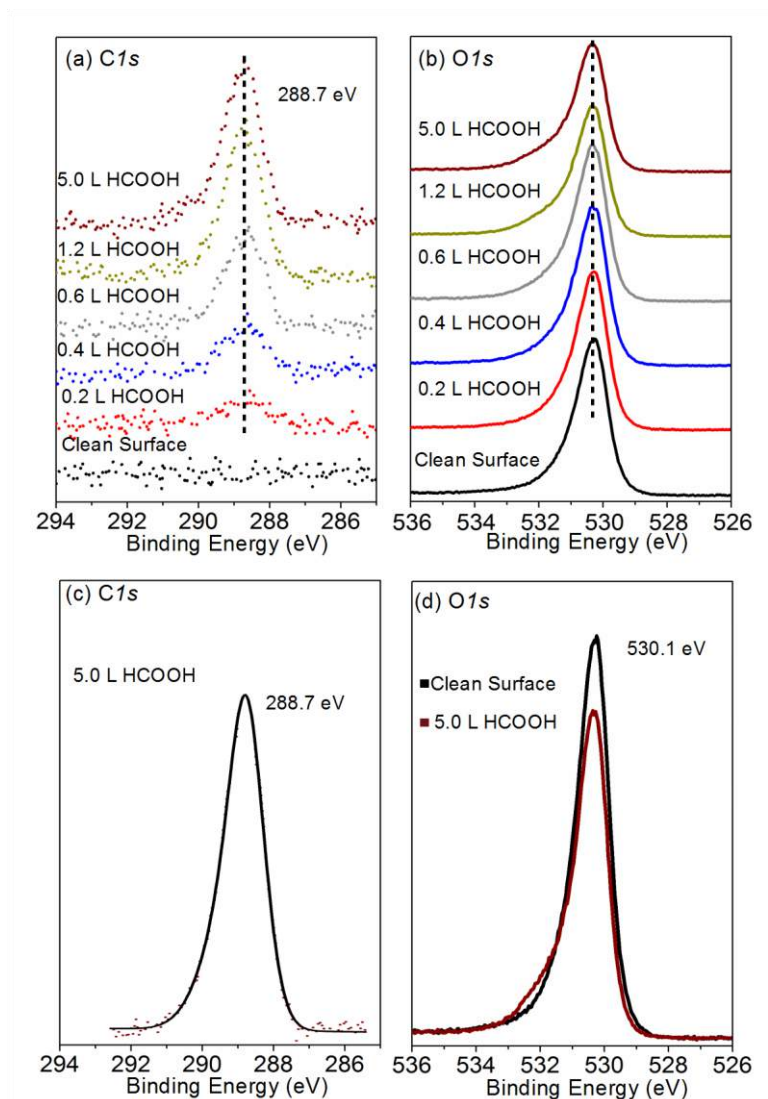
##### 6.3.1.1 XPS at Room Temperature

Figure 6.2 shows O 1s and C 1s photoemission spectra that were recorded after the clean Fe<sub>3</sub>O<sub>4</sub>(001) surface was exposed to HCOOH at room temperature. When the surface is freshly prepared, the C 1s region has no detectable carbon signal (black spectrum) but a peak emerges at 288.7 eV as the exposure of formic acid is increased (Figure 6.2a). At room temperature, the saturation coverage is obtained following a nominal exposure of 1.2 L, and the line shape is well approximated by one peak at 288.7 eV (Figure. 6.2c). The peak at 288.7 eV is consistent with adsorbed formate, which typically appears below 289 eV on other metal-oxide surfaces (117, 134, 136).

As HCOOH is deposited the lattice oxygen peak at 530.1 eV (75) decreases in intensity and a shoulder emerges on the high-energy side (at approximately 532.2 eV), which is saturated by 1.2 L (Figure 6.2b).

The position of this peak is consistent with both, OH groups and formate species on other metal-oxide surfaces (134, 136, 137). Figure 6.2d shows a direct comparison of the clean surface and 5 Langmuir HCOOH O 1s data.

## Chapter 6. Adsorption of Formic Acid on the Fe<sub>3</sub>O<sub>4</sub> (001) Surface



**Figure 6.2.** C 1s and O 1s XPS spectra from formic acid adsorbed on Fe<sub>3</sub>O<sub>4</sub>(001)-( $\sqrt{2}\times\sqrt{2}$ )R45° at room temperature. The upper panels show the evolution of the XPS spectra as a function of HCOOH exposure. The bottom panels show the best fit of the C 1s data for 5 L exposure. For the O 1s data, a direct comparison of the clean and 5 L data is shown.

### 6.3.1.2 XPS at 70 K

When the XPS experiment is performed with the sample at 70 K, at low exposure ( $\leq 0.4$  L) the C 1s data closely resemble those acquired at room temperature exhibiting a single peak at 288.7 eV (Figure 6.3a). As the exposure is increased however, the peak broadens and shifts toward higher binding energy. At 1.2 L the spectrum can be fitted by two components at 288.7 eV and 289.7 eV (Figure 6.3c). When the exposure is increased further, the peak at 289.7 eV grows without saturation, consistent with condensation of HCOOH multilayers onto the sample.

Figure 6.3b shows O 1s photoemission spectra. A shoulder again emerges on the high binding-energy side, but its intensity continues to grow with increasing exposure, as expected for HCOOH multilayers. A direct comparison of the data with the Fe<sub>3</sub>O<sub>4</sub>(001) surface before and after exposure to 5 L HCOOH (Figure 6.3d) shows the peak related to the substrate is more greatly diminished by the HCOOH multilayers than it was by the formate monolayer in Figure 6.2d.

## Chapter 6. Adsorption of Formic Acid on the Fe<sub>3</sub>O<sub>4</sub> (001) Surface

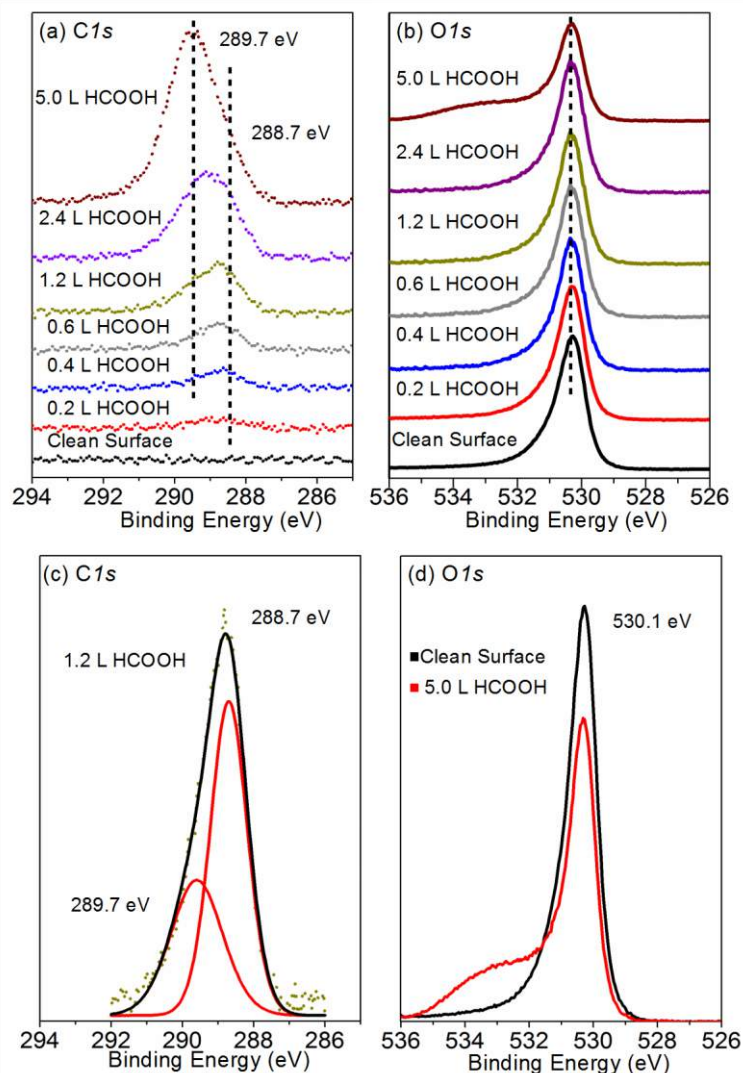


**Figure 6.3** C 1s and O 1s XPS spectra from formic acid adsorbed on the Fe<sub>3</sub>O<sub>4</sub>(001)-( $\sqrt{2}\times\sqrt{2}$ )R45° surface at 70 K. The upper panels show the evolution of the XPS spectra as a function of HCOOH exposure. The bottom panels show the best fit of the C 1s data, for 1.2 L exposure at 70 K. For the O 1s data, a direct comparison of the clean and 5 L data is shown.

### 6.3.2 Infrared Reflection Absorption Spectroscopy

Previous studies have shown the advantages of Infrared Reflection Absorption Spectroscopy (IRRAS) to investigate the configuration of adsorbates on metal oxides surfaces (138). For example, bands observed in the IRRAS-spectra for formate species on anatase TiO<sub>2</sub>(101) surface helped distinguishing the presence of formate species in a monodentate and bidentate configuration (120).

Figure 6.4 shows IRRAS-spectra at (a) room temperature and (b) 190 K acquired for the clean Fe<sub>3</sub>O<sub>4</sub>(001)-( $\sqrt{2}\times\sqrt{2}$ )R45° surface and following exposure to 2 L and 10 L HCOOH. As was mentioned above, these spectra were taken by our collaborators Dr. Heshmat Noei and Prof. Andreas Stierle at DESY. After dosing 2 L at room temperature (Figure 6.4a), a resonance at 1370 cm<sup>-1</sup> appears and reaches saturation around a dose of 10 L. In addition, a resonance with similar, but inverted shape appears at  $\approx$ 1540 cm<sup>-1</sup>. These peak frequencies are characteristic for the symmetric (1370 cm<sup>-1</sup>) and asymmetric (1540 cm<sup>-1</sup>) OCO stretch of formate species (139-141).

The resonance signals show Fano line shapes. Magnetite is neither a perfect conductor as the metals nor a perfect dielectric as the case of some oxide single crystals studied using IRRAS (138, 142). It has been noted that the shape of the peaks on IRRAS-spectra are related with the conducting characteristics of the materials, asymmetric peaks or Fano line shapes can occur due to poorly conducting substrates (143-145). Further description of this topic can be found in ref 145.

Two additional features appear, a double positive peak for the 1370 cm<sup>-1</sup> resonance, with the absorption maxima very close to the steep slope  $\approx$ 1372 cm<sup>-1</sup> and  $\approx$ 1385 cm<sup>-1</sup>. This indicates the superposition of two resonances near 1370 cm<sup>-1</sup>. We attribute the weaker signal to the C-H bending mode  $\delta$ (CH). As it is superimposed on the strong symmetric OCO stretch signal, the position and shape of the weaker peak cannot be determined with any certainty. No bands are

## Chapter 6. Adsorption of Formic Acid on the Fe<sub>3</sub>O<sub>4</sub> (001) Surface

observed in the region around 1700 cm<sup>-1</sup>, which would be expected for the  $\nu$  (C=O) stretch of intact HCOOH molecules (139-141).

The IRRAS-spectra at room temperature confirm the assignment to formate based on the XPS spectra, and show an upright (bidentate) orientation of the molecule. Due to the parallel, small dynamic dipole moment for the OH, the stretch mode expected was not detected (120).

Figure 6.4b shows IRRAS-spectra recorded at 190 K after exposure to HCOOH at the same temperature. The spectra show the symmetric and asymmetric OCO stretch signals at almost the same wavelengths (1365 and 1550 cm<sup>-1</sup>). In addition, a broad peak appears at  $\approx$ 1710 cm<sup>-1</sup>, which can be assigned to the stretching vibration mode of  $\nu$ (C=O) in molecularly adsorbed HCOOH (139-141).

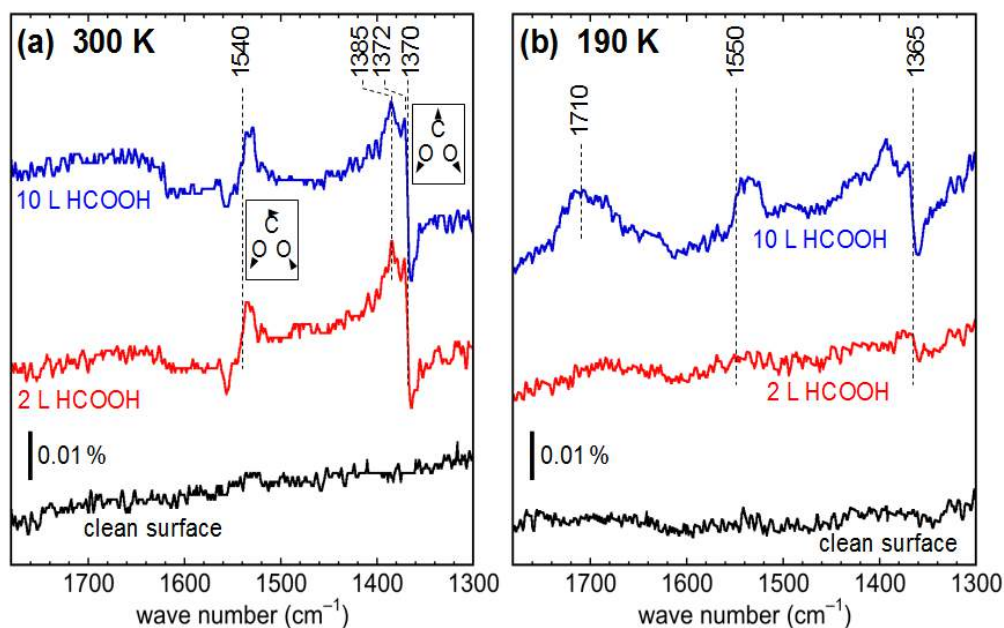


**Figure 6.4.** IRRAS experimental spectra at (a) room temperature and (b) 190 K acquired for the clean Fe<sub>3</sub>O<sub>4</sub>(001)-( $\sqrt{2}\times\sqrt{2}$ )R45° surface and following exposure to 2 L and 10 L HCOOH. The asymmetric (1540 cm<sup>-1</sup>) and symmetric (1370 cm<sup>-1</sup>) vibration modes are sketched in small boxes.

### 6.3.3 Low Energy Electron Diffraction

As described in Chapter 3, the clean Fe<sub>3</sub>O<sub>4</sub>(001) surface exhibits a  $(\sqrt{2}\times\sqrt{2})R45^\circ$  reconstruction, which is observed in LEED (Figure 6.5a) (37). When the surface is exposed to 5 L HCOOH at room temperature the spots related to the  $(\sqrt{2}\times\sqrt{2})R45^\circ$  reconstruction disappear and the surface exhibits a  $(1\times 1)$  periodicity (Figure 6.5b).

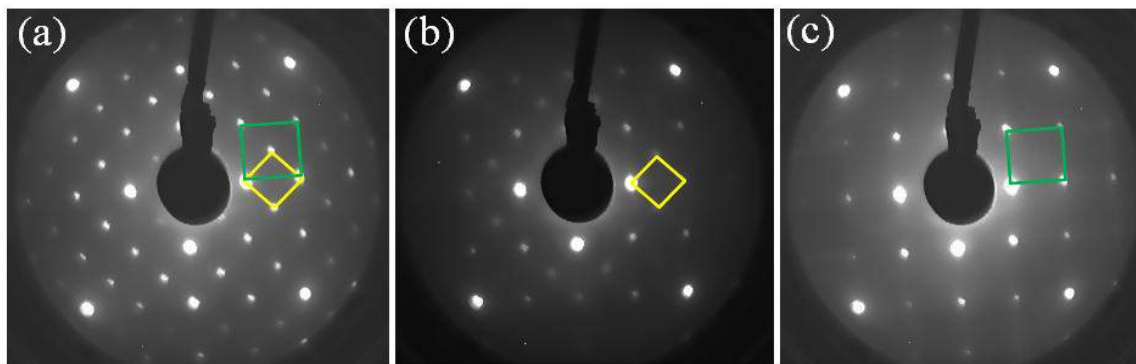


**Figure 6.5** LEED patterns acquired from the Fe<sub>3</sub>O<sub>4</sub>(001) surface with an electron energy of 90 eV. (a) Clean surface. The yellow square shows the  $(\sqrt{2}\times\sqrt{2})R45^\circ$  periodicity of the surface reconstruction, whereas the green square indicates the  $(1\times 1)$  unit cell. (b) After exposure to 1.2 L HCOOH at 70 K, the  $(\sqrt{2}\times\sqrt{2})R45^\circ$  periodicity is maintained, although the spots are less intense than for the clean surface. (c) After exposure to 5 L HCOOH at room temperature, the spots associated with the  $(\sqrt{2}\times\sqrt{2})R45^\circ$  are absent and the surface exhibits a  $(1\times 1)$  periodicity (green square).

## Chapter 6. Adsorption of Formic Acid on the Fe<sub>3</sub>O<sub>4</sub> (001) Surface

Since the half-order spots are absent at all energies, this observation implies that the  $(\sqrt{2}\times\sqrt{2})R45^\circ$  reconstruction is lifted by the dissociative adsorption of HCOOH. At 70 K, however, following exposure to 1.2 L of HCOOH, close to saturation of the dissociated species according to XPS, the LEED pattern retains some intensity of the  $(\sqrt{2}\times\sqrt{2})R45^\circ$  superstructure (Figure 6.5c).

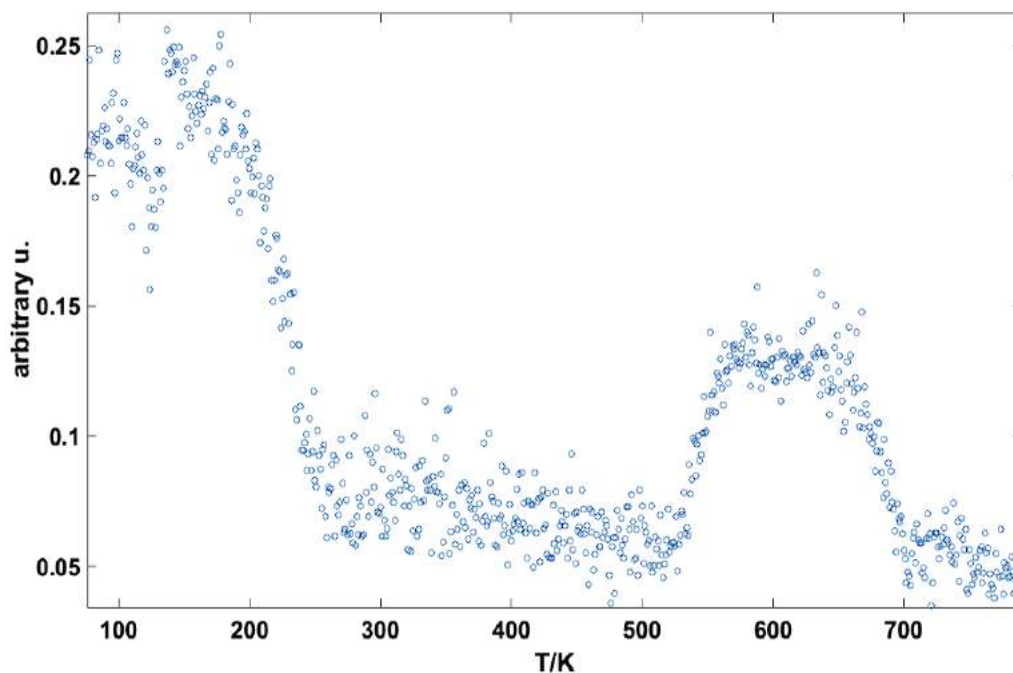


**Figure 6.6** Intensity variation of the  $(\sqrt{2}\times\sqrt{2})R45^\circ$  reconstruction spots of the Fe<sub>3</sub>O<sub>4</sub>(001) surface after exposure to 1.2 L HCOOH at 70 K and subsequent annealing until 800 K. The associated LEED patterns were acquired with an electron energy of 90 eV.



## Chapter 6. Adsorption of Formic Acid on the Fe<sub>3</sub>O<sub>4</sub> (001) Surface

Figure 6.6 shows the intensity variation of the  $(\sqrt{2}\times\sqrt{2})R45^\circ$  reconstruction spots  $(3/2, 1/2)$  of the Fe<sub>3</sub>O<sub>4</sub>(001) surface after exposure to 1.2 L HCOOH at 70 K and subsequent annealing up to 800 K at 1 K/s. This plot was obtained taking LEED patterns of the sample while the temperature was increasing. Between 100 and 200 K, the intensity of the reconstruction spots remain constant, which indicates the stability of the reconstruction on the surface. Around 200 K the intensity of the reconstruction spot decreases dramatically and reaches a minimum around 280 K. The intensity remains constant from this point until around 526 K where the intensity of the reconstruction spots increases. This change is related with the formic acid decomposition and desorption from on the surface, as will be shown in section 6.3.5. Once the intensity of the reconstruction spots increases at around 526 K, its intensity remains constant until a drop of the intensity occurs around 700 K, which is thought to be related with an order-disorder phase transition on the surface (75).

### 6.3.4 Scanning Tunneling Microscopy

Following a nominal exposure of 1L HCOOH on the Fe<sub>3</sub>O<sub>4</sub>(001) surface at room temperature (Figure 6.7a), the Fe rows of the substrate are completely obscured. Patches of circular protrusions related to formic acid species (corrugation, 20 pm) are separated by areas characterized by streaks in the fast-scan direction of the STM (vertical in the image). Such streaks typically result from weakly bound molecules moving under the influence of the STM tip. The protrusions have a nearest neighbor distance of 5.9 Å in the [1-10] direction, which corresponds to every other Fe atom along the Fe<sub>oct</sub> row. In some cases the nearest neighbor is 5.9 Å away in the [1-10] direction (the yellow line in Figure 6.7a joins two such protrusions), which corresponds to equivalent sites on the neighboring Fe row. In other areas neighboring protrusions are located 6.6 Å away at an angle  $\pm 26.6^\circ$  from the [110] axis (orange line in Figure. 6.7a).

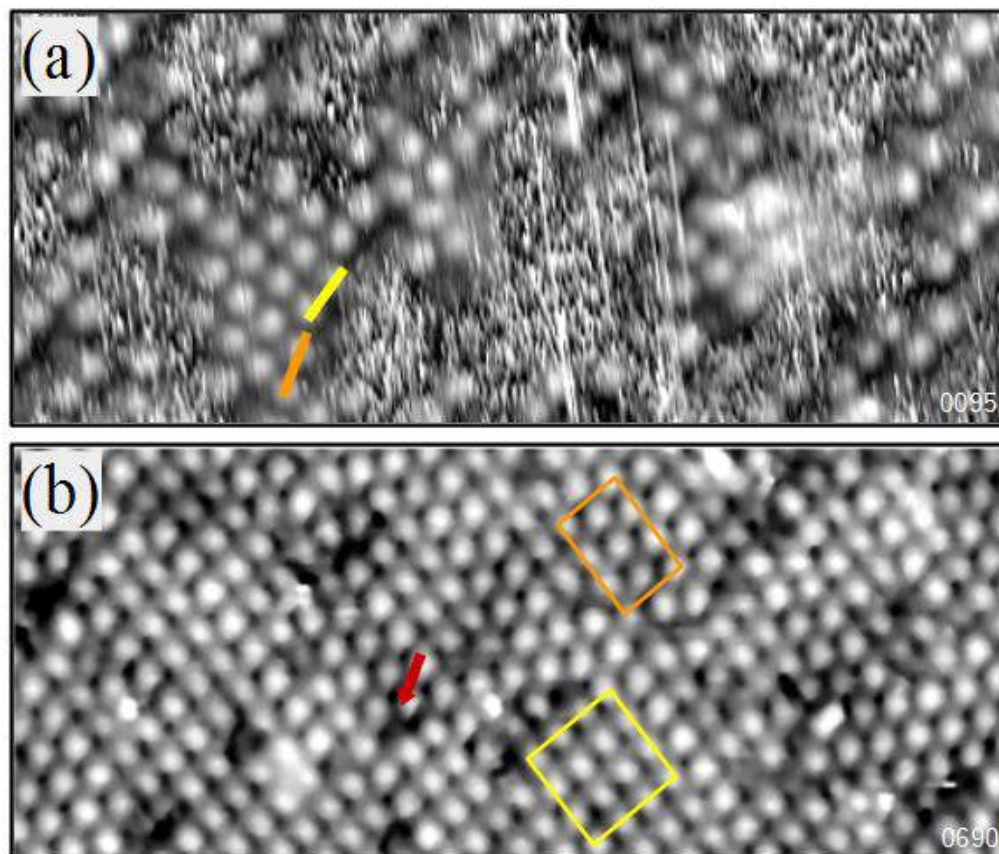


**Figure 6.7** STM images of the Fe<sub>3</sub>O<sub>4</sub>(001) surface following exposure to HCOOH at room temperature. (a) After exposure to 1 L HCOOH, the surface is characterized by protrusions associated with formate species, and areas obscured by rapidly diffusing molecules ( $20 \times 10 \text{ nm}^2$ ,  $V_{\text{sample}} = +1.5 \text{ V}$ ,  $I_{\text{tunnel}} = 0.1 \text{ nA}$ ). (Fast scan direction vertical.) (b) After dosing 10 L of HCOOH, close packed formate species cover the surface ( $20 \times 10 \text{ nm}^2$ ,  $V_{\text{sample}} = +1.5 \text{ V}$ ,  $I_{\text{tunnel}} = 0.1 \text{ nA}$ ). Two local orderings of the protrusions are observed, (1×1) (within the yellow square) and (2×1) (within the orange rectangle). The red arrow points to a 9 Å gap between protrusions in the [110] direction; at either side of which the local order switches between (1×1) and (2×1).

## Chapter 6. Adsorption of Formic Acid on the Fe<sub>3</sub>O<sub>4</sub> (001) Surface

When the exposure is increased to 10 L HCOOH, the surface is covered by a nearly complete over layer of protrusions (Figure. 6.7b). In some areas the protrusions are arranged with a square pattern with a nearest neighbor distance of 5.9 Å (one such patch is indicated by the yellow square); this corresponds to a (1×1) registry with the substrate. In other areas the protrusions are arranged with a local (2×1) order. This order is an extension of the 6.6 Å configuration observed in Figure 6.7b (orange rectangle). Occasionally, a row of protrusions running in the [110] direction exhibits a gap of 9 Å (red arrow), which results in a switch of the local ordering with the neighboring protrusions.

Figure 6.8 shows a schematic representation of the ordering observed in STM (Figure 6.7b) superimposed on a Fe<sub>3</sub>O<sub>4</sub>(001)-(1×1) surface (unit cell indicated by black square). The blue rectangles represent bridging bidentate formate bound to two surface Fe<sub>oct</sub> atoms along the row between subsurface Fe<sub>tet</sub> atoms. In the (1×1) ordered area formate binds to symmetrically equivalent Fe<sub>oct</sub> pairs, but the (2×1) ordering formate requires that an inequivalent Fe<sub>oct</sub> pair is occupied that straddles the line between two subsurface Fe<sub>tet</sub> atoms (green). Note that in the centre of Figure 6.8 one Fe<sub>oct</sub> atom is not occupied by formate; this results in a distance of 9 Å between formate species along the row direction, as observed experimentally at the border between the (1×1) and (2×1) phases (Figure 6.7).

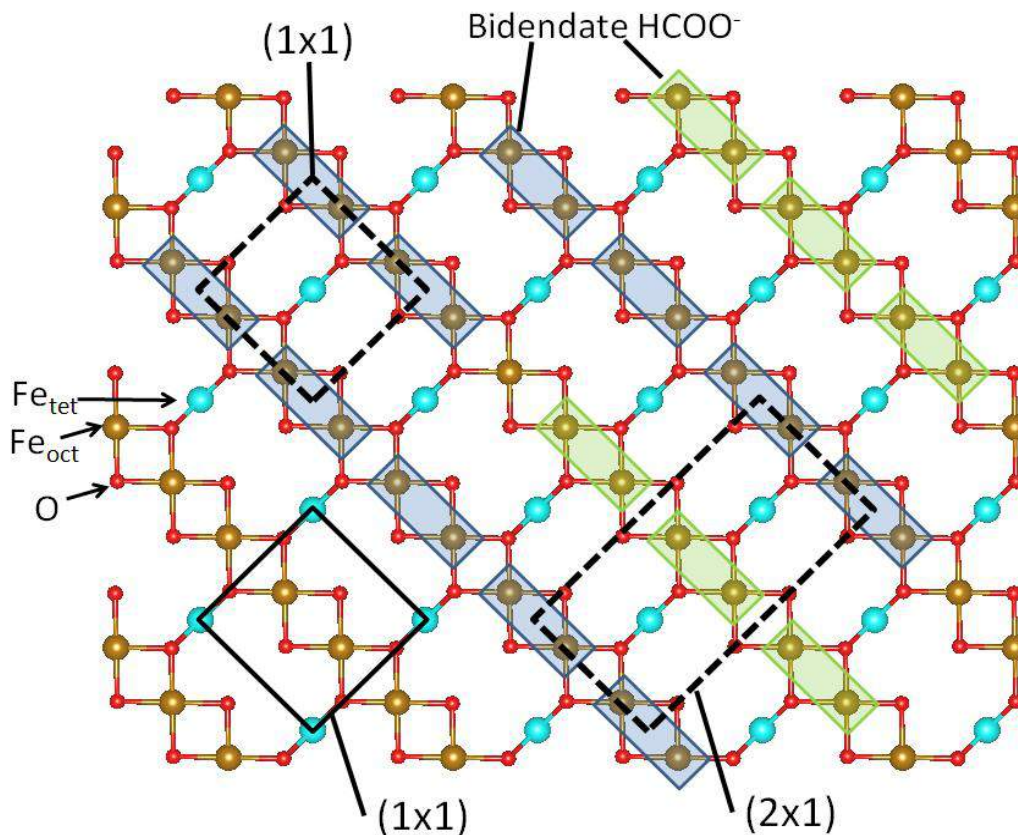


**Figure 6.8.** Schematic model of bridging bidentate formate adsorption on a Fe<sub>3</sub>O<sub>4</sub>(001)- (1×1) surface. Blue rectangles represent formate bound to an Fe<sub>oct</sub> pair located in the center of four subsurface Fe<sub>tet</sub> atoms (cyan), whereas green rectangles represent formate bound to an Fe<sub>oct</sub> pair that straddles the line between two subsurface Fe<sub>tet</sub>. A (1×1) periodicity can be formed by either the green or blue formate, both configurations are required to form the (2×1) periodicity observed in STM.

### 6.3.5 Temperature Programmed Desorption Spectroscopy

Figure 6.9 shows a series of desorption spectra observed on the Fe<sub>3</sub>O<sub>4</sub>(001) surface exposed to formic acid (HCOOH) at 100 K. At low exposures (<0.4 L) a weak HCOOH<sup>+</sup> (m/z =47) desorption signal was observed between 450 and 550 K. After exposure of more than 0.6 L HCOOH, a new peak appears at 275 K. The peak increases in intensity, shifts to lower temperature with increasing HCOOH exposures, and saturates at around 1.2 L (violet curve). According to literature, the signal at 275 K could be attributed to the recombination of surface formates with surface hydroxyl groups. The desorption between 450 and 550 K is related to decomposition of the monolayer of bidentate formate species as will be discussed later (28, 130).

Interestingly, the saturation of the 275 K peak occurs at 1.2 L, which is double that of the high temperature peak (0.6 L, red curve). This suggests that a monolayer can be formed with a density of 4 HCOOH per ( $\sqrt{2}\times\sqrt{2}$ )R45° unit cell, or one molecule per surface Fe<sub>oct</sub> cation.

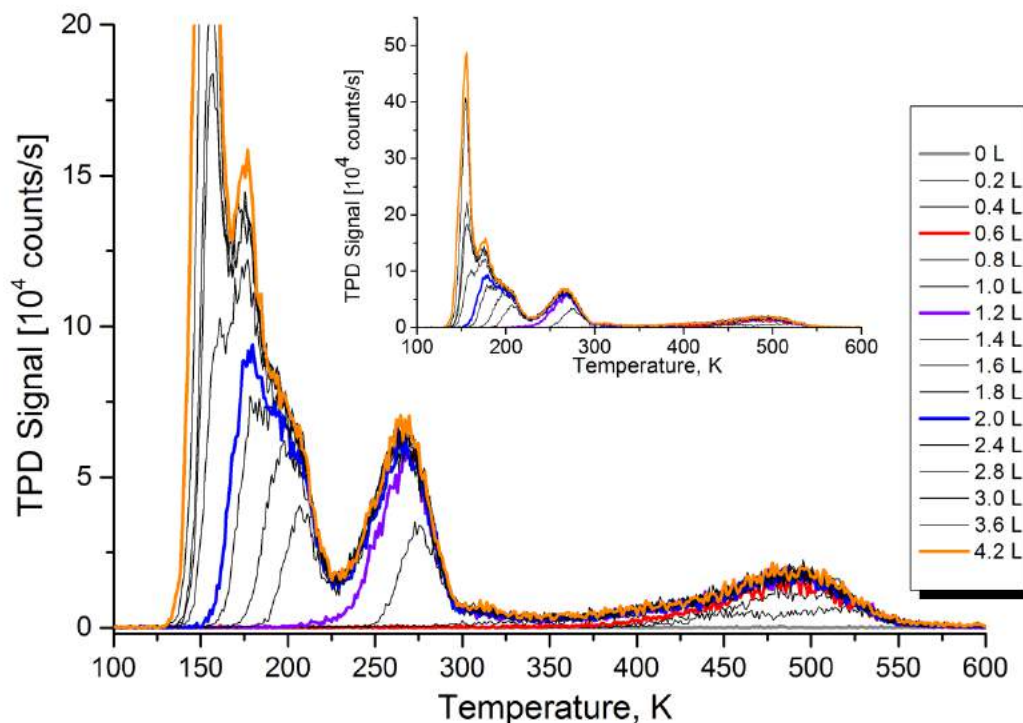


**Figure 6.9** TPD spectra of formic acid on Fe<sub>3</sub>O<sub>4</sub> (001) surface, monitored at  $m/z=47$ , for several dosing values.

Above an exposure of about 1.4 L of HCOOD a new peak emerges that shifts from 208 to 177 K with increasing exposure. Finally, above 2.4 L a new TPD peak appears at 155 K. This lower temperature peak is associated with multilayer desorption as observed on other oxides (28, 146).

The major decomposition products for the thermal decomposition of HCOOD on the Fe<sub>3</sub>O<sub>4</sub> (001) surface were CO, CO<sub>2</sub>, H<sub>2</sub>O, and H<sub>2</sub>CO, similar to those reported on the rutile TiO<sub>2</sub> (110) surface (130). These products were released with the high temperature desorption of HCOOD. No H<sub>2</sub> was observed.

Figure 6.9 shows TPD results from  $m/z$  values 18 (a), 28 (b), 44 (c) and 29 (d) respectively, as a function of HCOOD exposure. The spectra can be separated in two regions. The low temperature region, between 100 and 350 K, and the high temperature region from 350 to 700 K.

## Chapter 6. Adsorption of Formic Acid on the Fe<sub>3</sub>O<sub>4</sub> (001) Surface

Comparison of the desorption signals in the low temperature region for the spectra in figure 6.9 with those for HCOOD (Figure 6.8) suggests that the signals in this region resulted from the mass spectrometer cracking of HCOOD species from desorption of formic acid species and multilayer desorption.

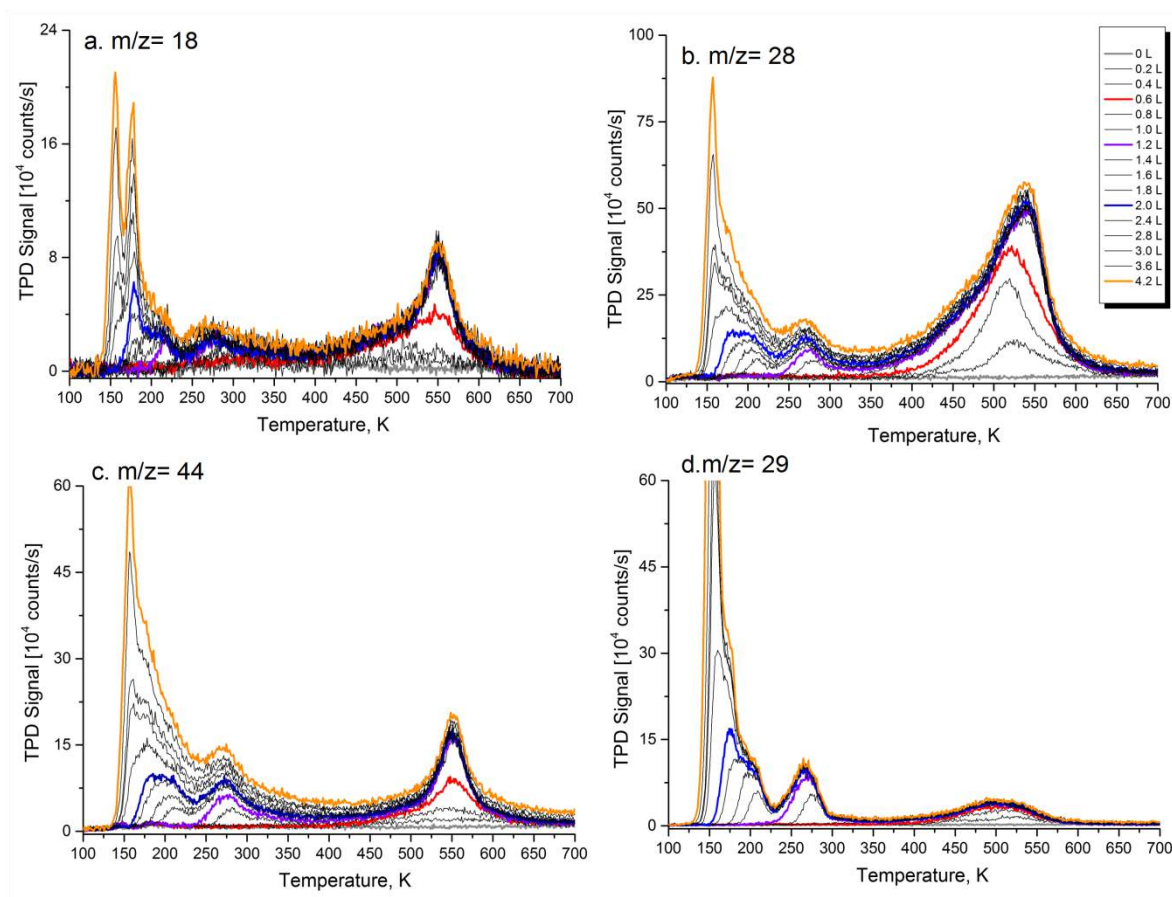


**Figure 9** TPD spectra of the Fe<sub>3</sub>O<sub>4</sub> (001) surface exposed to HCOOD. (a) m/z =18, (b) m/z = 28, (c) m/z = 44. (d) m/z = 29.

The spectra in figure 6.9 show in each case (a,b,c,d) signals at 155 K associated with mass spectrometer cracking of formic acid from multilayer desorption. The peak between 250 and 300 K increases in intensity for each mass as a function of increasing HCOOD exposure, and also results from mass spectrometer cracking of HCOOD species (28, 146). The spectra for m/z = 18 (Figure 6.9a) shows an additional peak at 177 K, which could be the result of small amounts of water

## Chapter 6. Adsorption of Formic Acid on the Fe<sub>3</sub>O<sub>4</sub> (001) Surface

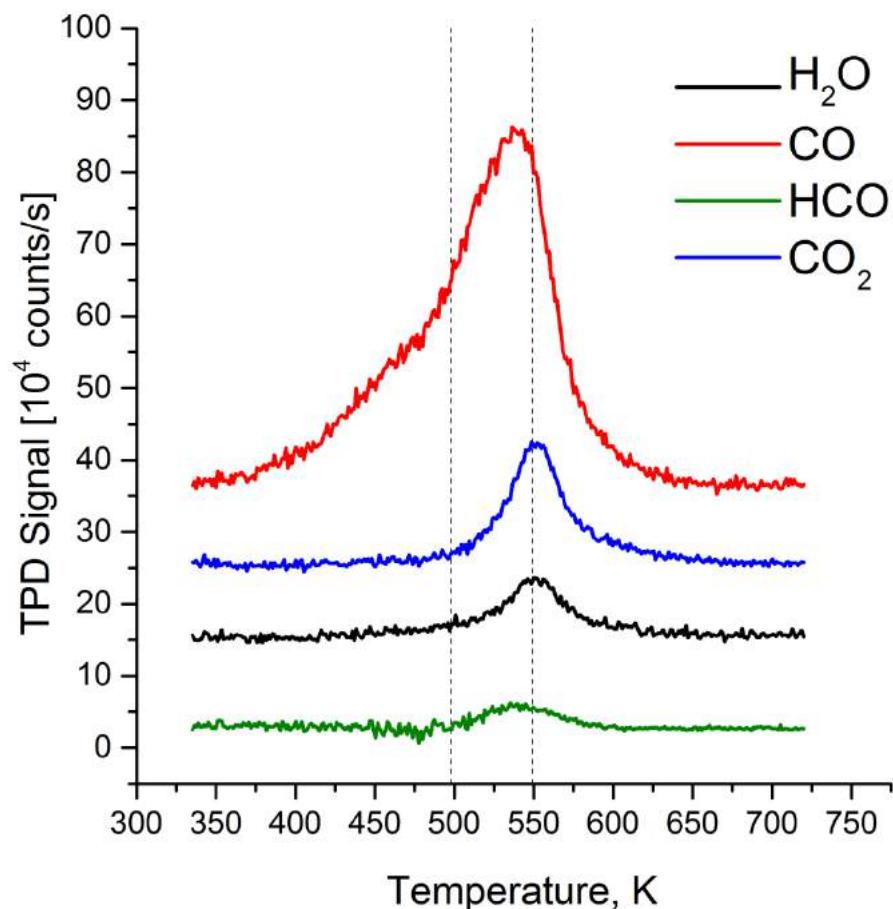
dosed with the formic acid, presumably as an impurity in the source material (28, 147).

In order to analyze the high temperature region and assign the signals at  $m/z$  18, 28, 29, and 44 with H<sub>2</sub>O, CO, CHO (this mass is monitored because it is the strongest cracking fragment for H<sub>2</sub>CO), and CO<sub>2</sub> respectively, a deconvolution process for these signals was carried out. A series of spectra (following the masses of interest) were taken after exposure of the sample to 4.2 L of HCOOD.

First, each spectrum of the signals mentioned above (18, 28, 29 and 44) was superimposed with an appropriate scaling, to the spectra for the mass 47 using as reference the multilayer desorption peak (155 K). Afterward, both superimposed spectra ( $m/z$  47 and the mass under study) are subtracted in order to discount the contribution, that comes from the mass spectrometer cracking of HCOOD in each species.

A particular case was the signal for mass 28, which would have contributions from CO desorption, but also from fragmentation of HCOOD and CO<sub>2</sub>. Here, after the subtraction of the signal coming from fragmentation of mass 47 contributing to the signal at mass 28, a second subtraction of the signal coming from fragmentation of mass 44 contributing to the signal at mass 28 was made, using the sensitivity factor determined using the fragmentation pattern of CO<sub>2</sub> dosed directly into our mass spectrometer (mass 44).





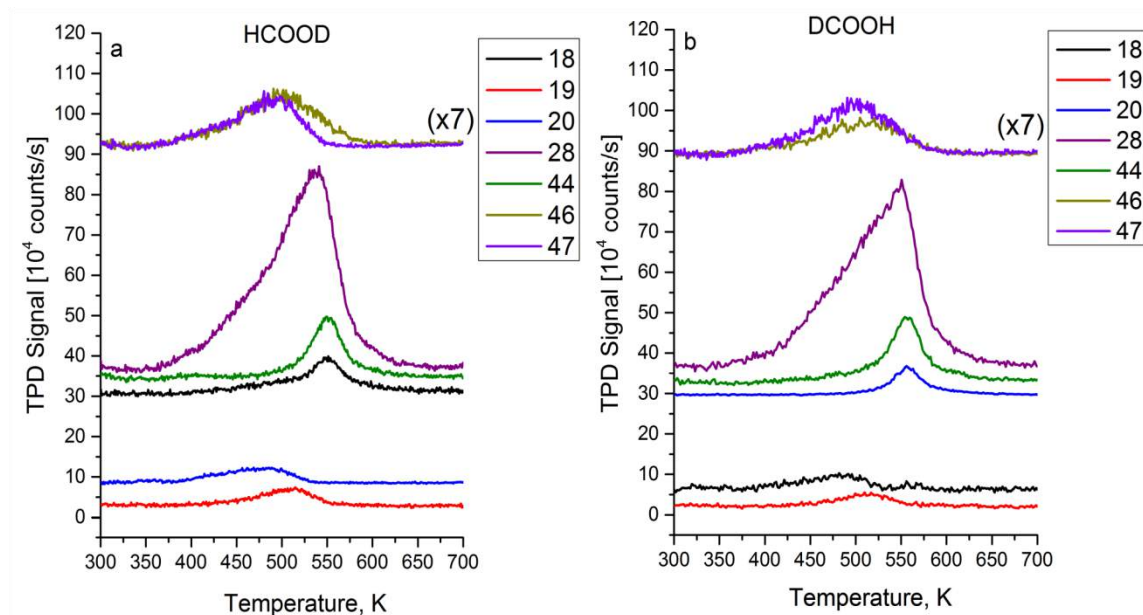
**Figure 6.10** Deconvoluted TPD spectra of the Fe<sub>3</sub>O<sub>4</sub> (001) surface exposed to 4.2 L HCOOD for H<sub>2</sub>O, CO, H<sub>2</sub>CO and CO<sub>2</sub>.

Figure 6.10 shows the deconvoluted TPD spectra for H<sub>2</sub>O, CO, HCO and CO<sub>2</sub>. The products observed in the high temperature region are related to decomposition reactions of the formate surface species. The CO signal (red spectrum), appears to be the result of two overlapping peaks located around 500 and 550 K. The CO<sub>2</sub> (blue spectrum) and H<sub>2</sub>O (black spectrum) signals show only one peak at 550 K. The green spectrum shows the signal for HCO, which presents a broad desorption signal whose maximum is located around 540 K.

Figure 6.11 shows temperature-programmed desorption spectra for m/z 18, 19, 20, 28, 44, 46 and 47, obtained following exposure of the Fe<sub>3</sub>O<sub>4</sub>(001) surface to 3.6 L of HCOOD (Figure 6.11a) and DCOOH (Figure 6.11b). In both cases, the primary

## Chapter 6. Adsorption of Formic Acid on the Fe<sub>3</sub>O<sub>4</sub> (001) Surface

decomposition products were CO, with CO<sub>2</sub> and water. Signals related to hydrogen production were not detected. In the case of HCOOD the mass which appears at 20 is related to D<sub>2</sub>O and in the case of DCOOH the mass corresponding to 18 is related to H<sub>2</sub>O.



**Figure 6.11** TPD spectra of the Fe<sub>3</sub>O<sub>4</sub> (001) surface exposed to 3.6 L (a) HCOOD and (b) DCOOH. The spectra are displayed on the same intensity scale. The spectra are plotted according to their desorption behavior and offset for clarity.

### 6.4. Discussion: Formic Acid on Fe<sub>3</sub>O<sub>4</sub>(001)-( $\sqrt{2}\times\sqrt{2}$ )R45° Surface

#### 6.4.1. Adsorption Behavior

Magnetite is characterized by a high degree of ionicity in the metal-oxygen bond. Consequently, the atoms are charged, and the reactivity of the surface can be understood in terms of acid-base reactions (5, 7, 16). The XPS and IRRAS data presented here show that HCOOH is adsorbed dissociatively at room temperature

## Chapter 6. Adsorption of Formic Acid on the Fe<sub>3</sub>O<sub>4</sub> (001) Surface

to form formate on the Fe<sub>3</sub>O<sub>4</sub> (001) surface. At low temperature, however, the formic acid showed both, molecular and dissociative adsorption.

Dissociation is facile in the system because the Fe<sup>3+</sup> cations and O<sup>2-</sup> anions are very close together on the surface (2 Å), which promotes an acid-base reaction. We propose that formate binds through its O atoms to two neighboring Fe atoms along the Fe<sub>oct</sub> row in a bridging bidentate configuration. A similar adsorption geometry was measured on the TiO<sub>2</sub>(110) surface (148), where the Ti-Ti separation is similar to the Fe-Fe separation here (3 Å).

STM suggests that, at room temperature, the adsorption of formic acid results in two bridging bidentate formate species per each ( $\sqrt{2}\times\sqrt{2}$ )R45° reconstruction unit cell, with two OH groups formed at the O atoms. These species are responsible for the high temperature desorption peak observed for TPD of m/z =47 (Figure 6.9).

TPD of HCOOD (Figure 6.9) shows that 1.2 L, which is twice the amount needed to saturate the high temperature peak (peak corresponding to two formate species per unit cell), is the amount to saturate the desorption peak at 275 K. Moreover, comparing the areas for the C1s spectra at 1.2 L for adsorption at room temperature and adsorption at 70 K, shows a bigger area for the low temperature data (around 50%).

These observations suggest that four HCOOH per ( $\sqrt{2}\times\sqrt{2}$ )R45° unit cell are adsorbed at low temperature (70K), two of them are formate species, and the other two are intact formic acid molecules, presumably adsorbed to the subsurface Fe<sub>tet</sub>, or forming hydrogen bonds. In the light of this assignment, the peak observed in TPD (Figure 6.9) around 280 K is attributed to the desorption of the two formic acid molecules.

The desorption of the two formic acid molecules mentioned above is linked to the lifting of the ( $\sqrt{2}\times\sqrt{2}$ )R45° reconstruction, as observed in LEED at room temperature (see figure 6.5c). Lifting the reconstruction must involve the relocation

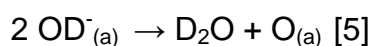
## Chapter 6. Adsorption of Formic Acid on the Fe<sub>3</sub>O<sub>4</sub> (001) Surface

of the 2<sup>nd</sup> layer interstitial Fe<sub>tet</sub> atom that underlies the subsurface rearrangement (37), and has been observed previously following saturation of the surface by atomic hydrogen (76), and water (149) (150). How the desorption of formic acid causes the necessary rearrangement of the subsurface cations to lift the ( $\sqrt{2}\times\sqrt{2}$ )R45° reconstruction is not yet clear, but it appears to be linked to the rearrangement of the subsurface induced by hydrogen atoms, which occurs in all cases. We currently entertain the possibility that the H atom, or even an hydroxyl group generated by the dissociation process of the formic acid, could be incorporated into the subsurface, filling the subsurface cation vacancy site responsible for the reconstruction. Theoretical calculations are being carried out by our collaborators to get more insight.

While the formate is clearly identified in the room temperature data, the OH species expected on the basis of equation (2) are not detected by IRRAS, imaged by STM, nor uniquely resolved in the O 1s XPS spectrum. We note, however, that DFT calculations predict the OH bond to be parallel to the surface (76), which makes detection by IRRAS problematic. Also, the corrugation of the STM images is dominated by the formate species at high coverage, and the substrate is obscured by loosely bound HCOOH molecules already at low coverage. Finally, where we expect to find the OH peak in O 1s XPS, we also find the formate peak which has double the intensity.

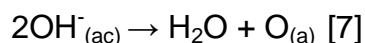
### 6.4.2. Desorption Behavior

TPD indicates that the primary pathway for the decomposition of formates on Fe<sub>3</sub>O<sub>4</sub> (001) surface was dehydration to CO. Here CO desorbed simultaneously with water during decomposition of formate at 550 K (Figure 6.10). The evolution of H<sub>2</sub>O and CO at the same temperature can be explained in terms of formate decomposition on dehydration process, as follows (28):



This process would be in line with the observation in figure 6.11, where desorption of D<sub>2</sub>O (m/z= 20) was observed on the DCOOH experiment (Figure 6.11b) , while H<sub>2</sub>O (m/z= 18) was observed in the case of HCOOD (Figure 6.11a).

The water observed below 500 K would then related with desorption of water involving the acidic proton. Here, the water could be result from condensation of two hydroxyl groups formed at two coordinate oxygen sites, for the case of DCOOH (Figure 6.11b) would be represented by :



In the case of HCOOD (Figure 6.11a), the product will be D<sub>2</sub>O.

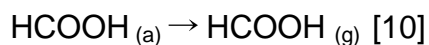
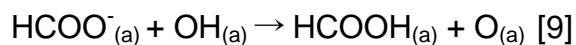
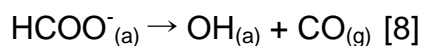
The observation of CO desorption at 500 and 550 K suggests that there are two pathways for decomposition on the surface. Similar results were observed on ZrO<sub>2</sub>(001), where different pathways were attributed to different surface terminations. On ZrO<sub>2</sub>, the low-temperature peak was assigned to decomposition of formates coordinated to cations adjacent to oxygen vacancies, while the high-temperature peak was assigned to decomposition on stoichiometric portions of the surface (151). In previous chapters (3,5), we described the presence of defects on

## Chapter 6. Adsorption of Formic Acid on the Fe<sub>3</sub>O<sub>4</sub> (001) Surface

Fe<sub>3</sub>O<sub>4</sub>(001) surface and their effect on the local electronic structure; specifically to the presence of Fe<sup>2+</sup> cations in the surface layers. These defects have shown different reactivity than the stoichiometric surface (reactivity to methanol, chapter 5). Based on this, it could be expected a similar behavior could occur with respect to CO evolution on the Fe<sub>3</sub>O<sub>4</sub> (001) surface as the observed on the ZrO<sub>2</sub> (001) surface.

Together with carbon monoxide, formaldehyde and CO<sub>2</sub> were observed. The formaldehyde was present in a peak around 540 K (Figure 6.10). Formaldehyde production has been related to the presence of low coordination and reduced surface cation sites. (28, 135, 151, 152). Its formation has been attributed to the disproportionation of formates (135, 151, 153), as was described above (Equation 3). Once again, the presence of formaldehyde as decomposition product seems to be related with defect sites on Fe<sub>3</sub>O<sub>4</sub>(001) surface, APDB and incorporated-Fe point defects.

Between 500 and 550 K formic acid (HCOOH) desorption was observed, which coincides with the evolution of CO. Similar behavior was observed on the TiO<sub>2</sub> (001) surface, where it was suggested that formate decomposition feeds the surface with protons and CO, these protons forms hydroxyl groups, which are available for reaction with other formate species to produce formic acid, according to (152):



The O<sub>(a)</sub> could react with CO to CO<sub>2</sub> or diffuse into the bulk.

## Chapter 6. Adsorption of Formic Acid on the Fe<sub>3</sub>O<sub>4</sub> (001) Surface

In fact, as was observed in Figure 6.11a the evolution of mass 46, which would correspond to HCOOH, presents a higher signal, which correspond to the product on reaction 9. It would be expected that in the case of DCOOH (Figure 6.11b), where the formate species would be DCOO<sup>-</sup>, the formic acid species created in the reaction will be DCOOD.

### 6.5 Adsorption of HCOOH on the Fe-Dimer Surface

To test for the influence of surface structure the adsorption of formic acid on the Fe-Dimer surface was studied using STM and XPS.

Figure 6.12 shows the Fe<sub>3</sub>O<sub>4</sub> (001) surface (Figure 6.12a) and the Fe-Dimer Fe<sub>3</sub>O<sub>4</sub> (001) surface (Figure 6.12b) after dosing 10 L of HCOOH at room temperature. As described above, when the Fe<sub>3</sub>O<sub>4</sub> (001) surface is exposed to 10 L HCOOH, the surface is covered by a nearly complete over layer of protrusions (Figure 6.12a). Again, two local orderings of the protrusions are observed; (1×1) (yellow square) and (2×1) (orange rectangle).

After dosing 10 L of HCOOH on the Fe-Dimer Fe<sub>3</sub>O<sub>4</sub> surface (Figure 6.12b), the surface is covered by protrusions with similar orderings as observed on the clean Fe<sub>3</sub>O<sub>4</sub> surface (yellow square). The red square highlights a region where a new adsorption configuration is observed. Here, green ovals show a couple of protrusions elongated. This new adsorption configuration could mean an increase of formate species on the Fe-Dimer surface due the presence of the two extra octahedral Fe atoms per reconstructed unit cell. Here a new bridging bidentate formate will bind as follows: one oxygen of the formate molecule to one Fe atom in the octahedral iron row and the second oxygen atom of the formate on one of the Fe atoms of the dimer.

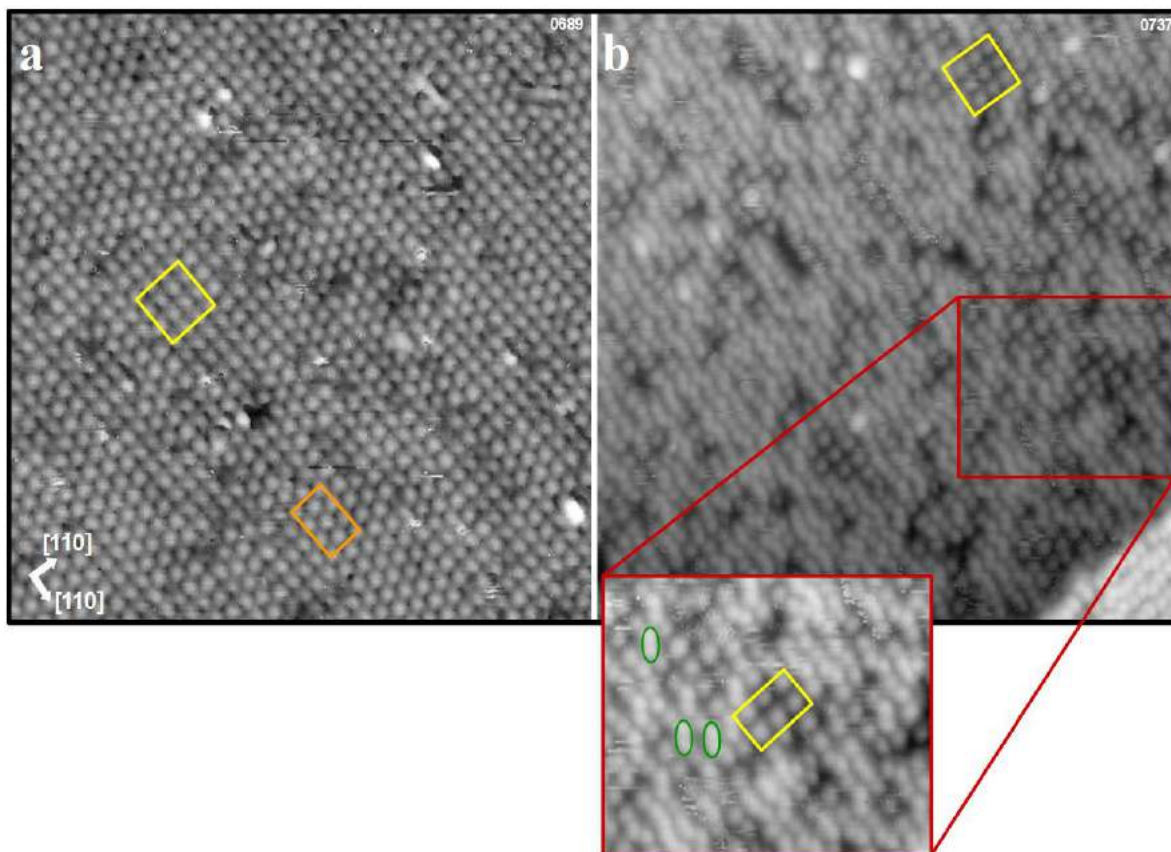


**Figure 6.12** STM images of the (a) clean Fe<sub>3</sub>O<sub>4</sub>(001) surface after dosing 10 L of HCOOH (20 x 20 nm<sup>2</sup>, V<sub>sample</sub>=1.5 V, I<sub>tunnel</sub>= 0.3 nA). (b) Fe-Dimer Fe<sub>3</sub>O<sub>4</sub> surface after dosing 10 L of HCOOH (20 x 20 nm<sup>2</sup>, V<sub>sample</sub>=1.6 V, I<sub>tunnel</sub>= 0.3 nA).

Figure 6.13 shows a schematic representation of the possible adsorption of formic acid on the Fe-Dimer Fe<sub>3</sub>O<sub>4</sub> surface. Here, the black dotted circles represent the position of the Fe-Dimer. The blue rectangles represent bridging bidentate formate bound to two surface Fe<sub>oct</sub> atoms along the row. The green rectangles represent bridging bidentate formate bound to one surface Fe<sub>oct</sub> atoms on the row and to one Fe atom on a dimer.



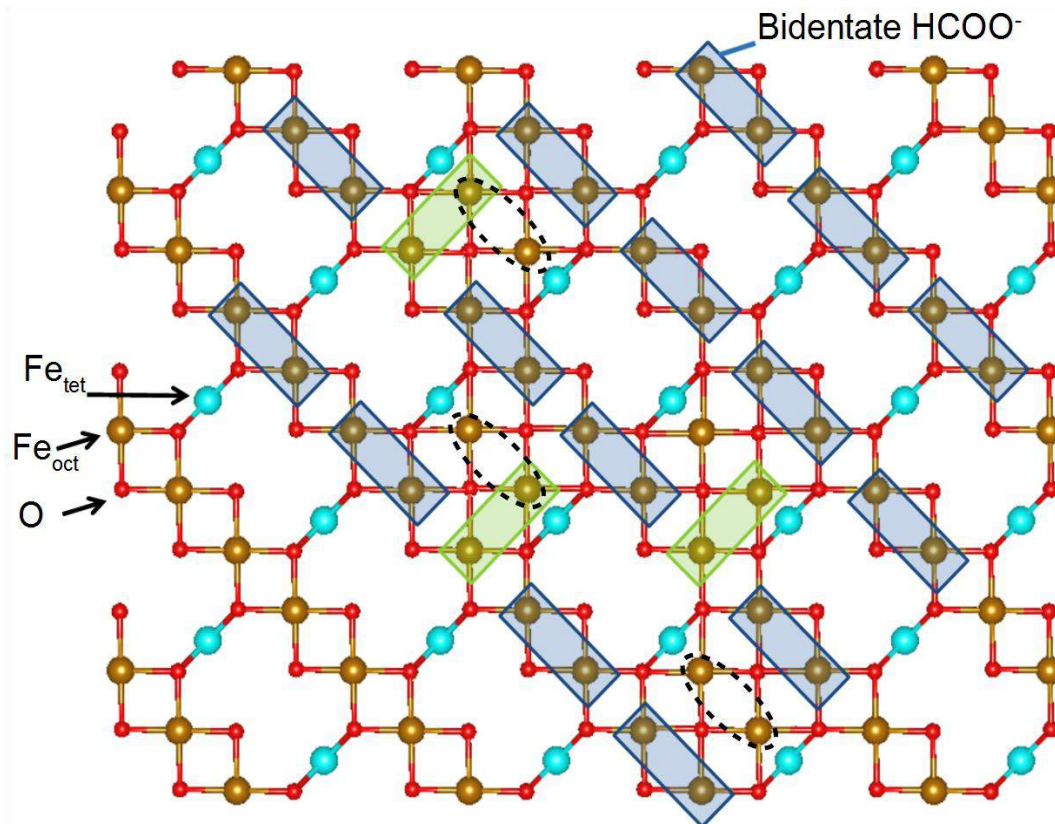


**Figure 6.13** Schematic model of bridging bidentate formate adsorption on a Fe<sub>3</sub>O<sub>4</sub>(001)- (1×1) surface and on a Fe-Dimer Fe<sub>3</sub>O<sub>4</sub> (001) surface. Black dotted circle rectangles highlight the position of the Fe-Dimer. Blue rectangles represent a formate bound to an Fe<sub>oct</sub> pair located in the octahedral Fe rows, whereas green rectangles represent a formate bound to an Fe atoms pair, one of them located in the Fe<sub>oct</sub> rows and the other Fe atom on the dimer.

## Chapter 6. Adsorption of Formic Acid on the Fe<sub>3</sub>O<sub>4</sub> (001) Surface

Photoemission spectra that were recorded in the OMEGA UHV system after that different Fe<sub>3</sub>O<sub>4</sub> surface terminations were exposed to 10 L of HCOOH at room temperature are shown in Figure 6.14.

The C 1s spectra are shown in Figure 6.14a. The C 1s region has no detectable carbon signal for the clean Fe<sub>3</sub>O<sub>4</sub>(001) surface (black line). Following the adsorption of formic acid on the clean surface a symmetric peak centered at 288.7 eV appears, which has been associated to formate species (red line, see also Figure 6.14a above).

On the 0.5 ML Fe / Fe<sub>3</sub>O<sub>4</sub>(001) surface a peak appears at the same position (blue line), its area is 25% larger than the one obtained for the clean surface. The Fe-dimer Fe<sub>3</sub>O<sub>4</sub> surface (2 ML Fe / Fe<sub>3</sub>O<sub>4</sub>(001) surface) after HCOOH adsorption (10 L HCOOH) shows a peak centered at the same energy as the previous cases, but with an area 50% larger than the signal obtained for the clean surface (orange line).

The O 1s spectra are shown in Figure 6.14b. The Fe<sub>3</sub>O<sub>4</sub>(001) surface exhibits a slightly asymmetric peak at 530.1 eV as described above (78). Adsorption of HCOOH produces an additional shoulder on the high-energy side (red line) which is consistent with both surface OH groups and formate species (101).

The blue and orange line shows the O 1s spectra for the Fe deposited surfaces (0.5 ML Fe/ Fe<sub>3</sub>O<sub>4</sub>(001) and 2 ML Fe/ Fe<sub>3</sub>O<sub>4</sub>(001)) respectively. As the coverage of Fe on the sample increases, the intensity of the shoulder on the high-energy side due to formic acid adsorption increases (compare inset in Figure 6.14b). The Fe-Dimer Fe<sub>3</sub>O<sub>4</sub> surface has the highest intensity, which is in agreement with the observations on the C 1s region.

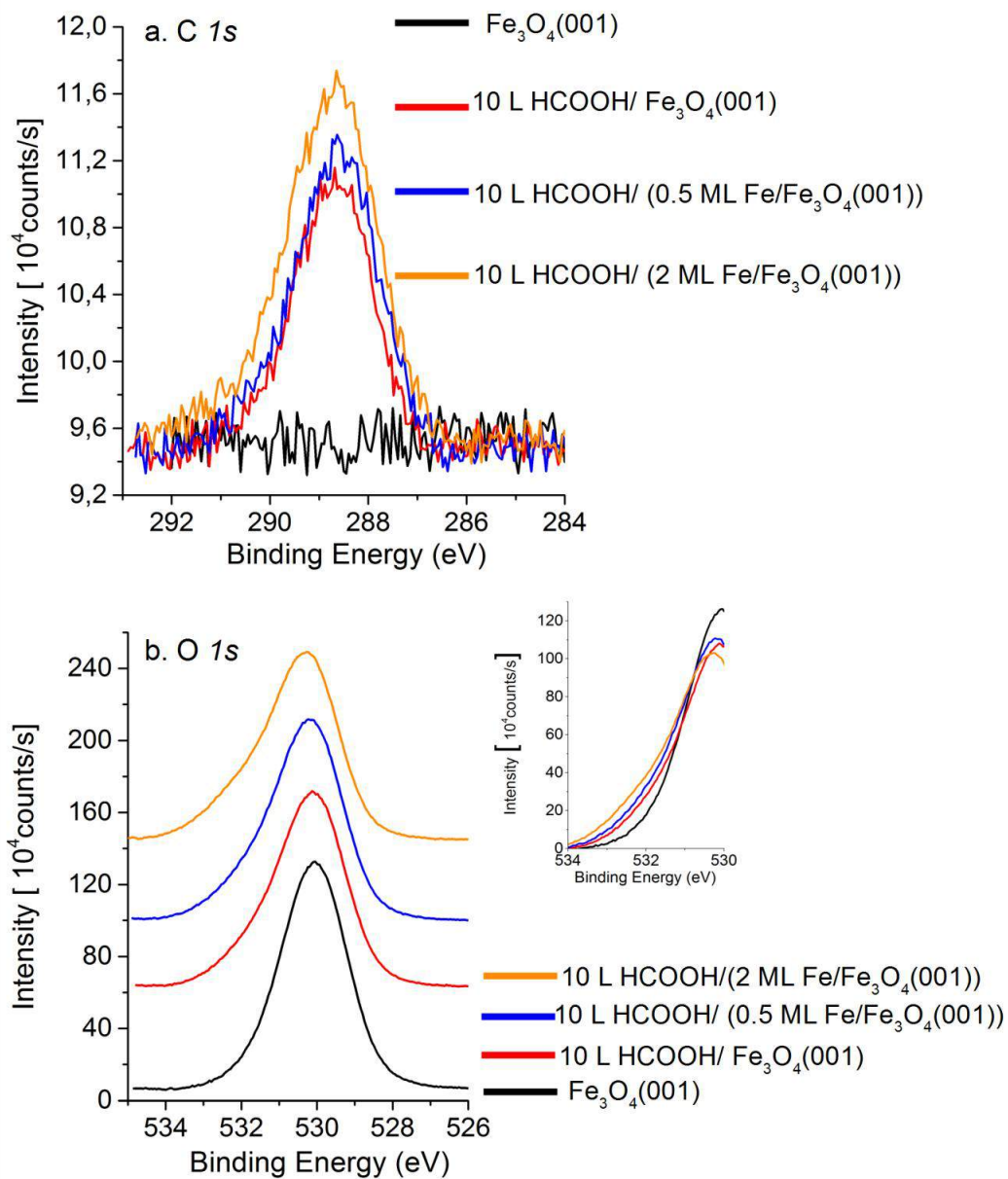


**Figure 6.14** XPS spectra of different Fe<sub>3</sub>O<sub>4</sub> surface terminations exposed to 10 L of HCOOH at room temperature (a) C 1s and (b) O 1s.

## Chapter 6. Adsorption of Formic Acid on the Fe<sub>3</sub>O<sub>4</sub> (001) Surface

According with STM and XPS measurements, the adsorption of formic acid on the Fe-Dimer surface increases in comparison with the SCV reconstructed Fe<sub>3</sub>O<sub>4</sub>(001) surface. The Fe-Dimer surface exposes two extra octahedral Fe atoms per reconstructed unit cell, where the Fe-Fe separation is similar to the Fe-Fe separation on the Fe<sub>oct</sub> row . These under-coordinated cations would be active sites for dissociation of formic acid in a bridging bidentate configuration.

### 6.6 Conclusions

Formic acid dissociates on the Fe<sub>3</sub>O<sub>4</sub>(001)-( $\sqrt{2}\times\sqrt{2}$ )R45° surface yielding a layer of bridging bidentate formate and surface hydroxyl groups. The adsorption can be understood in terms of acid-base chemistry where the close proximity of under-coordinated Fe<sup>3+</sup>/O<sup>2-</sup> cation/anion pairs facilitate the dissociation. Bridging bidentate formate groups show two different periodicities according with STM images, one with (1×1) symmetry and a second with (2×1) symmetry.

The adsorbed formate decomposes to produce CO, H<sub>2</sub>O, CO<sub>2</sub> and H<sub>2</sub>CO. The presence of surface defects seems to affect the reactivity of adsorbed formate species.

The increase of the under-coordinated Fe atoms on the magnetite surface plays an important role on the adsorption of formic acid. Here the Fe-dimer surface, which exposes two extra octahedral Fe atoms per reconstructed unit cell, with respect to the SCV reconstructed surface, showed an increases of the capacity for formic acid dissociation.

# 7. The Water Gas Shift Reaction on the Fe<sub>3</sub>O<sub>4</sub>(001) Surface: Related Adsorption Experiments

## 7.1 Introduction

The water gas shift reaction (WGS) is one of the most important processes in the fuel industry and one of the most studied reactions in the catalysis field. The reaction is an exothermic process and is expressed by:



The process is mainly used for the production of hydrogen from synthesis gas, which is then used for ammonia production, petroleum refineries, and as fuel for power generation (154, 155).

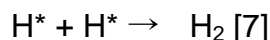
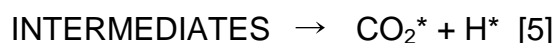
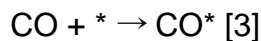
The reaction can be carried out over a wide temperature range. Two general regimes have been proposed: the high-temperature WGS and the low-temperature WGS (154, 156). The high-temperature regime involves temperatures of 350-500 °C. Here, catalysts based on the oxides of iron and chromium (Fe<sub>2</sub>O<sub>3</sub>-Cr<sub>2</sub>O<sub>3</sub>) are widely used. It is important to mention that the active phase of these catalysts is Fe<sub>3</sub>O<sub>4</sub>, which is obtained by reduction of Fe<sub>2</sub>O<sub>3</sub>. Oxides such as Cr<sub>2</sub>O<sub>3</sub> and Al<sub>2</sub>O<sub>3</sub> are used to minimize sintering and increase the stability (157). Low-temperature WGS is performed in a range of 190-250 °C, normally on Cu-based catalysts. Here Cu is dispersed on oxides such as ZnO, and Al<sub>2</sub>O<sub>3</sub>, which act as textural promoters and stabilizer for the Cu clusters (158-160).

In the industrial applications, both stages of WGS are used. First, the high temperature stage is used due its favorable kinetics. Afterwards, a low temperature

## Chapter 7. The Water Gas Shift Reaction on the Fe<sub>3</sub>O<sub>4</sub>(001) Surface: Related Adsorption Experiments

stage follows, in which the thermodynamic equilibrium is favored in order to minimize the concentration of CO (155).

The mechanism of the WGS reaction has been the subject of many different theoretical (161-163) and experimental studies (164-166). Two main mechanisms have been proposed to explain the reaction. The associative mechanism and the regenerative mechanism (also known as redox mechanism) (167). The associative mechanism was proposed first by Armstrong and Hilditch during their studies with copper chromite catalyst (168). Here is proposed that CO and H<sub>2</sub>O adsorb on the catalyst surface, and water dissociates on the surface, followed by the reaction between adsorbed OH and CO species to form surface intermediates that subsequently decompose into CO<sub>2</sub> and H<sub>2</sub>. The associative mechanism could be described in general by the following reactions :



Where \* represents a surface adsorption site, and X\* is an adsorbed X species (167).

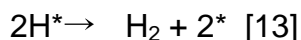
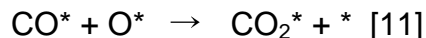
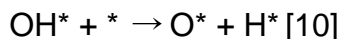
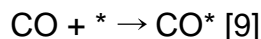
The associative mechanism has been shown to occur in different systems. On CeO<sub>x</sub>/Au(111) species such as formates (HCOO<sup>-</sup>) and carbonates (CO<sub>3</sub><sup>2-</sup>) have

## Chapter 7. The Water Gas Shift Reaction on the Fe<sub>3</sub>O<sub>4</sub>(001) Surface: Related Adsorption Experiments

been identified as surface intermediates(165). Formate species have also has been shown to be surface intermediates on ZnO (169) and ZrO<sub>2</sub>-supported Pt catalysts (166). On the other hand, theoretical studies have proposed intermediates such as carboxyl (HOCO) as the dominant intermediate in this reaction and the presence of species such as formaldehyde (CH<sub>2</sub>O) and formyl (HCO) as others possible intermediates of the reaction (158, 162, 170).

The regenerative mechanism, also described by Armstrong and Hildithch, proposes that CO is adsorbed on the surface and is then oxidized by oxygen from the metal oxide. Then the reduced support is re-oxidized by steam, producing hydrogen (47).

New suggestions show the regenerative mechanism as a Langmuir-Hinshelwood process (170). Here, CO and H<sub>2</sub>O adsorb on the surface and water dissociates on the surface, followed by CO oxidation. Finally, H<sub>2</sub> and CO<sub>2</sub> desorb from the surface. This process can be described as follows:



Due its industrial importance magnetite should receive special interest. Recent DFT calculations have determined that the regenerative mechanism is the

## Chapter 7. The Water Gas Shift Reaction on the Fe<sub>3</sub>O<sub>4</sub>(001) Surface: Related Adsorption Experiments

energetically most favorable pathway for the WGS on the Fe<sub>oct2-tet1</sub> terminated Fe<sub>3</sub>O<sub>4</sub>(111) surface (66). The regenerative mechanism has been also confirmed on Fe-based catalysts by in-situ DRIFTS experiments (171). On the other hand, isotope tracer experiments on WGS over iron based catalysts have shown that both the regenerative and the associative mechanism were consistent with experimental observations (172). Nevertheless, although on chromia- promoted magnetite catalysts under water gas shift conditions the formation of formate was observed, these species have been attributed as inactive surface species for the reaction (173). This panorama shows the necessity to make further investigations on the mechanism of WGS on magnetite surfaces in order to offer a best knowledge about the system, which could improve its industrial applications.

### 7.2 The WGS on Fe<sub>3</sub>O<sub>4</sub>(001) Surface

In order to get details about the WGS reaction on the Fe<sub>3</sub>O<sub>4</sub>(001) surface, a series of XPS measurements were performed using the synchrotron radiation facilities of Max-lab in collaboration with Jan Knudsen from the Synchrotron radiation research group at Lund University. As a first approximation to the reaction, here we will focus on the study of the co-adsorption of CO and H<sub>2</sub>O on the Fe<sub>3</sub>O<sub>4</sub>(001) surface.

C1s, O1s and Fe2p spectra were recorded in a differentially pumped high pressure XPS setup with an electrostatic pump analyzer, at photon energies of 390, 650 and 850 eV, respectively, which results in a kinetic energy of the photoelectrons of 110-130 eV.

Figure 7.1 shows C1s, O1s, and Fe2p spectra that were recorded after the Fe<sub>3</sub>O<sub>4</sub>(001) surface was exposed to CO and H<sub>2</sub>O. The C1s spectra are shown in Figure 7.1a. When the surface is freshly prepared the C1s region has no detectable carbon signal (orange spectra). The purple spectrum in figure 7.1a was taken after exposure of the sample to 1 x 10<sup>-8</sup> mbar of CO and 1 x 10<sup>-6</sup> mbar of H<sub>2</sub>O at room temperature. The spectrum shows a small signal around 285 eV. The following three spectra (black lines) were taken under the same conditions for CO



## Chapter 7. The Water Gas Shift Reaction on the Fe<sub>3</sub>O<sub>4</sub>(001) Surface: Related Adsorption Experiments

and H<sub>2</sub>O. Here is observed that, as the exposure time increases, the intensity for the peak at 285 eV also increases. In addition, two new signals begin to be resolved at 286.9 and 288.7 eV.

The red spectrum was taken after increasing the pressure of CO to  $1 \times 10^{-6}$  mbar while the pressure of H<sub>2</sub>O was kept on  $1 \times 10^{-6}$  mbar. The intensity of the mentioned peaks increases, and much better resolved. The blue spectrum was taken with the same conditions. After taking this spectra, the CO flow was removed completely, and the pressure of H<sub>2</sub>O was increased to  $1 \times 10^{-5}$  mbar. The remaining spectra were taken under these conditions; here the intensity of the peaks increases dramatically with the exposure time.

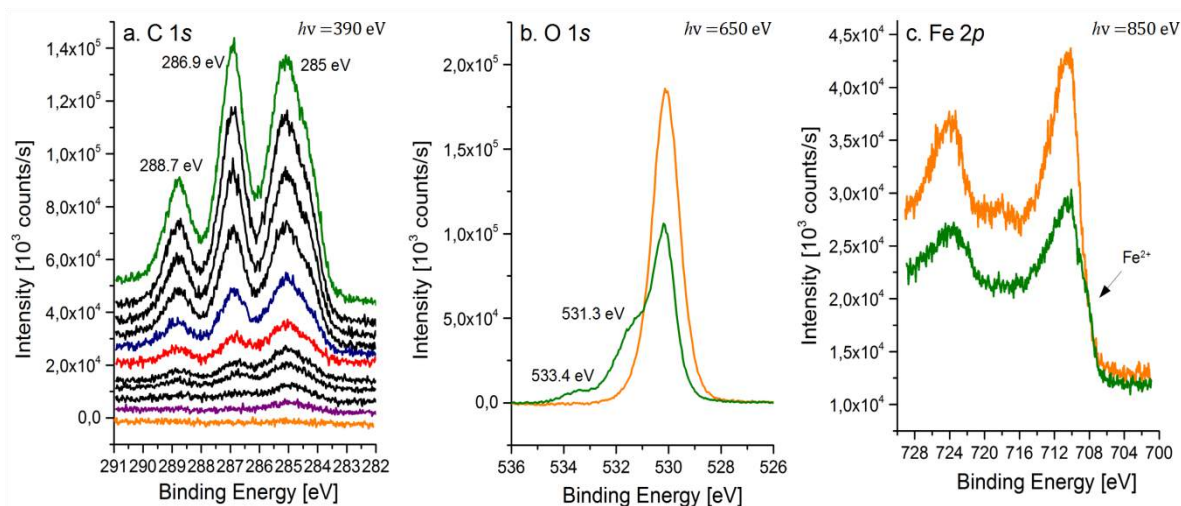


**Figure 7.1.** a. Sequential C 1s XPS spectra from CO and H<sub>2</sub>O co-exposed at room temperature on the Fe<sub>3</sub>O<sub>4</sub>(001) surface. The data are offset in the y-direction for clarity. b. O 1s XPS spectra for the clean Fe<sub>3</sub>O<sub>4</sub>(001) surface (orange line) and after exposure of CO and H<sub>2</sub>O at room temperature (green line). c. Fe 2p XPS spectra before (orange) and after (green) the exposure of CO and H<sub>2</sub>O at room temperature on the clean Fe<sub>3</sub>O<sub>4</sub>(001)-( $\sqrt{2} \times \sqrt{2}$ )R45° surface. See text for gas exposure conditions.

Figure 7.1b shows a direct comparison of the O 1s spectra for the clean surface (orange spectrum) and the surface after exposure of CO and H<sub>2</sub>O (green spectrum), which corresponds to the same conditions for the green spectra in the Figure 7.1a. The exposure of CO and H<sub>2</sub>O decreases the intensity of the lattice oxygen peak, and two peaks emerge on the high-energy side at approximately 531.3 and 533.4 eV. The Fe 2p spectra are shown in Figure 7.1c. The surface after exposure (green spectrum), taken at the same conditions as the C 1s and O 1s on green spectra, shows a shoulder around 708 eV, which is attributed to Fe<sup>2+</sup> contributions (78).

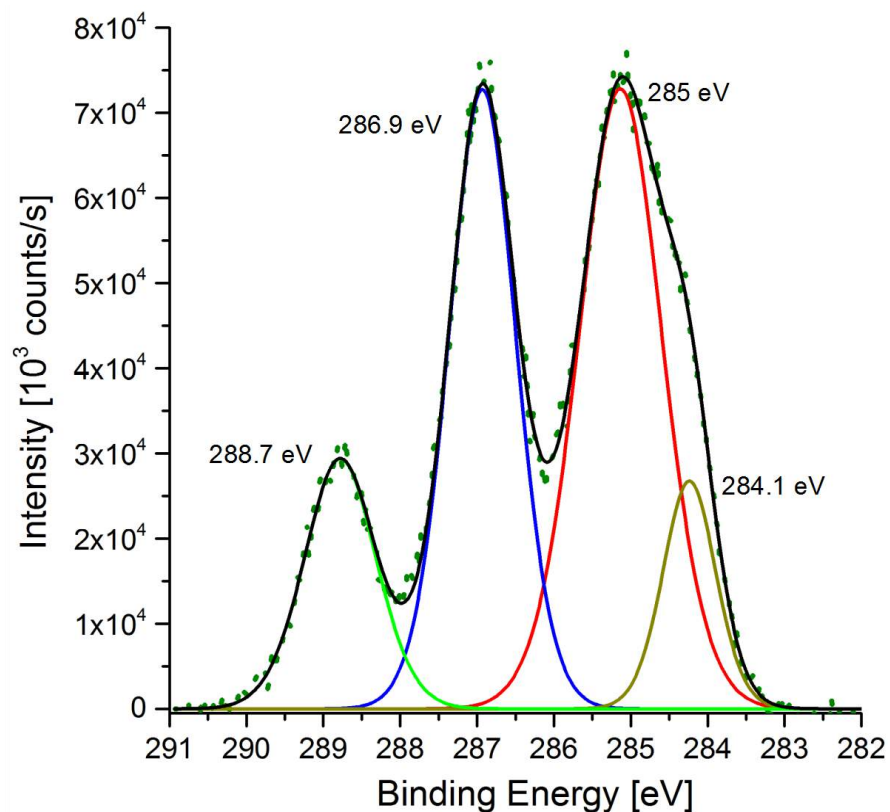


**Figure 7.2.** C 1s XPS ( $h\nu=390$  eV) spectra of the Fe<sub>3</sub>O<sub>4</sub>(001) surface after exposure to CO and H<sub>2</sub>O at room temperature. The signal is deconvoluted into four peaks.

## Chapter 7. The Water Gas Shift Reaction on the Fe<sub>3</sub>O<sub>4</sub>(001) Surface: Related Adsorption Experiments

Figure 7.2 shows the C 1s signal corresponding to the green spectrum in Figure 7.1a, which can be deconvoluted into four peaks using a Gaussian/Lorentzian (30) line shape. The fitting parameters are listed in Table 7.1, including peak position, full width at half maximum FWHM, and concentration.

Position (eV)	FWHM (eV)	% Concentration
288.7	1.1	14
286.9	1.0	33
285	1.3	43
284.1	0.8	10

**Table 7.1.** Deconvolution parameters of the C 1s peaks measured at Max-lab for the Fe<sub>3</sub>O<sub>4</sub>(001) surface exposed to CO and H<sub>2</sub>O.

An interesting observation was made when CO and H<sub>2</sub>O were dosed separately onto the sample in different experiments. Figure 7.3a shows the C 1s spectra following exposure to 1mbar of CO at room temperature, and Figure 7.3b shows the C 1s spectra when the sample was exposed to 1 x 10<sup>-6</sup> mbar of H<sub>2</sub>O at room temperature. Here is important to mention that during the exposure experiments is not possible to discount the presence of traces of H<sub>2</sub>O in the CO experiment coming from the background and from the CO reagent, as well as the presence of CO in the water experiments. Nevertheless, these results show that the carbon species are not just the result of CO adsorption. Here, the water has an important role to catalyze the buildup of carbon species on the surface.

## Chapter 7. The Water Gas Shift Reaction on the $\text{Fe}_3\text{O}_4(001)$ Surface: Related Adsorption Experiments

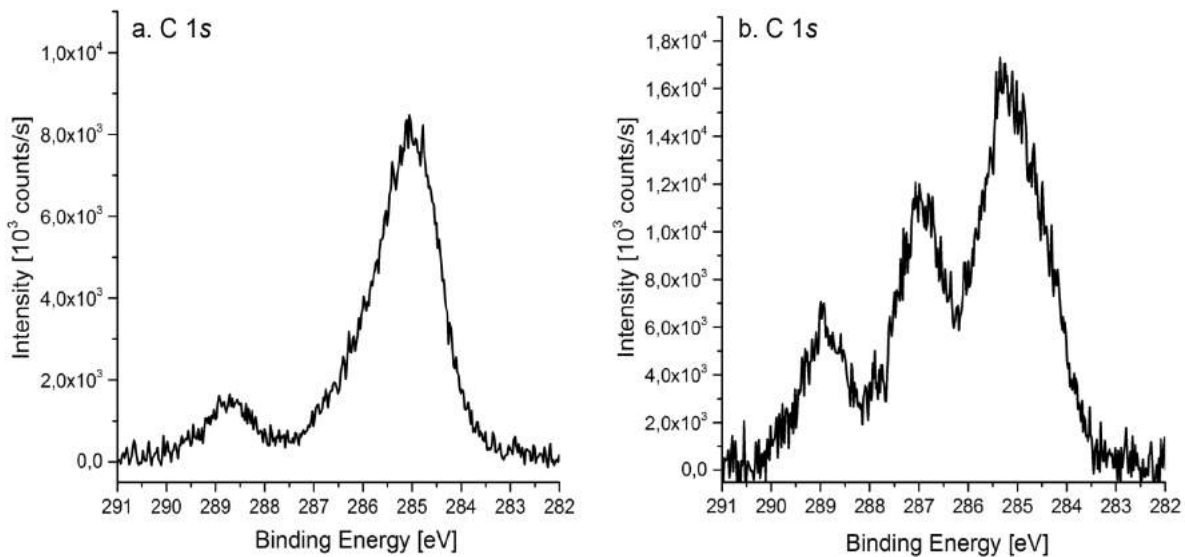


**Figure 7.3.** a. C 1s XPS spectra from CO (1mbar) adsorbed at room temperature on the  $\text{Fe}_3\text{O}_4(001)$ . b. C 1s XPS spectra from  $\text{H}_2\text{O}$  ( $1 \times 10^{-6}$  mbar) adsorbed at room temperature on the  $\text{Fe}_3\text{O}_4(001)$  surface ( $h\nu=390$  eV).

## Chapter 7. The Water Gas Shift Reaction on the $\text{Fe}_3\text{O}_4(001)$ Surface: Related Adsorption Experiments

Similar experiments were carried out in our OMEGA system at TU Wien. Here, the co-adsorption of CO and  $\text{H}_2\text{O}$  on the surface was studied using STM and XPS.

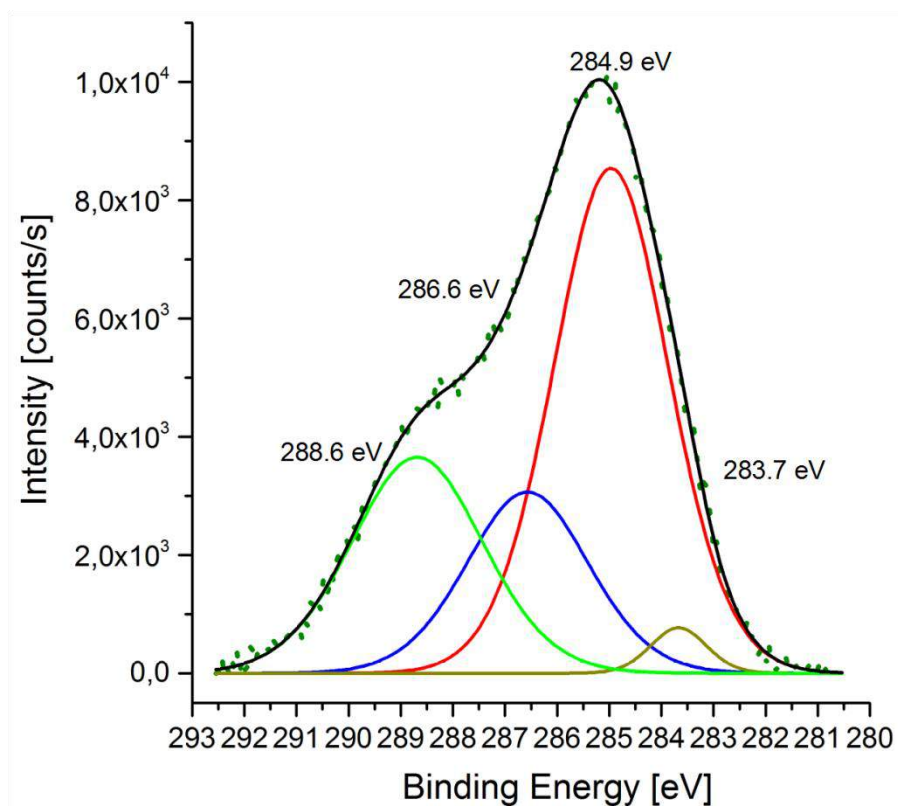


**Figure 7.4.** C 1s XPS spectra of the  $\text{Fe}_3\text{O}_4(001)$  surface taken following exposure to  $1 \times 10^{-8}$  mbar of CO and  $1 \times 10^{-5}$  mbar of  $\text{H}_2\text{O}$  for one hour at room temperature in the OMEGA system using non-monochromatized Al K $\alpha$  X-rays and a SPECS PHOIBOS 150 electron analyzer with a pass energy of 90 eV.

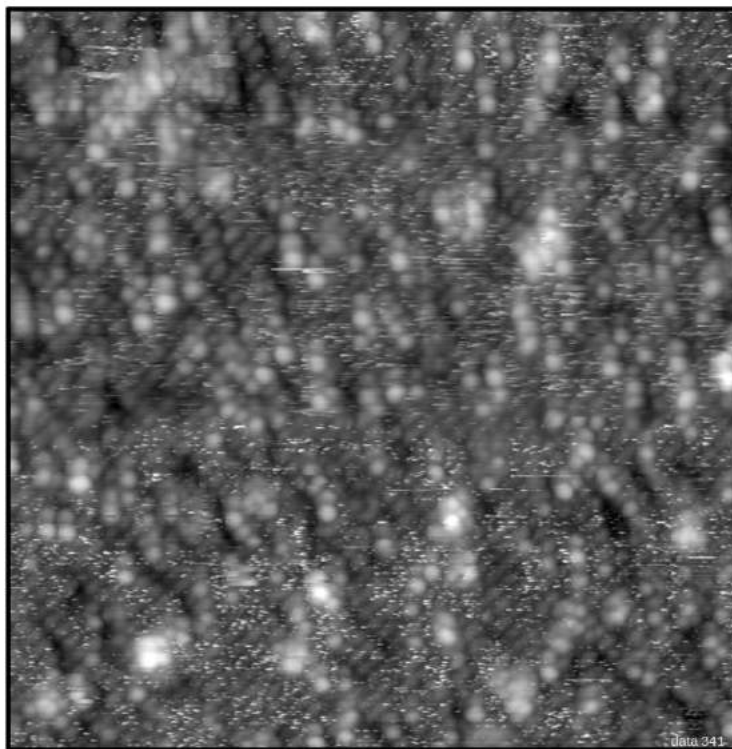
## Chapter 7. The Water Gas Shift Reaction on the Fe<sub>3</sub>O<sub>4</sub>(001) Surface: Related Adsorption Experiments

Figure 7.4 shows the C 1s photoemission spectra that were recorded after the Fe<sub>3</sub>O<sub>4</sub>(001) surface was exposed to  $1 \times 10^{-8}$  mbar of CO and  $1 \times 10^{-5}$  mbar of H<sub>2</sub>O for one hour at room temperature. The signal can be deconvoluted into four peaks as in the previous case (Gaussian/Lorentzian [30]). The fitting parameters are listed in Table 7.2 including peak position, full width at half maximum FWHM, and concentration.

Position (eV)	FWHM (eV)	% Concentration
288.6	2.9	26
286.6	2.8	20
284.9	2.6	52
283.7	1.3	2

**Table 7.2.** Deconvolution parameters of the C 1s peaks measured at OMEGA system for the Fe<sub>3</sub>O<sub>4</sub>(001) surface exposed to CO and H<sub>2</sub>O.

Figure 7.5 shows an STM image of the Fe<sub>3</sub>O<sub>4</sub>(001) surface after the exposure to  $1 \times 10^{-8}$  mbar of CO and  $1 \times 10^{-5}$  mbar of H<sub>2</sub>O for one hour at room temperature. A high density of bright protrusions appears as a consequence of the co-dosing experiment. Moreover, the iron rows appears as straight rows of bright protrusions, akin to the completely hydroxylated surface after adsorption of hydrogen atoms (75). After the co-dosing experiment the surface exhibits a (1×1) symmetry in LEED, which suggests that the reconstruction is lifted.



**Figure 7.5.** STM image of  $\text{Fe}_3\text{O}_4(001)$  surface ( $30 \times 30 \text{ nm}^2$ ;  $V_{\text{sample}} = +1.8 \text{ V}$ ;  $I_{\text{tunnel}} = 0.15 \text{ nA}$ ) after to exposure to  $1 \times 10^{-8} \text{ mbar}$  of CO and  $1 \times 10^{-5} \text{ mbar}$  of  $\text{H}_2\text{O}$  for one hour at room temperature.

### 7.3. Discussion: The WGS on $\text{Fe}_3\text{O}_4(001)$ Surface

The results presented here suggest the formation of C-containing intermediate species after the  $\text{Fe}_3\text{O}_4(001)$  surface was exposed to water and carbon monoxide at room temperature. The C  $1s$  signal is resolved into four peaks at 288.7, 286.9, 285, and 284.1 eV (Figure 7.1a). The peak at 285 eV could be assigned to carbon in the form of graphite or  $\text{CH}_x$  hydrocarbon fragments (164, 174). As observed in Figure 7.3a, this was the main species after the surface was exposed to 1 mbar CO. This signal could be the result of CO adsorption or come from hydrocarbon impurities in the gas. Similar observations have been reported after exposure of carbon monoxide on clean iron surfaces, and on the surface of native thin oxide films on polycrystalline iron (175, 176).

## Chapter 7. The Water Gas Shift Reaction on the Fe<sub>3</sub>O<sub>4</sub>(001) Surface: Related Adsorption Experiments

The position for the peak at 284.1 eV could be assigned to the presence of iron carbides compounds (Fe<sub>x</sub>C) (175, 177, 178). The peak at 288.7 eV was assigned to formate species, since the position in the C 1s spectra is the same as that observed after exposure the surface to formic acid at room temperature (Chapter 6). The assignment of the peak at 286.9 eV is challenging.

As mentioned above, species such as HOCO, CH<sub>2</sub>O (formaldehyde), and HCO (formyl) have been theoretically studied, and proposed as possible intermediates in the WGS reaction (162, 170). The carboxylate species has been predicted to have a short surface lifetime during the reaction between OH groups and CO (165, 179).

We hypothesize that the C 1s signal at 286.9 eV could be due to formaldehyde.

To evaluate if formaldehyde was indeed the C-containing intermediate species after the co-adsorption of water and carbon monoxide at room temperature, its adsorption on the Fe<sub>3</sub>O<sub>4</sub>(001) surface was studied in a separate experiment.

Figure 7.6 shows the C 1s photoemission spectra that were recorded after the Fe<sub>3</sub>O<sub>4</sub>(001) surface was exposed to 0.9 L of HCOH at 60 K, and subsequently annealed to progressively higher temperatures.

The C 1s region has no detectable C signal when the surface is freshly prepared. Following the adsorption of formaldehyde at 60 K a peak centered at 288.9 eV appears. When the sample is heated to 100 K, the signal appears to have contributions from two peaks, at 288.9 and 287.5 eV, respectively. With increase of temperature, the C 1s peak at 287.5 eV dominates the spectra. Upon heating, this peak decreases in intensity until it disappears around room temperature.



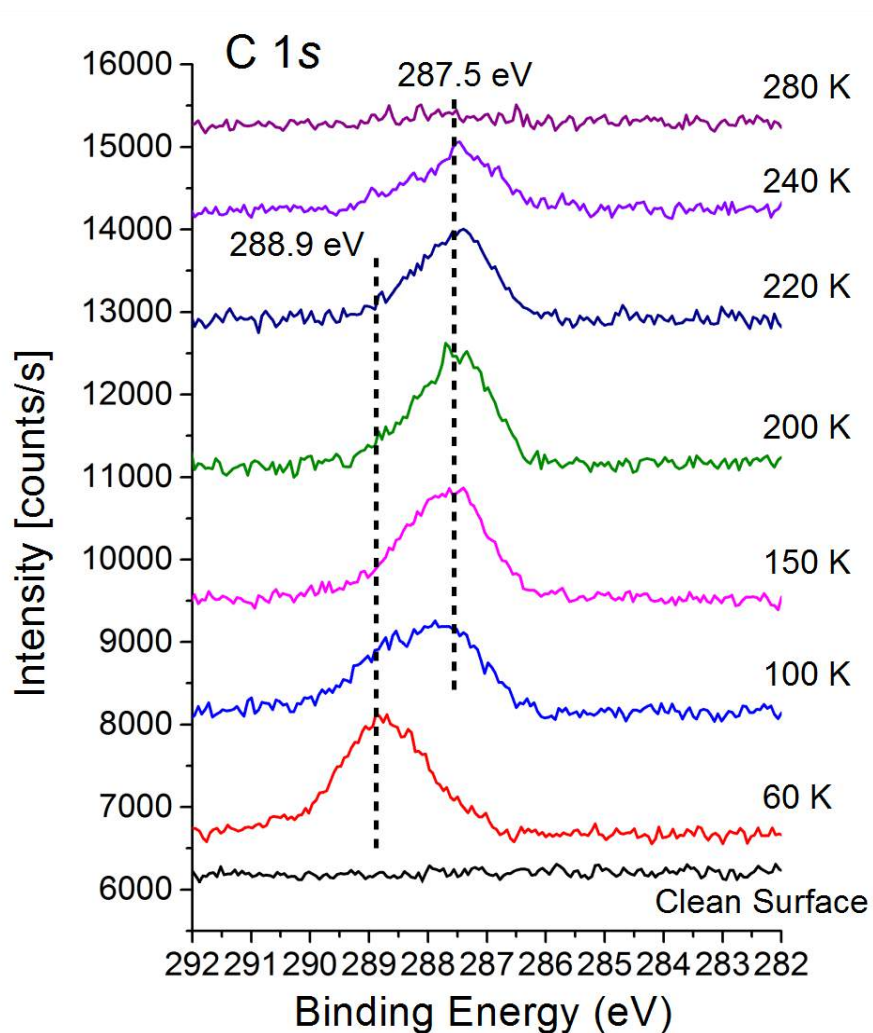


**Figure 7.6.** C 1s XPS spectra from formaldehyde adsorbed on the  $\text{Fe}_3\text{O}_4(001)$  surface at 60 K and annealed as indicated. The data are offset in the y-direction for clarity. The measurements were performed in the Mrs. system using a SPECS FOCUS 500 monochromatic source (Al  $K\alpha$ ) and a SPECS PHOIBOS 150 electron analyzer.

## Chapter 7. The Water Gas Shift Reaction on the $\text{Fe}_3\text{O}_4(001)$ Surface: Related Adsorption Experiments

STM and IR studies on the adsorption of formaldehyde on  $\text{TiO}_2(110)$  surface have shown the thermal conversion of isolated  $\text{CH}_2\text{O}$  monomers (180-182). Here,  $\text{CH}_2\text{O}$  monomers on surface  $\text{Ti}_{5c}$  rows forms paraformaldehyde by annealing at temperatures higher than 70 K. This product results from the polymerization and occurs by coupling  $\text{CH}_2\text{O}$  monomers. At high temperatures, around 250 K, the paraformaldehyde decomposes to form dioxymethylene species via a reaction of  $\text{Ti}_{5c}$ - bound  $\text{CH}_2\text{O}$  with surface O atoms (180-182). A similar processes could be proposed on the  $\text{Fe}_3\text{O}_4(001)$  surface, where the XPS results suggest changes on the configuration of the carbon species on the surface. Further experiments would be necessary to prove this hypothesis.

The position of the peak for the  $\text{CH}_2\text{O}$  and its thermal behavior discount the formaldehyde as an intermediate in the XPS spectrum on  $\text{Fe}_3\text{O}_4(001)$ . We note that no evidence of adsorption on the clean surface or on the pre-hydroxylated surface was observed at room temperature.

Others species as HOCO or HCO could be proposed. Directly characterization of these species as in the case of  $\text{HCOO}^-$ , where  $\text{HCOOH}$  can be used to produce it, is not possible. Thus, theoretical studies appear to be crucial to prove it their presence.

The dissociation of water has been shown as an important step of the WGS reaction for both mechanisms (164, 165, 183). In the regenerative mechanism as described by the equation 8, the dissociation of water to produce OH species plays an important step on the redox process. On the other hand, in the case of associative mechanism the reaction between OH groups from water dissociation with CO (equation 4) is responsible to create intermediates such as HCOO and HOCO.

Here the XPS results of the adsorption of  $\text{H}_2\text{O}$  on the surface (Figure 7.3b) shows how the adsorption of water is crucial to create the carbon intermediate species. We observe that a minimum pressure of water ( $10^{-6}$  mbar) is required to create the

## Chapter 7. The Water Gas Shift Reaction on the Fe<sub>3</sub>O<sub>4</sub>(001) Surface: Related Adsorption Experiments

intermediates, but already a low pressure of CO is enough to give the conditions for the reaction. Indeed in the case of the experiment shown in Figure 7.3b, the background pressure of CO in the chamber was sufficient to produce significant surface C species. The minimum pressure of water appears to be related with the minimum pressure to extensively hydroxylate the surface. In this context, Chambers has shown the presence of a threshold to complete the hydroxylation of the Fe<sub>3</sub>O<sub>4</sub>(001) surface, which appears between 10<sup>-4</sup> to 10<sup>-2</sup> mbar, which coincides with the presence of molecular water species on the surface. Here the interactions between adsorbed water molecules play an important role in the dissociation and the hydroxylation of the surface (149).

Several studies have established that the presence and proportion of certain intermediates, as well as the main mechanism observed, depends of the concentration of the reactants and the temperature of reaction (184). Results which are supporting a regenerative mechanism have shown intermediate ratios between water and CO (1:1) at high temperatures (above 500 K) (185). The associative mechanism, via intermediate formate species, has been observed under low temperatures and at very high ratio of water to CO (36:1) (184). On Rh-doped CeO<sub>2</sub>, it has been shown that, under water rich conditions, the selectivity of formate to CO<sub>2</sub> and H<sub>2</sub> is much higher than the selectivity in vacuum conditions (186). The differences in the concentration of intermediate species observed in our results (compare Figure 7.2 and 7.4) could be related to changes in the experimental conditions.

Magnetite appears as one of the most active water-gas shift catalysts. Several studies have attributed its reactivity to its electronic properties. Due its structure it is expected that a rapid electron exchange takes place between the Fe<sup>2+</sup> and the Fe<sup>3+</sup> cations in the octahedral sites; this property has been related with the regenerative mechanism, where surface cations capable of readily altering their oxidation state are decisive (46, 132). Our observations suggest some reduction of the surface after the co-adsorption experiment (Figure 7.1c) which could be related to the hydroxylation of the surface. Evidence of reduction on the Fe<sub>3</sub>O<sub>4</sub>(001)

## Chapter 7. The Water Gas Shift Reaction on the Fe<sub>3</sub>O<sub>4</sub>(001) Surface: Related Adsorption Experiments

surface by CO exposing at 573 K was not observed even at pressures around 10<sup>-5</sup> mbar (187).

The results presented here cannot discount a possible influence of both mechanisms on the surface. In fact, different studies, for example on gold promoted water gas shift catalysts, have suggested a mechanism which contains both regenerative and associative pathways (184), where the experimental conditions such as temperature play an important role (184, 188). The influence of the regenerative mechanism could be observed on the reduction of the surface as is observed in Figure 7.1c. On the other hand, although formate appears as a species created by the adsorption of H<sub>2</sub>O and CO, our formic acid TPD results (Chapter 6), where no production of H<sub>2</sub> was observed, would mean that this species would act only as a spectator. Nevertheless, the other intermediates observed could play an important role in the WGS reaction on the Fe<sub>3</sub>O<sub>4</sub>(001) surface. Further experiments about the reactivity and theoretical support are necessary to complete the understanding of the reaction.

## Conclusion

The work described in this thesis is a good example of how surface science and its tools can play an important role in understanding the active sites, intermediates and reaction pathways for the adsorption and reaction processes of organic molecules on metal oxides.

The identification of common defects on the  $\text{Fe}_3\text{O}_4(001)-(\sqrt{2}\times\sqrt{2})R45^\circ$  surface was possible using STM. In addition to the defects previously reported, i.e. the anti-phase domain boundaries (74) and surface hydroxyl groups (76), here a new kind of point defect related with Fe atoms incorporated in the subsurface was identified. This defect can be prepared by Fe deposition. The Fe atoms behave similar to other metals such as Ni, Co, Ti and Zr, entering the subsurface, filling one  $\text{Fe}_{\text{oct}}$  vacancy in the third layer of the SCV reconstruction. This induces the interstitial Fe atom related to the reconstruction to move and occupy the other vacancy, locally lifting the reconstruction.

A new interpretation of the Fe-Dimer termination was proposed. The Fe-Dimer surface is formed on the distorted bulk truncation surface. Here it is proposed that the  $(\sqrt{2}\times\sqrt{2})R45^\circ$  reconstruction should be lifted before the formation of the dimer. The Fe-Dimer surface is formed at two Fe atoms per unit cell, exhibiting  $(\sqrt{2}\times\sqrt{2})R45^\circ$  symmetry. The presence of Fe-clusters was related to reaction of the Fe-dimers patches and Fe atoms with oxygen.

On the basis of the STM, XPS and TPD results, we have shown that methanol adsorption is restricted to defect sites on the  $\text{Fe}_3\text{O}_4(001)$  surface at room temperature. This is in contrast to formic acid, which was found to dissociate at regular lattice sites on this surface, resulting in a monolayer of bidentate formate species. That the surface dissociates formic acid suggests that the cation-anion site separation is not prohibitive, but rather the acid-base strength of the surface atoms is insufficient to induce dissociation of weaker acids, such as methanol. On

the basis of the STM data the active sites for methanol dissociation are identified as step edges, Fe adatoms, incorporated Fe defects, and APDBs.

The presence of surface defects affects the reactivity of adsorbed species. In the case of formate, it decomposes to produce CO, H<sub>2</sub>O, CO<sub>2</sub> and H<sub>2</sub>CO, while the adsorption of methoxy species at defects sites promotes a disproportionation reaction to form methanol and formaldehyde.

We demonstrated that the increase of the under-coordinated Fe atoms on the magnetite surface plays an important role on the adsorption of formic acid and methanol. Here the Fe-dimer surface, which exposes two extra octahedral Fe atoms per reconstructed unit cell with respect to the SCV reconstructed surface, showed an increase in the capacity for formic acid dissociation and for the adsorption of methanol related species.

Finally, we have identified the presence of carbon intermediates species under co-adsorption of CO and H<sub>2</sub>O; these species were assigned to carbon in the form of graphite or CH<sub>x</sub> fragments, iron carbides, and formate species. The fourth species appears to be related to HOCO or HCO. Although the conditions of temperature used here does not correspond to the WGS reaction conditions, our observations of carbon species on the surfaces after the co-adsorption of CO and H<sub>2</sub>O suggest the presence of an associative mechanism. Other than that, regenerative mechanisms also could be involved, this idea comes from the observation of the surface reduction. These preliminary results represent an excellent motivation to continue with studies related to the water gas shift reaction on the Fe<sub>3</sub>O<sub>4</sub>(001) surface. In particular, experiments under different parameters of temperature and concentration of reactants, supported by theoretical calculations, are necessary to complete the understanding of the reaction.

# Bibliography

1. Kühn FE (2013) Catalysis. From Principles to Applications. By Matthias Beller, Albert Renken and Rutger A. van Santen. *Angewandte Chemie International Edition* 52(10):2650-2650.
2. Deutschmann O, Knözinger H, Kochloefl K, & Turek T (2000) Heterogeneous Catalysis and Solid Catalysts. *Ullmann's Encyclopedia of Industrial Chemistry*, (Wiley-VCH Verlag GmbH & Co. KGaA).
3. Ertl G (1990) Elementary Steps in Heterogeneous Catalysis. *Angewandte Chemie International Edition in English* 29(11):1219-1227.
4. Oura K, Katayama M, Zotov AV, Lifshits VG, & Saranin AA (2003) Atomic Structure of Surfaces with Adsorbates. *Surface Science: An Introduction*, (Springer Berlin Heidelberg, Berlin, Heidelberg).
5. Vohs JM (2012) Site Requirements for the Adsorption and Reaction of Oxygenates on Metal Oxide Surfaces. *Chemical Reviews* 113(6):4136-4163.
6. Freund HJ (1995) Metal Oxide Surfaces: Electronic Structure and Molecular Adsorption. *physica status solidi (b)* 192(2):407-440.
7. Calatayud M, Markovits A, Menetrey M, Mguig B, & Minot C (2003) Adsorption on perfect and reduced surfaces of metal oxides. *Catalysis Today* 85(2-4):125-143.
8. Curtis Conner Jr W (1993) Spectroscopic insight into spillover. *Studies in Surface Science and Catalysis*, eds T. Inui KFTU & Masai M (Elsevier), Vol Volume 77, pp 61-68.
9. Conner WC & Falconer JL (1995) Spillover in Heterogeneous Catalysis. *Chemical Reviews* 95(3):759-788.
10. Barteau MA (1996) Organic Reactions at Well-Defined Oxide Surfaces. *Chemical Reviews* 96(4):1413-1430.
11. Freund H-J (1997) Adsorption of Gases on Complex Solid Surfaces. *Angewandte Chemie International Edition in English* 36(5):452-475.
12. Zhang K, Shaikhutdinov S, & Freund H-J (2015) Does the Surface Structure of Oxide Affect the Strong Metal-Support Interaction with Platinum? Platinum on  $\text{Fe}_3\text{O}_4(001)$  versus  $\text{Fe}_3\text{O}_4(111)$ . *ChemCatChem* 7(22):3725-3730.
13. Doornkamp C & Ponc V (2000) The universal character of the Mars and Van Krevelen mechanism. *Journal of Molecular Catalysis A: Chemical* 162(1-2):19-32.
14. Peng XD & Barteau MA (1991) Acid-base properties of model magnesium oxide surfaces. *Langmuir* 7(7):1426-1431.
15. Auroux A & Gervasini A (1990) Microcalorimetric study of the acidity and basicity of metal oxide surfaces. *The Journal of Physical Chemistry* 94(16):6371-6379.
16. Metiu H, Chrétien S, Hu Z, Li B, & Sun X (2012) Chemistry of Lewis Acid-Base Pairs on Oxide Surfaces. *The Journal of Physical Chemistry C* 116(19):10439-10450.

17. Bera P & Vohs JM (2007) Reaction of CH<sub>3</sub>OH on Pd/ZnO(0001) and PdZn/ZnO(0001) Model Catalysts. *The Journal of Physical Chemistry C* 111(19):7049-7057.
18. Stone FS, Garrone E, & Zecchina A (1985) A Special Double Issue Containing Papers Presented at the Workshop on Surface Properties of Oxides Surface properties of alkaline earth oxides as studied by UV-visible diffuse reflectance spectroscopy. *Materials Chemistry and Physics* 13(3):331-346.
19. Henderson M, Otero-Tapia S, & Castro M (1999) The chemistry of methanol on the TiO<sub>2</sub>(110) surface: the influence of vacancies and coadsorbed species. *Faraday Discussions* 114(0):313-329.
20. Kim YK, Kay BD, White JM, & Dohnálek Z (2007) Inductive Effect of Alkyl Chains on Alcohol Dehydration at Bridge-bonded Oxygen Vacancies of TiO<sub>2</sub>(110). *Catalysis Letters* 119(1):1-4.
21. Onishi H, Egawa C, Aruga T, & Iwasawa Y (1987) Adsorption of Na atoms and oxygen-containing molecules on MgO(100) and (111) surfaces. *Surface Science* 191(3):479-491.
22. Dulub O, Boatner LA, & Diebold U (2002) STM study of the geometric and electronic structure of ZnO(0 0 0 1)-Zn, (0 0 0 1̄)-O, (1 0 1̄ 0), and (1 1 2̄ 0) surfaces. *Surface Science* 519(3):201-217.
23. Akhter S, Lui K, & Kung HH (1985) Comparison of the chemical properties of the zinc-polar, the oxygen-polar, and the nonpolar surfaces of zinc oxide. *The Journal of Physical Chemistry* 89(10):1958-1964.
24. Vohs JM & Barteau MA (1988) Reaction pathways and intermediates in the decomposition of acetic and propionic acids on the polar surfaces of zinc oxide. *Surface Science* 201(3):481-502.
25. Zhou J & Mullins DR (2006) Adsorption and reaction of formaldehyde on thin-film cerium oxide. *Surface Science* 600(7):1540-1546.
26. Mullins DR, Robbins MD, & Zhou J (2006) Adsorption and reaction of methanol on thin-film cerium oxide. *Surface Science* 600(7):1547-1558.
27. Ferrizz RM, Wong GS, Egami T, & Vohs JM (2001) Structure Sensitivity of the Reaction of Methanol on Ceria. *Langmuir* 17(8):2464-2470.
28. Henderson MA (1997) Complexity in the Decomposition of Formic Acid on the TiO<sub>2</sub>(110) Surface. *The Journal of Physical Chemistry B* 101(2):221-229.
29. Henderson MA (1996) An HREELS and TPD study of water on TiO<sub>2</sub>(110): the extent of molecular versus dissociative adsorption. *Surface Science* 355(1):151-166.
30. Pacchioni G (2003) Oxygen Vacancy: The Invisible Agent on Oxide Surfaces. *ChemPhysChem* 4(10):1041-1047.
31. Duriez C, Chapon C, Henry CR, & Rickard JM (1990) Structural characterization of MgO(100) surfaces. *Surface Science* 230(1):123-136.
32. Ferrari AM & Pacchioni G (1995) Electronic Structure of F and V Centers on the MgO Surface. *The Journal of Physical Chemistry* 99(46):17010-17018.
33. Giamello E, Paganini MC, Murphy DM, Ferrari AM, & Pacchioni G (1997) A Combined EPR and Quantum Chemical Approach to the Structure of Surface F<sub>s</sub><sup>+</sup>(H) Centers on MgO. *The Journal of Physical Chemistry B* 101(6):971-982.



34. Pacchioni G (2000) Ab initio theory of point defects in oxide materials: structure, properties, chemical reactivity. *Solid State Sciences* 2(2):161-179.
35. Bredow T & Pacchioni G (2002) Electronic structure of an isolated oxygen vacancy at the  $\text{TiO}_2(110)$  surface. *Chemical Physics Letters* 355(5-6):417-423.
36. Lu G, Linsebigler A, & Yates JT (1994)  $\text{Ti}^{3+}$  Defect Sites on  $\text{TiO}_2(110)$ : Production and Chemical Detection of Active Sites. *The Journal of Physical Chemistry* 98(45):11733-11738.
37. Blum R, et al. (2014) Subsurface cation vacancy stabilization of the magnetite (001) surface. *Science (New York, N.Y.)* 346(6214):1215-1218.
38. Cornell RM & Schwertmann U (2004) Introduction to the Iron Oxides. *The Iron Oxides*, (Wiley-VCH Verlag GmbH & Co. KGaA), pp 1-7.
39. Somorjai GA & Salmeron M (1986) Surface Properties of Catalysts. *Iron and Its Oxides; Surface Chemistry, Photochemistry And Catalysis. Homogeneous and Heterogeneous Photocatalysis*, eds Pelizzetti E & Serpone N (Springer Netherlands, Dordrecht), pp 445-477.
40. Davis BH (2009) Fischer-Tropsch Synthesis: Reaction mechanisms for iron catalysts. *Catalysis Today* 141(1-2):25-33.
41. Butt JB (1990) Carbide phases on iron-based Fischer-Tropsch synthesis catalysts part I: Characterization studies. *Catalysis Letters* 7(1):61-81.
42. Niemantsverdriet JW, Van der Kraan AM, Van Dijk WL, & Van der Baan HS (1980) Behavior of metallic iron catalysts during Fischer-Tropsch synthesis studied with Moessbauer spectroscopy, x-ray diffraction, carbon content determination, and reaction kinetic measurements. *The Journal of Physical Chemistry* 84(25):3363-3370.
43. Bukur DB, et al. (1995) Activation Studies with a Precipitated Iron Catalyst for Fischer-Tropsch Synthesis. *Journal of Catalysis* 155(2):353-365.
44. Shroff MD, et al. (1995) Activation of Precipitated Iron Fischer-Tropsch Synthesis Catalysts. *Journal of Catalysis* 156(2):185-207.
45. Grenoble DC, Estadt MM, & Ollis DF (1981) The chemistry and catalysis of the water gas shift reaction: 1. The kinetics over supported metal catalysts. *Journal of Catalysis* 67(1):90-102.
46. Lund Carl R F, Kubsh Joseph E, & Dumesic J A (1985) Water Gas Shift over Magnetite-Based Catalysts. *Solid State Chemistry in Catalysis*, ACS Symposium Series, (American Chemical Society), Vol 279, pp 313-338.
47. Rhodes C, Hutchings GJ, & Ward AM (1995) Water-gas shift reaction: finding the mechanistic boundary. *Catalysis Today* 23(1):43-58.
48. dos Santos Coelho F, et al. (2008) Potential application of highly reactive  $\text{Fe}(0)/\text{Fe}_3\text{O}_4$  composites for the reduction of Cr(VI) environmental contaminants. *Chemosphere* 71(1):90-96.
49. Li S, Krishnamoorthy S, Li A, Meitzner GD, & Iglesia E (2002) Promoted Iron-Based Catalysts for the Fischer-Tropsch Synthesis: Design, Synthesis, Site Densities, and Catalytic Properties. *Journal of Catalysis* 206(2):202-217.
50. Novotný Z, et al. (2012) Ordered Array of Single Adatoms with Remarkable Thermal Stability:  $\text{Au}/\text{Fe}_3\text{O}_4(001)$ . *Physical Review Letters* 108(21):216103.

51. Parkinson GS, et al. (2013) Carbon monoxide-induced adatom sintering in a Pd-Fe<sub>3</sub>O<sub>4</sub> model catalyst. *Nat Mater* 12(8):724-728.
52. Fadley CS (2010) X-ray photoelectron spectroscopy: Progress and perspectives. *Journal of Electron Spectroscopy and Related Phenomena* 178-179:2-32.
53. Einstein A (1905) Über einen die Erzeugung und Verwandlung des Lichtes betreffenden heuristischen Gesichtspunkt. *Annalen der Physik* 322(6):132-148.
54. Somorjai G (1994) *Introduction to Surface Chemistry and Catalysis* (John Wiley & Sons, New York).
55. Rakić V & Damjanović L (2013) Temperature-Programmed Desorption (TPD) Methods. *Calorimetry and Thermal Methods in Catalysis*, ed Auroux A (Springer Berlin Heidelberg, Berlin, Heidelberg), pp 131-174.
56. Redhead P.A (1962) Thermal Desorption of Gases. *Vacuum* 12(4) 203-211.
57. Binnig G & Rohrer H (1983) Scanning tunneling microscopy. *Surface Science* 126(1):236-244.
58. Binnig G, Rohrer H, Gerber C, & Weibel E (1982) Tunneling through a controllable vacuum gap. *Applied Physics Letters* 40(2):178-180.
59. Hollins P (2006) Infrared Reflection–Absorption Spectroscopy. *Encyclopedia of Analytical Chemistry*, (John Wiley & Sons, Ltd).
60. Hoffmann FM (1983) Infrared reflection-absorption spectroscopy of adsorbed molecules. *Surface Science Reports* 3(2–3):107-192.
61. Halwidl D (2016) Development of an Effusive Molecular Beam Apparatus (Springer Spektrum).
62. de la Figuera J, et al. (2013) Real-space imaging of the Verwey transition at the (100) surface of magnetite. *Physical Review B* 88(16):161410.
63. Joaquín G & Gloria S (2004) The Verwey transition—a new perspective. *Journal of Physics: Condensed Matter* 16(7):R145.
64. Friedrich W (2002) The Verwey transition - a topical review. *Journal of Physics: Condensed Matter* 14(12):R285.
65. Fubini B, Mollo L, & Giamello E (1995) Free Radical Generation at the Solid/Liquid Interface in Iron Containing Minerals. *Free Radical Research* 23(6):593-614.
66. Huang L, Han B, Zhang Q, Fan M, & Cheng H (2015) Mechanistic Study on Water Gas Shift Reaction on the Fe<sub>3</sub>O<sub>4</sub>(111) Reconstructed Surface. *The Journal of Physical Chemistry C* 119(52):28934-28945.
67. Tasker PW (1979) The stability of ionic crystal surfaces. *Journal of Physics C: Solid State Physics* 12(22):4977.
68. Claudine N (2000) Polar oxide surfaces. *Journal of Physics: Condensed Matter* 12(31):R367.
69. Stanka B, Hebenstreit W, Diebold U, & Chambers SA (2000) Surface reconstruction of Fe<sub>3</sub>O<sub>4</sub>(001). *Surface Science* 448(1):49-63.
70. Rustad JR, Wasserman E, & Felmy AR (1999) A molecular dynamics investigation of surface reconstruction on magnetite (001). *Surface Science* 432(1–2):L583-L588.
71. Pentcheva R, et al. (2005) Jahn-Teller Stabilization of a "Polar" Metal Oxide Surface:Fe<sub>3</sub>O<sub>4</sub>(001). *Physical Review Letters* 94(12):126101.

72. Pentcheva R, et al. (2008) A combined DFT/LEED-approach for complex oxide surface structure determination:  $\text{Fe}_3\text{O}_4(001)$ . *Surface Science* 602(7):1299-1305.
73. Wang H-Q, Altman EI, & Henrich VE (2006) Steps on  $\text{Fe}_3\text{O}_4(100)$ : STM measurements and theoretical calculations. *Physical Review B* 73(23):235418.
74. Parkinson GS, et al. (2012) Antiphase domain boundaries at the  $\text{Fe}_3\text{O}_4(001)$  surface. *Physical Review B* 85(19).
75. Bartelt NC, et al. (2013) Order-disorder phase transition on the (100) surface of magnetite. *Physical Review B* 88(23):235436.
76. Parkinson GS, et al. (2010) Semiconductor-half metal transition at the  $\text{Fe}_3\text{O}_4(001)$  surface upon hydrogen adsorption. *Physical Review B* 82(12):125413.
77. Parkinson GS, Novotny Z, Jacobson P, Schmid M, & Diebold U (2011) Room temperature water splitting at the surface of magnetite. *Journal of the American Chemical Society* 133(32):12650-12655.
78. Novotny Z, et al. (2013) Probing the surface phase diagram of  $\text{Fe}_3\text{O}_4(001)$  towards the Fe-rich limit: Evidence for progressive reduction of the surface. *Physical Review B* 87(19):195410.
79. Bliem R, et al. (2014) Cluster Nucleation and Growth from a Highly Supersaturated Adatom Phase: Silver on Magnetite. *ACS Nano* 8(7):7531-7537.
80. Bliem R, et al. (2015) Adsorption and incorporation of transition metals at the magnetite  $\text{Fe}_3\text{O}_4(001)$  surface. *Physical Review B* 92(7):075440.
81. Parkinson GS, Novotný Z, Jacobson P, Schmid M, & Diebold U (2011) A metastable Fe(A) termination at the  $\text{Fe}_3\text{O}_4(001)$  surface. *Surface Science* 605(15-16):L42-L45.
82. Tarrach G, Bürgler D, Schaub T, Wiesendanger R, & Güntherodt HJ (1993) Atomic surface structure of  $\text{Fe}_3\text{O}_4(001)$  in different preparation stages studied by scanning tunneling microscopy. *Surface Science* 285(1):1-14.
83. Gaines JM, et al. (1997) An STM study of  $\text{Fe}_3\text{O}_4(100)$  grown by molecular beam epitaxy. *Surface Science* 373(1):85-94.
84. Gaines JM, et al. (1997) The (001) Surface of  $\text{Fe}_3\text{O}_4$  Grown Epitaxially on MgO and Characterized by Scanning Tunneling Microscopy. *MRS Online Proceedings Library Archive* 474:null-null.
85. Spiridis N, Barbasz J, Łodziana Z, & Korecki J (2006)  $\text{Fe}_3\text{O}_4(001)$  films on Fe(001): Termination and reconstruction of iron-rich surfaces. *Physical Review B* 74(15):155423.
86. Spiridis N, et al. (2004) Surface Structure of Epitaxial Magnetite  $\text{Fe}_3\text{O}_4(001)$  Films: In Situ STM and CEMS Studies. *The Journal of Physical Chemistry B* 108(38):14356-14361.
87. Taguchi M, et al. (2015) Temperature Dependence of Magnetically Active Charge Excitations in Magnetite across the Verwey Transition. *Physical Review Letters* 115(25):256405.
88. Parkinson GS (2016) Iron oxide surfaces. *Surface Science Reports* 71(1):272-365.

89. Palo DR, Dagle RA, & Holladay JD (2007) Methanol Steam Reforming for Hydrogen Production. *Chemical Reviews* 107(10):3992-4021.
90. Sá S, Silva H, Brandão L, Sousa JM, & Mendes A (2010) Catalysts for methanol steam reforming—A review. *Applied Catalysis B: Environmental* 99(1–2):43-57.
91. Badlani M & Wachs IE (2001) Methanol: A “Smart” Chemical Probe Molecule. *Catalysis Letters* 75(3):137-149.
92. Perrot E, et al. (1994) Atomic-Scale Resolution on the MgO(100) Surface by Scanning Force and Friction Microscopy. *EPL (Europhysics Letters)* 26(9):659.
93. Wu MC, Truong CM, & Goodman DW (1993) Interactions of alcohols with a nickel oxide(100) surface studied by high-resolution electron energy loss spectroscopy and temperature-programmed desorption spectroscopy. *The Journal of Physical Chemistry* 97(37):9425-9433.
94. Herman GS, Dohnálek Z, Ruzycki N, & Diebold U (2003) Experimental Investigation of the Interaction of Water and Methanol with Anatase-TiO<sub>2</sub>(101). *The Journal of Physical Chemistry B* 107(12):2788-2795.
95. Onda K, Li B, Zhao J, & Petek H (2005) The electronic structure of methanol covered TiO<sub>2</sub>(110) surfaces. *Surface Science* 593(1–3):32-37.
96. Zhang Z, Bondarchuk O, White JM, Kay BD, & Dohnálek Z (2006) Imaging Adsorbate O–H Bond Cleavage: Methanol on TiO<sub>2</sub>(110). *Journal of the American Chemical Society* 128(13):4198-4199.
97. Farfan-Arribas E & Madix RJ (2003) Different binding sites for methanol dehydrogenation and deoxygenation on stoichiometric and defective TiO<sub>2</sub>(110) surfaces. *Surface Science* 544(2–3):241-260.
98. Yoshimichi N, Ken-ichi F, & Yasuhiro I (2004) The dynamic behaviour of CH<sub>3</sub>OH and NO<sub>2</sub> adsorbed on CeO<sub>2</sub>(111) studied by noncontact atomic force microscopy. *Nanotechnology* 15(2):S49.
99. Rim KT, et al. (2012) Scanning Tunneling Microscopy and Theoretical Study of Water Adsorption on Fe<sub>3</sub>O<sub>4</sub>: Implications for Catalysis. *Journal of the American Chemical Society* 134(46):18979-18985.
100. Grant AW, et al. (2001) Methanol Decomposition on Pt/ZnO(0001)–Zn Model Catalysts. *The Journal of Physical Chemistry B* 105(38):9273-9279.
101. Li Z, et al. (2015) Reactions of Deuterated Methanol (CD<sub>3</sub>OD) on Fe<sub>3</sub>O<sub>4</sub>(111). *The Journal of Physical Chemistry C* 119(2):1113-1120.
102. Matolín V, et al. (2009) Methanol adsorption on a CeO<sub>2</sub>(111)/Cu(111) thin film model catalyst. *Surface Science* 603(8):1087-1092.
103. Vohs JM & Barteau MA (1986) Conversion of methanol, formaldehyde and formic acid on the polar faces of zinc oxide. *Surface Science* 176(1–2):91-114.
104. Kim KS & Barteau MA (1989) Reactions of methanol on TiO<sub>2</sub>(001) single crystal surfaces. *Surface Science* 223(1–2):13-32.
105. Peng XD & Barteau MA (1989) Spectroscopic characterization of surface species derived from HCOOH, CH<sub>3</sub>COOH, CH<sub>3</sub>OH, C<sub>2</sub>H<sub>5</sub>OH, HCOOCH<sub>3</sub>, and C<sub>2</sub>H<sub>2</sub> on MgO thin film surfaces. *Surface Science* 224(1–3):327-347.

106. Wu MC, Estrada CA, Corneille JS, & Goodman DW (1992) Model surface studies of metal oxides: Adsorption of water and methanol on ultrathin MgO films on Mo(100). *The Journal of Chemical Physics* 96(5):3892-3900.
107. Mensch MW, Byrd CM, & Cox DF (2003) Reaction of methanol on stoichiometric and O-terminated  $\alpha$ -Cr<sub>2</sub>O<sub>3</sub> (1 0  $\bar{1}$  2): interconversion of oxygenated C1 surface intermediates. *Catalysis Today* 85(2–4):279-289.
108. Henrich VE & Shaikhutdinov SK (2005) Atomic geometry of steps on metal-oxide single crystals. *Surface Science* 574(2–3):306-316.
109. Gong X-Q, Selloni A, Batzill M, & Diebold U (2006) Steps on anatase TiO<sub>2</sub>(101). *Nat Mater* 5(8):665-670.
110. Davis EM, et al. (2015) Growth of Fe<sub>3</sub>O<sub>4</sub>(001) thin films on Pt(100): Tuning surface termination with an Fe buffer layer. *Surface Science* 636:42-46.
111. Mulakaluri N & Pentcheva R (2012) Hydrogen Adsorption and Site-Selective Reduction of the Fe<sub>3</sub>O<sub>4</sub>(001) Surface: Insights From First Principles. *The Journal of Physical Chemistry C* 116(31):16447-16453.
112. Łodziana Z (2007) Surface Verwey Transition in Magnetite. *Physical Review Letters* 99(20):206402.
113. Feng T & Vohs JM (2004) A TPD study of the partial oxidation of methanol to formaldehyde on CeO<sub>2</sub>-supported vanadium oxide. *Journal of Catalysis* 221(2):619-629.
114. Gorte RJ & Zhao S (2005) Studies of the water-gas-shift reaction with ceria-supported precious metals. *Catalysis Today* 104(1):18-24.
115. Senanayake SD, et al. (2010) Probing the reaction intermediates for the water–gas shift over inverse CeO<sub>x</sub>/Au(111) catalysts. *Journal of Catalysis* 271(2):392-400.
116. Pang CL, Lindsay R, & Thornton G (2013) Structure of Clean and Adsorbate-Covered Single-Crystal Rutile TiO<sub>2</sub> Surfaces. *Chemical Reviews* 113(6):3887-3948.
117. Peng XD & Barteau MA (1990) Dehydration of carboxylic acids on the MgO(100) surface. *Catalysis Letters* 7(5-6):395-402.
118. Xu C & Goodman DW (1995) Surface chemistry of polar oxide surfaces: formic acid on NiO(111). *Journal of the Chemical Society, Faraday Transactions* 91(20):3709-3715.
119. Senanayake SD & Mullins DR (2008) Redox Pathways for HCOOH Decomposition over CeO<sub>2</sub> Surfaces. *The Journal of Physical Chemistry C* 112(26):9744-9752.
120. Xu M, et al. (2012) Dissociation of formic acid on anatase TiO<sub>2</sub>(101) probed by vibrational spectroscopy. *Catalysis Today* 182(1):12-15.
121. Buchholz M, et al. (2015) The Interaction of Formic Acid with Zinc Oxide: A Combined Experimental and Theoretical Study on Single Crystal and Powder Samples. *Topics in Catalysis* 58(2):174-183.
122. Gercher VA & Cox DF (1994) Formic acid decomposition on SnO<sub>2</sub>(110). *Surface Science* 312(1–2):106-114.
123. Baber AE, et al. (2013) Assisted deprotonation of formic acid on Cu(111) and self-assembly of 1D chains. *Physical Chemistry Chemical Physics* 15(29):12291-12298.

124. Iwasawa Y, Onishi H, Fukui K-i, Suzuki S, & Sasaki T (1999) The selective adsorption and kinetic behaviour of molecules on TiO<sub>2</sub>(110) observed by STM and NC-AFM. *Faraday Discussions* 114(0):259-266.
125. Cutting RS, Muryn CA, Thornton G, & Vaughan DJ (2006) Molecular scale investigations of the reactivity of magnetite with formic acid, pyridine, and carbon tetrachloride. *Geochimica et Cosmochimica Acta* 70(14):3593-3612.
126. Tanner RE, Sasahara A, Liang Y, Altman EI, & Onishi H (2002) Formic Acid Adsorption on Anatase TiO<sub>2</sub>(001)-(1×4) Thin Films Studied by NC-AFM and STM†. *The Journal of Physical Chemistry B* 106(33):8211-8222.
127. Zachariasen WH (1940) The Crystal Structure of Sodium Formate, NaHCO<sub>2</sub>. *Journal of the American Chemical Society* 62(5):1011-1013.
128. Onishi H & Iwasawa Y (1994) STM-imaging of formate intermediates adsorbed on a TiO<sub>2</sub>(110) surface. *Chemical Physics Letters* 226(1-2):111-114.
129. Petrie WT & Vohs JM (1991) An HREELS investigation of the adsorption and reaction of formic acid on the (0001)-Zn surface of ZnO. *Surface Science* 245(3):315-323.
130. Ai M (1977) Activities for the decomposition of formic acid and the acid-base properties of metal oxide catalysts. *Journal of Catalysis* 50(2):291-300.
131. Rethwisch DG & Dumesic JA (1986) Effect of metal-oxygen bond strength on properties of oxides. 1. Infrared spectroscopy of adsorbed carbon monoxide and carbon dioxide. *Langmuir* 2(1):73-79.
132. Rethwisch DG & Dumesic JA (1986) The effects of metal-oxygen bond strength on properties of oxides: II. Water-gas shift over bulk oxides. *Applied Catalysis* 21(1):97-109.
133. Trillo JM, Munuera G, & Criado JM (1972) Catalytic Decomposition of Formic Acid on Metal Oxides. *Catalysis Reviews* 7(1):51-86.
134. Lykhach Y, et al. (2013) Adsorption and Decomposition of Formic Acid on Model Ceria and Pt/Ceria Catalysts. *The Journal of Physical Chemistry C* 117(24):12483-12494.
135. Kim KS & Barteau MA (1990) Structural dependence of the selectivity of formic acid decomposition on faceted titania (001) surfaces. *Langmuir* 6(9):1485-1488.
136. Wulser KW & Langell MA (1992) Carboxylic acid adsorption on NiO(100) characterized by X-ray photoelectron and high resolution electron energy loss spectroscopies. *Catalysis Letters* 15(1-2):39-50.
137. Wang LQ, Ferris KF, Shultz AN, Baer DR, & Engelhard MH (1997) Interactions of HCOOH with stoichiometric and defective TiO<sub>2</sub>(110) surfaces. *Surface Science* 380(2-3):352-364.
138. Noei H, et al. (2013) Vibrational spectroscopic studies on pure and metal-covered metal oxide surfaces. *physica status solidi (b)* 250(6):1204-1221.
139. Hayden BE, King A, & Newton MA (1998) Fourier Transform Reflection-Absorption IR Spectroscopy Study of Formate Adsorption on TiO<sub>2</sub>(110). *The Journal of Physical Chemistry B* 103(1):203-208.
140. Crook S, Dhariwal H, & Thornton G (1997) HREELS study of the interaction of formic acid with ZnO(1010) and ZnO(0001)-O. *Surface Science* 382(1-3):19-25.

141. Nakatsuji H, Yoshimoto M, Umemura Y, Takagi S, & Hada M (1996) Theoretical Study of the Chemisorption and Surface Reaction of HCOOH on a ZnO(1010) Surface. *The Journal of Physical Chemistry* 100(2):694-700.
142. Xu M, et al. (2012) The Surface Science Approach for Understanding Reactions on Oxide Powders: The Importance of IR Spectroscopy. *Angewandte Chemie International Edition* 51(19):4731-4734.
143. Tobin RG (1992) Asymmetric lines and background shifts in reflection-absorption infrared spectroscopy. *Physical Review B* 45(20):12110-12113.
144. Msl'shukov AG (1991) The infrared absorption line shape of molecules adsorbed on a metal surface. *Solid State Communications* 79(1):81-83.
145. Gamba O, et al. (2015) Adsorption of Formic Acid on the Fe<sub>3</sub>O<sub>4</sub>(001) Surface. *The Journal of Physical Chemistry C* 119(35):20459-20465.
146. Truong CM, Wu MC, & Goodman DW (1992) Adsorption and reaction of formic acid on NiO(100) films on Mo(100): Temperature programmed desorption and high resolution electron energy loss spectroscopy studies. *The Journal of Chemical Physics* 97(12):9447-9453.
147. Uetsuka H, Henderson MA, Sasahara A, & Onishi H (2004) Formate Adsorption on the (111) Surface of Rutile TiO<sub>2</sub>. *The Journal of Physical Chemistry B* 108(36):13706-13710.
148. Sayago DI, et al. (2004) Structure Determination of Formic Acid Reaction Products on TiO<sub>2</sub>(110). *The Journal of Physical Chemistry B* 108(38):14316-14323.
149. Kendelewicz T, et al. (2013) X-ray Photoemission and Density Functional Theory Study of the Interaction of Water Vapor with the Fe<sub>3</sub>O<sub>4</sub>(001) Surface at Near-Ambient Conditions. *The Journal of Physical Chemistry C* 117(6):2719-2733.
150. Mulakaluri N, Pentcheva R, Wieland M, Moritz W, & Scheffler M (2009) Partial Dissociation of Water on Fe<sub>3</sub>O<sub>4</sub>(001): Adsorbate Induced Charge and Orbital Order. *Physical Review Letters* 103(17):176102.
151. Dilara PA & Vohs JM (1993) TPD and HREELS investigation of the reaction of formic acid on zirconium dioxide(100). *The Journal of Physical Chemistry* 97(49):12919-12923.
152. Henderson MA (1995) Formic Acid Decomposition on the {110}-Microfaceted Surface of TiO<sub>2</sub>(100): Insights Derived from 18O-Labeling Studies. *The Journal of Physical Chemistry* 99(41):15253-15261.
153. Kim KS & Barteau MA (1988) Pathways for carboxylic acid decomposition on titania. *Langmuir* 4(4):945-953.
154. Smith RJB, Loganathan M, & Shantha Murthy S (2010) A Review of the Water Gas Shift Reaction Kinetics. in *International Journal of Chemical Reactor Engineering*.
155. Ladebeck JR & Wagner JP (2010) Catalyst development for water–gas shift. *Handbook of Fuel Cells*, (John Wiley & Sons, Ltd).
156. Bukur DB, Todic B, & Elbashir N (2016) Role of water-gas-shift reaction in Fischer–Tropsch synthesis on iron catalysts: A review. *Catalysis Today* 275:66-75.
157. Ratnasamy C & Wagner JP (2009) Water Gas Shift Catalysis. *Catalysis Reviews* 51(3):325-440.

158. Gokhale AA, Dumesic JA, & Mavrikakis M (2008) On the Mechanism of Low-Temperature Water Gas Shift Reaction on Copper. *Journal of the American Chemical Society* 130(4):1402-1414.
159. Kowalik P, Próchniak W, & Borowiecki T (2011) The effect of alkali metals doping on properties of Cu/ZnO/Al<sub>2</sub>O<sub>3</sub> catalyst for water gas shift. *Catalysis Today* 176(1):144-148.
160. Shishido T, et al. (2006) Water-gas shift reaction over Cu/ZnO and Cu/ZnO/Al<sub>2</sub>O<sub>3</sub> catalysts prepared by homogeneous precipitation. *Applied Catalysis A: General* 303(1):62-71.
161. Chuasiripattana K, Warschkow O, Delley B, & Stampfl C (2010) Reaction intermediates of methanol synthesis and the water–gas-shift reaction on the ZnO(0001) surface. *Surface Science* 604(19–20):1742-1751.
162. Tang Q-L, Chen Z-X, & He X (2009) A theoretical study of the water gas shift reaction mechanism on Cu(111) model system. *Surface Science* 603(13):2138-2144.
163. Mohsenzadeh A, Richards T, & Bolton K (2016) DFT study of the water gas shift reaction on Ni(111), Ni(100) and Ni(110) surfaces. *Surface Science* 644:53-63.
164. Mudiyansele K, et al. (2013) Importance of the Metal–Oxide Interface in Catalysis: In Situ Studies of the Water–Gas Shift Reaction by Ambient-Pressure X-ray Photoelectron Spectroscopy. *Angewandte Chemie International Edition* 52(19):5101-5105.
165. Senanayake SD, et al. (2010) Probing the reaction intermediates for the water–gas shift over inverse CeO<sub>x</sub>/Au(111) catalysts. *Journal of Catalysis* 271(2):392-400.
166. Tibiletti D, et al. (2006) An investigation of possible mechanisms for the water–gas shift reaction over a ZrO<sub>2</sub>-supported Pt catalyst. *Journal of Catalysis* 244(2):183-191.
167. Rhodes C, Hutchings GJ, & Ward AM (1995) Recent Advances in C1 Chemistry Water-gas shift reaction: finding the mechanistic boundary. *Catalysis Today* 23(1):43-58.
168. Armstrong EF & Hilditch TP (1920) A Study of Catalytic Actions at Solid Surfaces. IV. The Interaction of Carbon Monoxide and Steam as Conditioned by Iron Oxide and by Copper. *Proceedings of the Royal Society of London. Series A* 97(684):265-273.
169. Tabatabaei J, Sakakini BH, & Waugh KC (2006) On the mechanism of methanol synthesis and the water-gas shift reaction on ZnO. *Catalysis Letters* 110(1):77-84.
170. Grabow LC, Gokhale AA, Evans ST, Dumesic JA, & Mavrikakis M (2008) Mechanism of the Water Gas Shift Reaction on Pt: First Principles, Experiments, and Microkinetic Modeling. *The Journal of Physical Chemistry C* 112(12):4608-4617.
171. Natesakhawat S, Wang X, Zhang L, & Ozkan US (2006) Development of chromium-free iron-based catalysts for high-temperature water-gas shift reaction. *Journal of Molecular Catalysis A: Chemical* 260(1–2):82-94.



172. Oki S & Mezaki R (1973) Identification of rate-controlling steps for the water-gas shift reaction over an iron oxide catalyst. *The Journal of Physical Chemistry* 77(4):447-452.
173. Diagne C, Vos PJ, Kiennemann A, Perrez MJ, & Portela MF (1990) Water-gas shift reaction over chromia-promoted magnetite. Use of temperature-programmed desorption and chemical trapping in the study of the reaction mechanism. *Reaction Kinetics and Catalysis Letters* 42(1):25-31.
174. Deng X, et al. (2008) Surface Chemistry of Cu in the Presence of CO<sub>2</sub> and H<sub>2</sub>O. *Langmuir* 24(17):9474-9478.
175. Miller DJ, Biesinger MC, & McIntyre NS (2002) Interactions of CO<sub>2</sub> and CO at fractional atmosphere pressures with iron and iron oxide surfaces: one possible mechanism for surface contamination? *Surface and Interface Analysis* 33(4):299-305.
176. Bhargava G, Gouzman I, Chun CM, Ramanarayanan TA, & Bernasek SL (2007) Characterization of the "native" surface thin film on pure polycrystalline iron: A high resolution XPS and TEM study. *Applied Surface Science* 253(9):4322-4329.
177. Park E, Ostrovski O, Zhang J, Thomson S, & Howe R (2001) Characterization of phases formed in the iron carbide process by X-ray diffraction, mossbauer, X-ray photoelectron spectroscopy, and raman spectroscopy analyses. *Metallurgical and Materials Transactions B* 32(5):839-845.
178. Wiltner A & Linsmeier C (2004) Formation of endothermic carbides on iron and nickel. *physica status solidi (a)* 201(5):881-887.
179. Rodriguez JA, Hanson JC, Stacchiola D, & Senanayake SD (2013) In situ/operando studies for the production of hydrogen through the water-gas shift on metal oxide catalysts. *Physical Chemistry Chemical Physics* 15(29):12004-12025.
180. Yu X, et al. (2016) Interaction of Formaldehyde with the Rutile TiO<sub>2</sub>(110) Surface: A Combined Experimental and Theoretical Study. *The Journal of Physical Chemistry C* 120(23):12626-12636.
181. Zhu K, et al. (2015) Low-Temperature Reductive Coupling of Formaldehyde on Rutile TiO<sub>2</sub>(110). *The Journal of Physical Chemistry C* 119(32):18452-18457.
182. Yuan Q, Wu Z, Jin Y, Xiong F, & Huang W (2014) Surface Chemistry of Formaldehyde on Rutile TiO<sub>2</sub>(110) Surface: Photocatalysis vs Thermal-Catalysis. *The Journal of Physical Chemistry C* 118(35):20420-20428.
183. Graf PO, de Vlieger DJM, Mojet BL, & Lefferts L (2009) New insights in reactivity of hydroxyl groups in water gas shift reaction on Pt/ZrO<sub>2</sub>. *Journal of Catalysis* 262(2):181-187.
184. Burch R (2006) Gold catalysts for pure hydrogen production in the water-gas shift reaction: activity, structure and reaction mechanism. *Physical Chemistry Chemical Physics* 8(47):5483-5500.
185. Hilaire S, Wang X, Luo T, Gorte RJ, & Wagner J (2001) A comparative study of water-gas-shift reaction over ceria supported metallic catalysts. *Applied Catalysis A: General* 215(1-2):271-278.

## Bibliography

186. Shido T & Iwasawa Y (1993) Reactant-Promoted Reaction Mechanism for Water-Gas Shift Reaction on Rh-Doped CeO<sub>2</sub>. *Journal of Catalysis* 141(1):71-81.
187. Bliem R, et al. (2015) An Atomic-Scale View of CO and H<sub>2</sub> Oxidation on a Pt/Fe<sub>3</sub>O<sub>4</sub> Model Catalyst. *Angewandte Chemie International Edition* 54(47):13999-14002.
188. Burch R, Goguet A, & Meunier FC (2011) A critical analysis of the experimental evidence for and against a formate mechanism for high activity water-gas shift catalysts. *Applied Catalysis A: General* 409–410:3-12.

# Curriculum Vitae

## IDENTIFICATION

**NAME**

Oscar Alberto

**DATE OF BIRTH**

08/01/1985

**PASSPORT**

C.C 80796211

**LAST NAME**

Gamba Vasquez

**NATIONALITY**

Colombian

**ADDRESS**

Josef-Baumann-Gasse 8a (402)-1220  
Wien

**PHONE NUMBER - eMAIL**

(+43) 6648673594 - oagambav@gmail.com

## COMMUNICATIVE SKILLS

Spanish (maternal language)

English (Fluent)

## ACADEMIC FORMATION

Bachelor in Chemistry, National University of Colombia, Bogotá, 2008.

Master in Chemistry. National University of Colombia, Bogotá, 2010.

Doctoral Programme in Natural Sciences. Vienna University of Technology, Vienna, 2016

## ACADEMIC AWARDS

Scholarship for graduate student, Faculty of Natural Sciences, National University of Colombia, 2009.

Funding Master's Thesis, Faculty of Natural Sciences, National University of Colombia, 2009.

Scholarship in the Doctoral school Solids4fun, Vienna University of Technology, 2012.

## PROFESSIONAL EXPERIENCE

Teaching Assistant, Chemistry Department, National University of Colombia, 2009-2010

Lecturer-Researcher, Chemistry Department, University of Amazonia, 2010-2012.

## RESEARCH EXPERIENCE

Co-researcher, "Synthesis of pillared clays with Al-Fe and Al-Ce-Fe solid polymer assisted by ultrasound". Solid State and Environmental Catalysis Group. National University of Colombia. 2009-2010.

Co-researcher, "Evaluation of the lipase activity of enzyme extracts of microorganisms present in the region of Florencia-Caquetá". University of Amazonia, 2011.

Co-researcher, "Surface research of magnetite". Vienna University of Technology, Institute of Applied Physics. Surface Physics group. 2012- currently

## PUBLICATIONS

O. Gamba, S. Moreno, R. Molina. **Catalytic performance of Ni-Pr supported on delaminated clay in the dry reforming of methane**. In: I. J. of Hydrogen Energy, 36, (2011), 1540.

C. Daza, O. Gamba, Y. Hernandez, M. Centeno, F. Mondragón, S. Moreno, R. Molina. **High-Stable Mesoporous Ni-Ce/ Clay catalysts for Syngas production**. In: Catal. Lett, 141, (2011), 1037.

R. Bliem, R. Kosak, L. Perneczky, Z. Novotny, O. Gamba, D. Fobes, Z. Mao, M. Schmid, P. Blaha, U. Diebold, G. S. Parkinson. **Cluster nucleation and growth from a highly supersaturated adatom phase: silver on magnetite**. In: ACS Nano, 8, (2014), 7531.

R. Bliem, E. McDermott, P. Ferstl, M. Setvin, O. Gamba, J. Pavelec, M. A. Schneider, M. Schmid, U. Diebold, P. Blaha, L. Hammer, G. S. Parkinson. **Subsurface cation vacancy stabilization of the magnetite (001) surface**. In: Science, 346, (2014), 1215.

R. Bliem, J. Pavelec, O. Gamba, E. McDermott, Z. Wang, S. Gerhold, M. Wagner, J. Osiecki, K. Schulte, M. Schmid, P. Blaha, U. Diebold, G. S. Parkinson. **Adsorption and incorporation of transition metals at the magnetite  $\text{Fe}_3\text{O}_4(001)$  surface**. In: Phys. Rev. B, 92, (2015), 075440.

O. Gamba, H. Noei, J. Pavelec, R. Bliem, M. Schmid, U. Diebold, A. Stierle, G. S. Parkinson. **Adsorption of formic acid on the  $\text{Fe}_3\text{O}_4(001)$  surface**. In: J. Phys. Chem. C, 119, (2015), 20459.

R. Bliem, J. van der Hoeven, A. Zavodny, O. Gamba, J. Pavelec, P. de Jongh, M. Schmid, U. Diebold, G. S. Parkinson. **An atomic-scale view of CO and  $\text{H}_2$  oxidation on a Pt/ $\text{Fe}_3\text{O}_4$  model catalyst**. In: Angew. Chem. Int. Ed, 54, (2015) 13999.

G. S. Parkinson, P. Lackner, O. Gamba, S. Maaß, S. Gerhold, M. Riva, R. Bliem, U. Diebold, M. Schmid.  **$\text{Fe}_3\text{O}_4(110)-(1 \times 3)$  revisited: Periodic (111) nanofacets**. In: Surf. Sci, 649 (2016) 120.

B. Arndt, R. Bliem, O. Gamba, J. van der Hoeven, H. Noei, U. Diebold, G. S. Parkinson, A. Stierle. **Atomic structure and stability of magnetite  $\text{Fe}_3\text{O}_4(001)$ : An X-ray view**. In: Surf. Sci, 653, (2016) 76.

R. Bliem, J. van der Hoeven, J. Hulva, J. Pavelec, O. Gamba, P. de Jongh, M. Schmid, P. Blaha, U. Diebold, G. S. Parkinson. **Dual role of CO in the stability of subnano Pt clusters at the Fe<sub>3</sub>O<sub>4</sub> (001) surface.** In: PNAS, (2016) 1.

O. Gamba, J. Hulva, J. Pavelec, R. Bliem, M. Schmid, U. Diebold, G. S. Parkinson. **The role of surface defects in the adsorption of methanol on Fe<sub>3</sub>O<sub>4</sub>(001).** In: Top. Catal. (2016) DOI 10.1007/s11244-016-0713-9.

## CONFERENCE PROCEEDINGS & PRESENTATIONS

XV Congreso Colombiano de Química, Bogotá-Colombia 2008  
**Efecto del praseodimio y del cerio en la reducibilidad de catalizadores de níquel soportados en arcillas delaminadas.**

Novel Gas Conversion Symposium, Lyon-France 2010  
**Ni-Pr Catalysts supported on clays modified for the reaction of the reforming of methane with CO<sub>2</sub>.**

XXII CICAT, Cón-cón- Chile 2010  
**Catalizadores Ni-Pr soportados en minerales arcillosos modificados para el reformado seco de metano.**

Jahrestagung der Österreichischen Physikalischen Gesellschaft (ÖPG), Linz-Austria 2013  
**Water Gas Shift Chemistry at the Fe<sub>3</sub>O<sub>4</sub> (001) surface.**

Functional Oxide Surfaces and Interfaces (FOXSI), Hochkar-Austria 2014  
**Adsorption of Formic Acid on Fe<sub>3</sub>O<sub>4</sub> (001) surface.**

Jahrestagung der Österreichischen Physikalischen Gesellschaft (ÖPG), Pöllau-Austria 2014  
**Adsorption of Formic acid and Methanol on the Magnetite (001) surface.**

79. Jahrestagung der Deutschen Physikalischen Gesellschaft (DPG) und DPG-Frühjahrstagung der Sektion Kondensierte Materie (SKM), Berlin- Alemania 2015  
**Surface Chemistry of Magnetite (001) Surface.**

IX. Simposio Colombiano de Catálisis, Cali-Colombia 2015  
**Study of Intermediates in the Water Gas Shift Reaction on the Fe<sub>3</sub>O<sub>4</sub> (001) Surface.**